COMPACT, MID-INFRARED LASER SOURCE FOR REMOTE SENSING OF GAS EFFLUENTS

by

Trenton Jeffery Berg

A thesis submitted in partial fulfillment
of the requirements for the degree

of

Master of Science

in

Electrical Engineering

MONTANA STATE UNIVERSITY
Bozeman, Montana

November, 2009

APPROVAL

of a thesis submitted by

Trenton Jeffery Berg

This thesis has been read by each member of the thesis committee and has been found to be satisfactory regarding content, English usage, format, citation, bibliographic style, and consistency, and is ready for submission to the Division of Graduate Education.

Dr. Joseph Shaw

Approved for the Department Electrical Engineering

Dr. Robert Maher

Approved for the Division of Graduate Education

Dr. Carl A. Fox

STATEMENT OF PERMISSION TO USE

In presenting this thesis in partial fulfillment of the requirements for a master's degree at Montana State University, I agree that the Library shall make it available to borrowers under rules of the Library.

If I have indicated my intention to copyright this thesis by including a copyright notice page, copying is allowable only for scholarly purposes, consistent with "fair use" as prescribed in the U.S. Copyright Law. Requests for permission for extended quotation from or reproduction of this thesis in whole or in parts may be granted only by the copyright holder.

Trenton Jeffery Berg

November 2009

ACKNOWLEDGEMENTS

I must first thank my wife, Lori Jo, my sister, Nicole, and my parents, Debbie and Jeff for their unwavering love and encouragement throughout my graduate work and especially while I was writing this thesis. They have been incredibly supportive during one of the most difficult, but rewarding times of my life. Without them none of this would have been possible, and to them I owe all of my success.

I give special thanks to Kris Merkel, Randy Reibel, and Randy Babbitt for giving me the opportunity to work and grow into the field of optics. Without the opportunities these individuals have given me, I would not be where I am at today.

I am grateful to my teachers that I have had throughout my graduate degree: Joe Shaw, Kevin Repasky, and David Dickensheets. Joe, Kevin, and David have extraordinary gifts as teachers, and have guided me and shown unselfish patience towards me in my transition from Computer Science to Electrical Engineering.

Thanks go to Erin Egbert, Aaron Anderson, and Loren Coopmans for their support on this graduate work over the last two years. They played a significant role in the system-level component work presented in Chapter 5. I also thank the people I have met at S2 Corporation, Bridger Photonics, and Spectrum Lab for their support.

Last, but definitely not least, I thank my research advisor and great friend, Pete Roos. Over the past four years, he has had the single most profound influence on my development as a scientist. Pete combines patience, work ethic, knowledge, compassion, and balance in life like no one I've ever met. He has provided me guidance and friendship beyond anything I could have asked for.

TABLE OF CONTENTS

TABLE OF CONTENTS - CONTINUED

LIST OF TABLES

Table Page

LIST OF FIGURES

LIST OF FIGURES - CONTINUED

Figure Page

LIST OF FIGURES - CONTINUED

Figure Page

LIST OF FIGURES - CONTINUED

Figure Page

LIST OF FIGURES - CONTINUED

Figure Page

GLOSSARY OF ACRONYMS

ADC	Analog-to-Digital Converter
AR	Anti-Reflective
BPM	Birefringent Phase Matching
CLN	Congruent Lithium Niobate
CO_2	Carbon Dioxide
CW	Continuous Wave
DFB	Distributed Feedback
DFG	Difference Frequency Generation
DIAL	Differential Absorption Lidar
EPA	Environmental Protection Agency
FET	Field-effect Transistor
FWHM	Full Width Half Maximum
GRIIRA	Green Induced Infrared Absorption
KTP	Potassium Titanyl Phosphate
LIDAR	Light Detection and Ranging
LN	Lithium Niobate
MSPS	Mega Samples Per Second
NEP	Noise Equivalent Power
NPBS	Non Polarizing Beam Splitter
OPA	Optical Parametric Amplification
OPG	Optical Parametric Generation

GLOSSARY OF ACRONYMS – CONTINUED

OPO	Optical Parametric Oscillator
OSA	Optical Spectrum Analyzer
PBS	Polarizing Beam Splitter
PPKTP	Periodically Poled Potassium Titanyl Phosphate
PPLN	Periodically Poled Lithium Niobate
PPM	Parts Per Million
PPS	Pulses Per Second
PPSLT	Periodically Poled Stoichiometric Lithium Tantalate
QCL	Quantum Cascade Laser
QPM	Quasi Phase Matching
SLT	Stoichiometric Lithium Tantalate
SNR	Signal to Noise Ratio
TEC	Thermo-electric Cooler
YAG	Yttrium Aluminium Garnet

ABSTRACT

Remote sensing of gas effluents in the mid-IR wavelength region from 2 μm to 5 μm is preferred due to strong molecular absorption features (10 to 100 times stronger than in the near-IR) and high-transparency atmospheric windows. Currently, long-range mid-IR remote sensing is inhibited by the lack of suitable laser sources. As a result, frequency conversion in nonlinear optical materials has emerged as a powerful method to produce high-power, tunable, mid-IR light. However, compact, high-power narrowband conversion systems suitable for long-range mid-IR spectroscopy are not commercially available.

This thesis describes the development of a high-power, narrowband, tunable, compact, mid-IR laser source for long-range remote sensing of gas effluents. Frequency conversion into the mid-IR is achieved by use of a high-peak-power, compact pump laser and optical parametric generation (OPG) in periodically poled nonlinear crystals. This mid-IR laser system was designed and developed for remote sensing at ranges up to and exceeding 100 m in a compact form factor. Such a laser will fill the current scientific need for a hand-held mid-IR laser source capable of long-range mid-IR spectroscopy.

Based on theoretical models and experimental demonstrations a compact mid-IR laser source was developed that emits > 1 mJ broadband pulses in the mid-IR. To narrow the linewidth of the broadband OPG output, optical parametric amplification was demonstrated through seeding of the OPG process with a narrowband, continuous-wave, distributed feedback (DFB) laser. Seeding efficiencies exceeding 35% were demonstrated for 1 mJ of output energy, and efficiencies exceeding 65% were demonstrated at lower energies when the pump beam was spatially filtered. The linewidth of the narrowed mid-IR output was inferred to be < 350 MHz based upon heterodyne measurements conducted at the signal wavelength in the near-IR. This linewidth is well within the FWHM bandwidth of typical mid-IR atmospherically broadened molecular absorption features. The demonstrated mid-IR energies and laser linewidths are predicted to be sufficient for detection of low concentration gas effluents (< 1 ppm) at ranges exceeding 100 m. The developed mid-IR laser source was used to successfully demonstrate differential detection of carbon dioxide (CO_2).

CHAPTER 1

INTRODUCTION

Motivation / System Overview

Laser remote sensing has developed into an essential tool for remote detection and monitoring of atmospheric gases. More recently, laser remote sensing has become a critical method for identifying the presence of particular gas effluents for public safety, environmental protection, and national security. Detection of atmospheric gas effluents is possible because each molecule absorbs light at a unique "fingerprint" set of wavelengths, as can be seen in Figure 1. By probing the molecules absorption feature with a laser that exhibits the appropriate wavelength and linewidth, it is possible to determine the presence and concentration of a certain gas. This is a fundamental concept of sensing gases with the remote sensing technique Light Detection and Ranging (Lidar), where laser light is transmitted to the gas effluent of interest, and an optical receiver is used to collect and analyze the attenuated backscattered light.

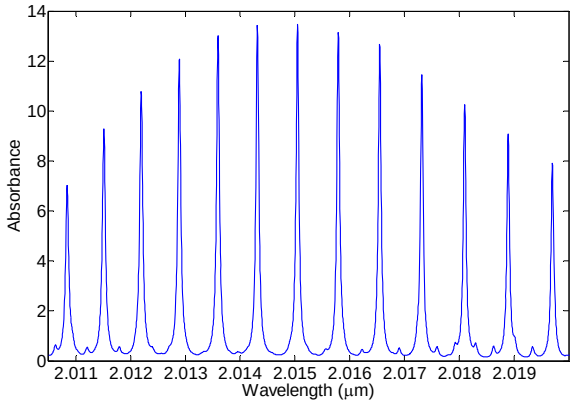

Figure 1. Absorption profile of atmospheric CO_2, showing the "fingerprint" absorption profile.

The mid-IR wavelength region is attractive for performing laser remote sensing for several reasons. Most small organic and inorganic molecules have their fundamental absorption features in the mid-IR wavelength region from 2 μm to 5 μm [1]. These absorption features are typically 10 to 100 times stronger than in the visible and near-IR regions. The stronger absorption allows a lidar system to more reliably detect the presence of gas effluents in the atmosphere, especially when the concentration is low. This absorption difference between the mid-IR and near-IR is because mid-IR radiation causes a fundamental transition between ro-vibrational states in the molecules, while near-IR radiation forces weaker overtone and combination-overtone ro-vibrational transitions [1]. As a result, many gas effluents that require detection and monitoring, have strong absorption features located in the mid-IR, which is illustrated by the colored lines in Figure 2. Remote sensing in the mid-IR is also advantageous due to the presence of high transparency atmospheric windows where low-attenuation laser light propagation through the atmosphere is achieved, which is shown in Figure 2, where the blue trace represents the atmospheric transmission a 100 meter horizontal path. Considering the strong absorption features present for an abundance of gas effluents of interest, and the high atmospheric transmission in the mid-IR, this spectral region is ideal for laser remote sensing.

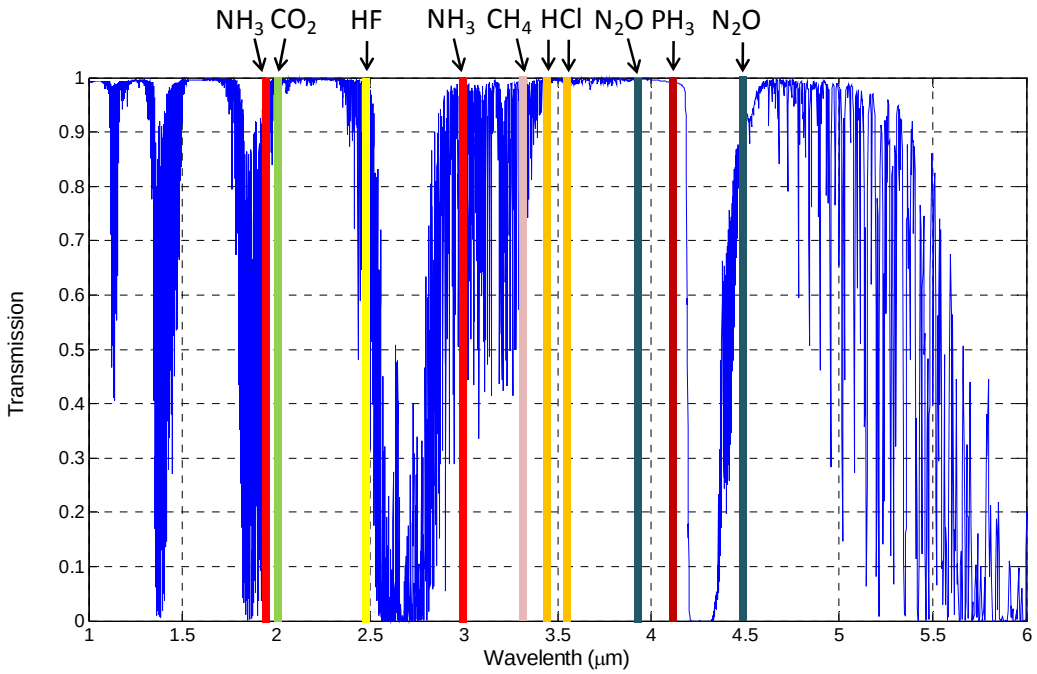

Figure 2. Plot showing the location of several gas effluents of interest located in the mid-IR (colored lines), along with the atmospheric transmission profile for a range of 100 m (blue). The atmospheric transmission (blue) was obtained from the ModTran atmospheric modeling software, and the gas effluent spectral lines (colored lines) were obtained from the HITRAN radiative transfer database.

Lasers are ideal light sources for atmospheric lidar systems because they provide the high peak powers, narrow linewidths, narrow pulse widths, and high repetition rates [2] necessary to probe the unique molecular absorption features. High peak powers allow for long-range remote sensing. Narrow laser linewidths allow for strong absorption of the laser light by the narrow bandwidth absorption features (<5 GHz) [3] of the gas effluent molecules. Pulsed lasers offer the capability of range-resolved measurements, where a narrower pulse width results in better range resolution. And high repetition rates allow for pulse averaging to increase the signal to noise ratio (SNR) of the lidar system. As a result, there have been significant advancements in modern lidar technology since the invention of the laser in the 1960's [2].

Unfortunately, mid-IR lidar systems have been inhibited by the lack of suitable laser sources. Quantum Cascade Lasers (QCL) can reach a wide wavelength range from 3.5 μm to 66 μm, and advancements are continually expanding this wavelength range. However, room-temperature-operated, commercially available QCL's are only available down to ~4.7 μm [1]. External-cavity diode lasers offer large tuning ranges and narrow linewidths, but are only available up to ~2.0 μm [1], and lack the peak power for long-range remote sensing. Lead-Salt Diode Lasers, and semiconductor lasers, such as heterojunction laser diodes and antimonide quantum well laser diodes, can cover small windows of the mid-IR; however, they require cryogenic cooling and lack the peak powers for long-range remote sensing applications [1]. Several powerful solid state lasers (primarily those based on rare-earth ions, etc.) can operate in limited bands in the mid-IR, but lack the wavelength flexibility for detecting various chemicals, the spectral purity for high-resolution spectroscopy, and/or the compact size for hand-held applications [1]. Due to the fundamentally limiting material properties that hamper construction of suitable lasers from 2.8 μm to 4 μm [1], frequency conversion in nonlinear optical materials has become extremely attractive to generate light in the mid-IR.

Frequency conversion in nonlinear optical materials provides a powerful and relatively simple way to generate tunable mid-IR light from available pump laser sources. These conversion processes are Optical Parametric Generation (OPG), and Optical Parametric Oscillation (OPO). In both of these processes a pump laser is passed into the nonlinear optical material and the material frequency converts the pump light into mid-IR

light. The difference between the two processes lies in the fact that an OPO utilizes a nonlinear material in a cavity for frequency conversion, while OPG requires only a single pass through the nonlinear material. OPO's are typically used to achieve frequency conversion threshold when a high power pump source is unavailable. OPO's can be operated in a triply resonant, doubly resonant, or singly resonant configuration depending on available pump power. If sufficient pump power is available to achieve threshold in a double pass through the nonlinear material, a simpler OPO can be constructed with a singly resonant cavity to enhance either the signal or idler. A commercially available OPO system was identified from M^2 lasers that is tunable from 2.7 μm to 4.7 μm, in a compact package [4]. However, this laser system has a 90-GHz linewidth, which makes long-range mid-IR spectroscopy difficult, and it can achieve an average power of only 450 mW at 350 kHz (~1 μJ/pulse) which would require averaging ~1000 shots to achieve similar performance to the mid-IR laser source reported here. In addition, this system is priced at ~$81,900, which is far too expensive for the compact sensor market to bear. Another mid-IR OPO system was identified from Aculight Corporation that can tune from 2.3 μm to 3.9 μm, and achieve >1 Watt of continuous wave (CW) power with 1 < MHz linewidth [5]. However this system would still require seconds of averaging to achieve long-range remote sensing and the unit is priced at $125,000.

Nevertheless, if a suitable high-power pump source is available, OPG is inherently advantageous because of the simplicity of single-pass frequency conversion, and the ability to achieve absolute frequency stability of < 1 GHz. However, current OPG systems suitable for long-range mid-IR remote sensing lack either the compact size, high

output power, or low cost required for the compact sensor applications. For example, we identified a newly released Difference Frequency Generation (DFG) based (which is a form of single pass OPG), commercially available mid-IR laser source offered by NovaWave Technologies, which they claim as “the first commercially available turnkey mid-infrared difference generation frequency (DFG-based) laser system” [6]. This laser system operates in the 3.3-μm +/- 100 nm wavelength range, and has a linewidth of < 3 MHz and an absolute frequency stability of 20 MHz making it suitable for mid-IR spectroscopy. However, this unit is a bench top system capable of only < 700 μW of CW output power. Consequently, it lacks the necessary output power for long-range (up to 100 m) remote sensing applications without seconds of averaging. Furthermore, this unit is priced at $55,250, which is once again too expensive for the compact sensor market. Therefore the need exists for a compact, ruggedized, low-cost, hand-held, widely-tunable, room-temperature-operated, absolute-frequency-stable, mid-IR laser source capable of long-range, high-resolution, single-shot, remote sensing of gas effluents in the atmosphere.

This thesis describes the development of an OPG based, high-power, compact, inexpensive, mid-IR laser source capable of meeting the aforementioned needs. This laser has the potential to be very compact, robust, and low cost owing to the monolithic pump source (75mm x 8 mm x 4 mm, $1,600 single unit price), the nonlinear optical materials (50 mm x 1 mm x 1 mm, $2,500 single unit price). The price and form factor will enable this laser to excel in applications where hand-held functionality is required. Also, this laser will operate narrowband (< 350 MHz linewidth) through use of optical parametric

amplification (see Chapter 4) which makes it ideal for mid-IR remote sensing of gas effluents. Even though this laser is potentially very small and inexpensive, it has the potential to detect low concentration gas effluents (< 1 ppm) with a single laser pulse from 100 meters, owing to sufficient mid-IR optical power as a result of efficient OPG conversion (see chapters 2 and 3). This laser also will have the ability to perform meter-level range-resolved spatial mappings of gas effluents owing to its short pulse durations (< 7 ns). Finally, the laser has the potential to be a widely tunable laser source over the mid-IR region of interest because of recent advancements in multi-channel nonlinear optical materials. All of these design considerations will be discussed in detail in the appropriate sections of this thesis.

Applications

A mid-IR laser source such as the one described here can be used for a wide variety of applications, including atmospheric pollution monitoring, industrial process control, leak detection, automotive engine exhaust analysis, drug detection, and medical disease diagnosis [1]. This thesis focuses on two very promising application spaces that are currently being pursued, methamphetamine (meth) lab detection and CO_2 pollution monitoring.

Meth is rapidly growing into a national drug crisis owing to its highly illicit and addictive nature, inexpensive price, relatively simple “cook” methods with over-the-counter ingredients, and growing popularity with young adults. Long-term meth abuse may result in many damaging effects, including violent behavior, anxiety, confusion, insomnia, paranoia, auditory hallucinations, mood disturbances, and delusions. Chronic

use frequently leads to symptoms such as: neurotoxicity (brain damage), respiratory problems, irregular heartbeat, and irreversible damage to blood vessels in the brain--producing strokes, heart and kidney damage, cardiovascular collapse, and death [7].

Meth use is an alarmingly major problem in Montana which ranked as the fifth worst state in 2005 [7,8]. A 2005 study reported that 65% of Montana's young adults reported that meth is "easy to get," 50% of Montana's foster care children were in foster care because of meth, and 50% of incarcerations were meth related [9]. The Montana attorney general reported that meth costs Montana $65 million per year in correctional and foster care services alone [9]. Although these statistics are extremely disturbing, they have begun to show improvement since 2005 [7,9]. These improvements are primarily because of laws put into place in 2005 to restrict over the counter sales of pseudoephedrine [10], a critical ingredient in meth production, and also because of the success of the Montana Meth Project, which has implemented graphic pictures (see Figure 3), television commercials, and radio advertisements into communities around Montana to attempt to deter possible users. Other states have adopted similar programs to the Montana Meth Project and have seen similar results [3].

Figure 3. Example of the graphic pictures implemented into Montana communities to deter potential meth users. Picture courtesy of Montana Meth Project (2009).

Unfortunately, drug enforcement personnel still lack the ability to rapidly acquire evidence of meth labs in widely varying locations, environments, and circumstances to eliminate the mass production of meth. Therefore, meth will remain a local and national drug crisis. Fortunately, the gas effluents associated with meth production have very strong absorption features that reside in the mid-IR wavelength region from about 2 μm to 4 μm. Furthermore, all meth production methods emit toxic gaseous byproducts, which are commonly vented into the atmosphere or enter the atmosphere when liquid/sludge byproducts are poured down drains or directly into the ground and evaporate. This situation is ideal for the proposed mid-IR remote sensor, because it will allow law enforcement to remotely probe a suspicious location for the vented meth-associated effluents. Because the remote sensor can reach anywhere in the wavelength region from 2 μm to 4 μm, it could scan the suspicious location for several of the 40 effluents associated with meth production to eliminate the possibilities of false positives. Such a device would be instrumental in the detection of meth labs to eliminate mass meth production.

The other main application that has been researched in this thesis is remote sensing of carbon dioxide (CO_2). CO_2 emissions have dramatically increased over the past 50 years as a result of a major increase in fossil fuel combustion [11]. The increased emissions, coupled with deforestation, have led to a dramatic increase in atmospheric CO_2 concentrations (see Figure 4) [12]. There is reason to believe that this increase in CO_2, along with other greenhouse gases, is significantly altering the global climate [13]. This alteration has led to a concentrated effort to stabilize current atmospheric

concentrations of CO_2. This effort was fueled by a ruling by the U.S. Supreme Court in 2007 that CO_2 is a pollutant under the federal Clean Air Act, which enables the Environmental Protection Agency (EPA) to regulate CO_2 emissions. Such regulations will require monitoring of a wide variety of pollution sources including automobile exhaust systems, industrial emission sources, and carbon sequestration sites.

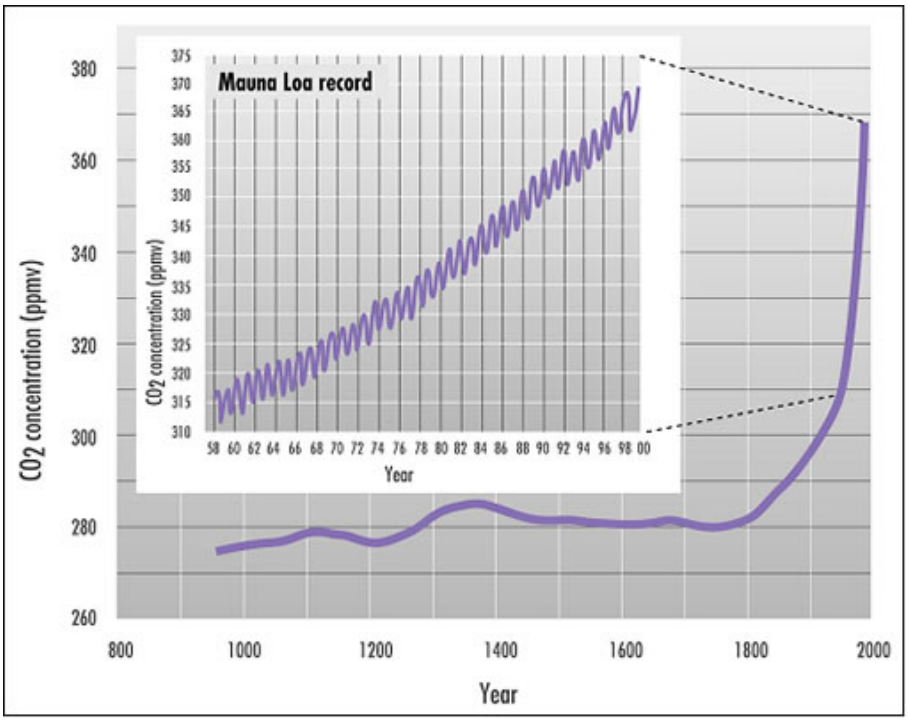

Figure 4. Atmospheric CO_2 concentration over the last 1000 years, based on ice core analysis and, since 1958, on direct measurements. Inset is the monthly average CO_2 concentration since 1958 at Mauna Loa, Hawaii [12].

With current technologies, EPA personnel would be forced to perform on-site scans of pollution locations by sampling the emitted effluents with point-source gas-intake measurement devices, because there currently exists no hand-held technology that can remotely determine the location and concentration of elevated CO_2 emissions. Fortunately, CO_2 has a strong absorption band near 2.0 μm (a factor of 100 greater than

in the near-IR), which is conveniently located in another major atmospheric window (see Figure 2). This combination makes CO_2 monitoring an ideal application for the proposed mid-IR lidar system. This device with its range-resolution capabilities would enable EPA personnel to simply aim the sensor toward a distant pollution source and measure the emitted CO_2 concentration, the distance to the source, and the spatial extent of the gas plume.

The Laser System: A Brief Introduction

To excel in the proposed applications spaces, an appropriate mid-IR laser must be constructed. Three major components are required to construct this compact laser system; a pump source, a nonlinear material to achieve Optical Parametric Generation (OPG), and a seed laser to achieve Optical Parametric Amplification (OPA). Each component will be discussed in detail at this time.

Scientific Materials Corporation (SMC) [14] offers a pump laser that emits high energy pulses, while maintaining a small and ruggedized form factor for hand-held operation. Owing to the second-order nature of the OPG process, high pump intensities (>100 MW/cm^2) are required to achieve the required frequency conversion threshold. In addition, due to reach the hand held sensor market, the pump laser must have a small form factor, and low power consumption. This is achieved by the SMC laser, termed the Monoblock, which is a Q-switched, Nd:YAG, 1064 nm, monolithic laser capable of producing pulses with energy >15 mJ, and pulse durations < 10 ns, with a form factor of ~3” in length, which can be seen in Figure 5. This laser, along with an intra-cavity OPO

to generate 1.5-μm light, was developed and deployed by Army Night Vision Labs as an eye safe range finder mounted to soldiers weapons in the armed forces [15]. As a result it was developed into a ruggedized and compact package, and the flashlamp pumped version of this laser can operate on a pair of AA batteries for extended periods of time. From Figure 5, the laser cavity is created by the output coupler and a highly reflective coating placed on the back of the Nd:YAG gain medium. A Brewster cut is used to select out a polarization state of the output emission. All of the components are secured to a monolithic YAG rail with the same expansion coefficient to eliminate temperature-induced misalignment. For our application we neglect the intra-cavity OPO that was part of the original design.

The Monoblock as designed does not exhibit single longitudinal mode operation, which is critical for molecular spectroscopy applications. Therefore the laser was modified by Spectrum Lab and Bridger Photonics personnel in the early portions of this project to achieve consistent single-mode operation. The linewidth of the modified Monoblock was measured to be ~250 MHz, which is important when attempting to produce narrowband mid-IR light through OPG/OPA processes. All of these and the aforementioned properties make the Monoblock an ideal laser to pump the OPG/OPA process and generate narrowband mid-IR light in a compact package.

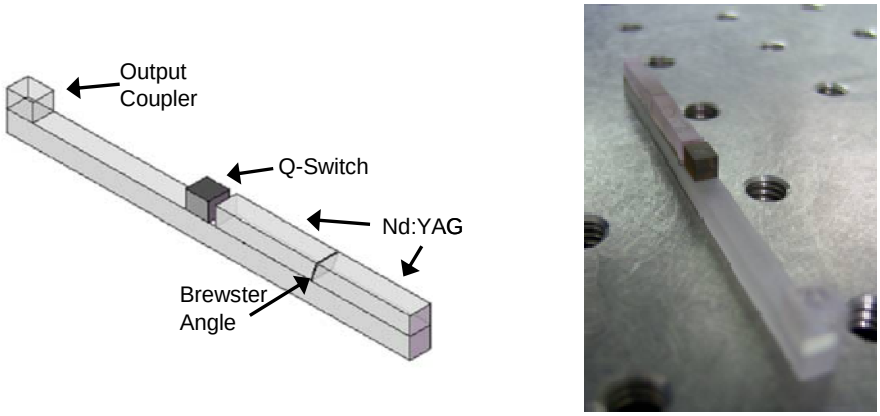

Figure 5. (Left) A SolidWorks drawing showing the monolithic laser components of the Monoblock. (Right) A digital image of the Monoblock near 1-inch spaced holes to provide scale.

Optical Parametric Generation (OPG) is a 2nd-order ($\chi^{(2)}$) nonlinear process that occurs when a pump laser interacts with a 2nd-order ($\chi^{(2)}$) nonlinear optical material. In this process, a pump photon is incident on a nonlinear material, and through the nonlinear interactions with the material, the pump photon is converted into two lower-energy (lower-frequency) photons, as shown with a simple schematic in Figure 6. The two created photons are known as the signal and the idler. This interaction can lead to exponential growth in both the signal and idler modes. OPG is a parametric process, which requires that energy is conserved in the pump, signal, and idler leading to the following equation in terms of wavelength, where $\lambda_x = 2\pi c/\omega_x$ [22],

$$\frac{1}{\lambda_{pump}} = \frac{1}{\lambda_{signal}} + \frac{1}{\lambda_{idler}}. \tag{1.1}$$

For a given pump wavelength, the allowed signal and idler pairs are determined by conservation of energy, and also conservation of momentum, or phase matching, which is the ability for the three beams to remain phase matched, which is discussed in detail in Chapter 3.

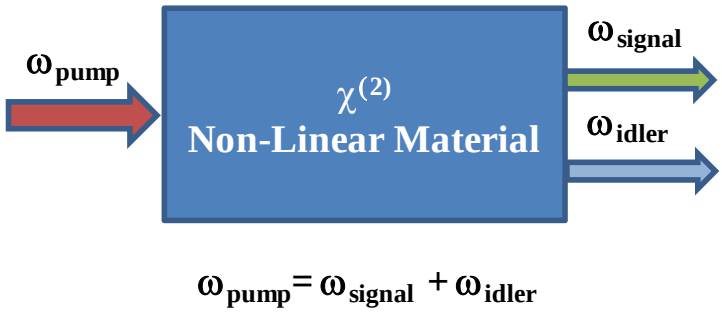

Figure 6. A simple picture showing the basic concept of optical parametric generation.

In OPG, the frequency conversion begins from a phenomenon known as parametric fluorescence, which results in broadband (> 100 GHz) signal and idler emission. This is analogous to spontaneous emission in an amplifier. However, high-resolution gas sensing requires that the mid-IR laser source have a linewidth narrower than that of the gas effluent species, which is typically ~3.5 GHz (FWHM) for atmospherically broadened mid-IR absorption features. Therefore, the broadband output must be narrowed to allow for use of the mid-IR laser in spectroscopy applications.

Optical parametric amplification (OPA) is a process used to obtain narrowband emission of the signal and idler. This is achieved by inputting narrowband light (spatially overlapped with the pump) into the nonlinear material at the signal or idler wavelength to seed the OPG process. It is called OPA because it is an amplification of the narrowband light at the seed laser wavelength, as long as the seed wavelength is spectrally overlapped with either the broadband signal or idler. As a result, OPA results in a narrowing of both the signal and idler, regardless of which beam is seeded, provided a narrowband seed laser is used. This process is analogous to seeding an amplifier to start the process from stimulated emission rather than spontaneous emission. The seed laser can either be a

pulsed or CW source, therefore for simplicity we choose to seed with commercially-available, narrowband Distributed Feedback (DFB) diode lasers located at the signal wavelength. These lasers are ideal because they are obtainable throughout the near-IR where the signal wavelengths will be located, are sufficiently narrowband, and have a compact form factor. Also, DFB's can easily tune over several nanometers, which will be important when performing differential absorption lidar (DIAL) measurements discussed briefly in this chapter and in detail in Chapter 2.

Gas Effluent Detection: A Brief Overview

Owing to the unpredictable nature of the atmosphere and the generally weak amplitudes of backscattered light, advanced detection schemes must be used when detecting gases in the atmosphere. In general, the detection measurements are performed by directing the transmit laser light through a plume of the gas effluent of interest and monitoring the level of attenuation on the return pulse caused by molecular absorption. However, the highly turbulent nature of the atmosphere makes it difficult to differentiate attenuation caused by molecular absorption from signal fading caused by turbulence. Therefore, single-wavelength spectroscopy can produce errors when the signal is altered by the variable atmosphere.

Differential Absorption Lidar (DIAL), which is illustrated in Figure 7, is a differential measurement technique that eliminates many of the unknown atmospheric variations by directing two laser pulses at the gas effluent of interest, each with a different wavelength. One pulse's wavelength is spectrally located on an absorption

feature (λ_{on}), and the second off resonance from the absorption feature (λ_{off}). This difference results in λ_{on} being absorbed more strongly if the gas effluent is present. A small portion of the light passing through the plume scatters back along the beam path and is focused onto a sensitive detector. A measurable difference in the signal level between the two paths means that the gas effluent was present. The higher the absorption difference, the greater the amount of the gas effluent is present. The two wavelengths can be easily achieved by sequentially tuning the OPA seed laser on the resonant transition and then off.

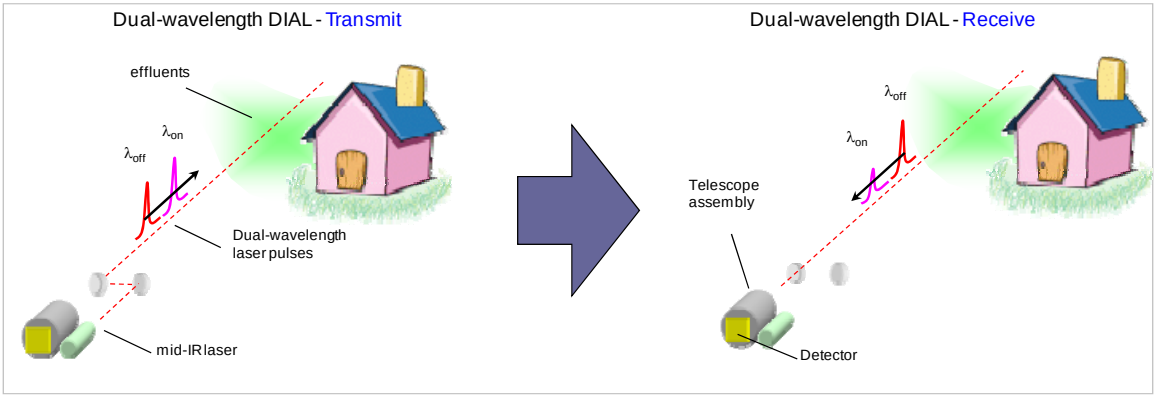

Figure 7. A picture illustrating the basic idea of the DIAL measurement technique where two wavelengths of light are emitted, one of which is absorbed more strongly than the other. A differential measurement is made, and based upon the known absorption characteristics of the gas effluent, the presence and/or the amount of the gas effluent can be determined.

The measurement sensitivity typically depends on the amount of light that is backscattered, collected, and focused onto the detector. This is dictated primarily by the backscatter coefficient of the scattering source. Typical lidar systems use elastic backscattering from atmospheric molecules (Rayleigh scattering) and aerosol particles (particle or Mie scattering). In the mid-IR elastic backscattering is dominated by particle

scattering because of the $1/\lambda^4$ wavelength dependence of Rayleigh scattering. Particle backscatter efficiencies depend strongly on the atmospheric density of aerosols; however, in the mid-IR, backscatter efficiencies tend to be on the order of 1 photon per million (1e-6) per range bin [2 pg. 132].

Alternatively, if allowed by the application, topographical scattering from a hard target source such as a house located behind the plume of interest can be used to significantly increase the backscatter efficiencies to on the order of 1 photon per 10 (0.1) per range bin [16]. The application space will determine whether particle or topographical scattering is used, a selection that is described in more detail in Chapter 2.

Overview of Thesis

This introductory chapter was devoted to presenting the motivation for a mid-IR remote sensor, the approach taken to solve several key shortcomings of existing laser sources, and several of the very promising applications of a mid-IR lidar system to be built with the laser source described here. This chapter also briefly introduced the components that allow realization of a mid-IR laser source, and the basic concepts of remote sensing such that an introductory understanding of the proposed system is achieved. The following Chapters will focus on the details of the laser system and remote sensing techniques as well as all other critical aspects of this project. Chapter 2 reviews the performance specifications that the laser system must achieve, which were determined by performing a radiometric analysis. Chapter 3 will describe the down selection of a nonlinear optical material that can meet the transmit energy level

requirements determined in the performance specifications. Chapter 4 will present introductory theory and experimental results for optical parametric amplification (OPA) to obtain narrowband emission. Chapter 5 will discuss the supporting mechanical and electrical system components of the remote sensing system that are necessary to perform consistent, accurate measurements. Chapter 6 will present the experimental setup and results for gas effluent testing performed with a constructed mid-IR laser source. Finally, a summary of the work performed will be given, along with recommendations for future research, in Chapter 7.

CHAPTER 2

PERFORMANCE REQUIREMENTS

This chapter is devoted to system modeling to determine the required parameters to perform long-range mid-IR remote sensing of gas effluents. The primary goal of these calculations is to determine the requirements of the laser source. As a result, the mid-IR laser source design is based on the transmit energy requirements calculated in this chapter. The calculations rely heavily on the lidar equation, the DIAL equation, the atmospheric transmission, and the HITRAN radiative transfer database, which are all discussed in detail in this chapter. At the conclusion of this chapter we will have determined the transmit energy requirements for both the meth and CO_2 applications to perform high-resolution DIAL measurements.

Lidar Equation

The achievable resolution of a lidar system relies strongly on the level of backscattered light collected by the receiver. Atmospheric transmission is a critical parameter for remote sensing over long distances, but several other parameters must be considered also. The amount of light returning from the object or plume of interest is governed by the Lidar Equation, which is given by,

$$E(R,\lambda) = E_L \frac{c\tau}{2} \eta(\lambda) \frac{A}{R^2} O(R) \beta(R,\lambda) T^2. \qquad (2.1)$$

This equation describes atmospheric, elastic, backscattered returns with pulsed laser illumination, and is illustrated in Figure 8. In this equation, *E(R, λ)* is the detected peak

optical energy per pulse, E_L is the transmitted laser pulse energy, c is the speed of light, τ is the pulse duration, η is the overall optical efficiency of the receiver system which includes every optical element that the receive light passes through before detection, A is the receiver collection optic area or the telescope entrance pupil area as seen in Figure 8, R is the range to the scattering gas effluent of interest, $O(R)$ is the range-dependent overlap factor between the transmitter and the receiver (or, as illustrated in Figure 8, the ratio of the area of the receiver field of view to the laser beam area at a range R), β is the backscatter coefficient which describes how much light is scattered in the backwards direction towards the lidar receiver, and T^2 is the range- and wavelength-dependent round-trip atmospheric transmission factor, which for a uniform path is given by the Lambert-Beer-Bouguer law as,

$$T^2 = exp\left[-2\int_0^R \alpha(r,\lambda)dr\right], \tag{2.2}$$

where α is the total extinction coefficient, which also is a function of wavelength and range. The parameter α includes both scattering losses in the atmosphere and absorption by the gas effluent of interest. The quantity $c\tau/2$ in Eqn. (2.1) is known as a range bin, or ΔR, which represents the total plume length illuminated by one laser pulse as seen in Figure 8. A range bin also determines the achievable range resolution of the system, if applicable. The A/R^2 parameter in Eqn. (2.1) is the projected solid angle subtended by the collection optic (telescope) with area A as seen from the scattering event at range R which is also illustrated in Figure 8. Eqn. (2.2) is plotted in Figure 2 (blue trace is one way transmittance) for the near-IR and mid-IR wavelength regions; however, this plot only illustrates the losses inflicted through typical rural atmospheric conditions and does not

portray any information regarding the unknown plumes of gas effluents that we are trying to detect. However, as will be shown later in the chapter, information regarding the gas effluent of interest is contained in Eqn. (2.2) when performing DIAL measurements.

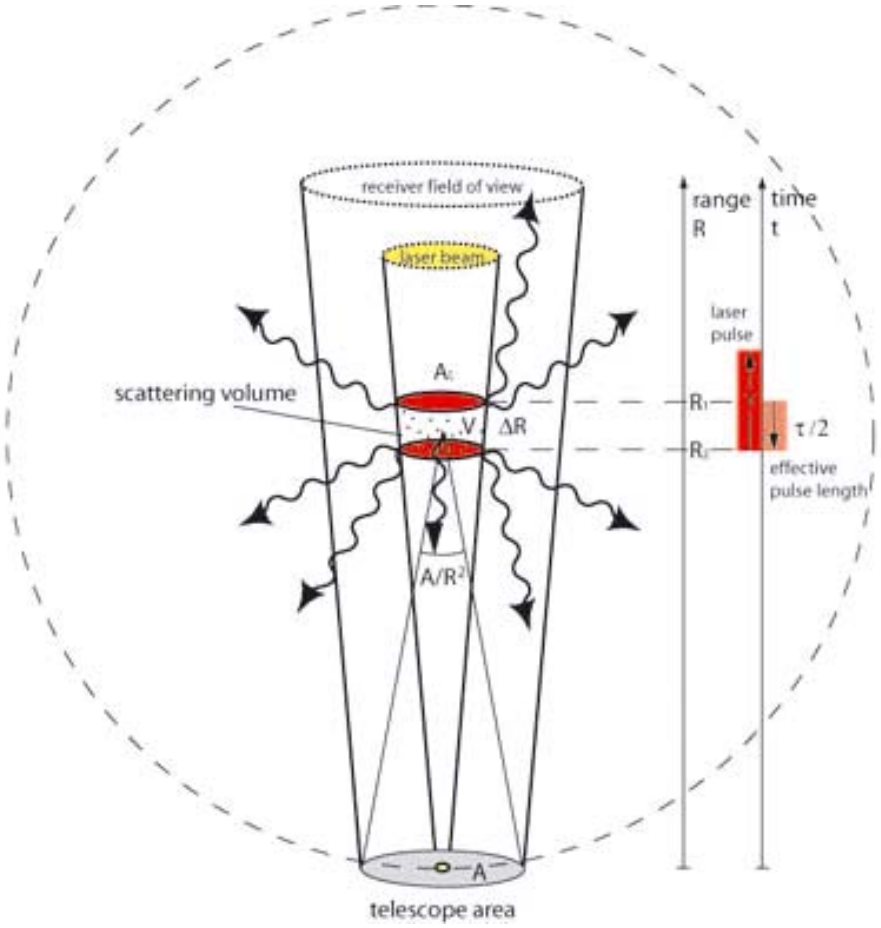

Figure 8. Illustration of the lidar geometry [2].

System Specifications

The lidar equation is critical in guiding the design of a lidar system to achieve its overall goals. Ultimately, the lidar equation determines the amount of transmit power that is required to receive a suitable return lidar signal for high-resolution measurements. However, additional calculations involving the Noise Equivalent Power (NEP) of the

receiver photodetector must be performed to determine the actual Signal-to-Noise Ratio (SNR) of the system. The photodetector NEP can drastically alter the achievable SNR, and the minimum measurable concentration at long ranges. In the next two sections, the lidar equation and these additional calculations are used to find system specifications for the meth and CO_2 applications.

Meth Detection Specifications

The meth detection application is purely a binary detection scenario: either the gas effluent of interest is present or not. Therefore, the goal is to remotely determine if low concentrations of meth associated effluents are present. Experimental data has shown that typical concentrations for the major gas effluents associated with the meth cook are on the order of 0.1 ppm to 250 ppm during the cook stage [17]. Depending on the gas effluent's absorption cross section, this results in a typical transmission loss of ~0.1% through just one meter.

Because of the inverse square dependence of the detected signal energy on range, the maximum range to target is extremely critical and must be first be specified. Based on conversations with drug enforcement personnel, a maximum range required for the meth lidar system was chosen to be 100 meters. This is the range that is estimated to be required to uncover >95% of meth labs. Therefore, the goal is to measure 0.1% changes in the detected lidar signal at a maximum range of 100 meters. However, because only detection is desired, range-resolved measurements are not necessary, which allows for the use of topographical scattering to significantly increase the detected lidar signal levels. It is anticipated that the meth lab itself and the surrounding environment will serve as the

topographical scatterer. Based upon these parameters, a set of system specifications for the meth lidar system are generated that allows for an estimation of the necessary transmit power. The list of system specifications can be seen in Table 1.

Table 1. Table of system specifications for the meth lidar system.

Parameter	**Value**
Transmit Energy (E_L)	E_L = 1.0 mJ
Pulse Duration (τ)	τ = 7 ns
Spectral Transmission (η)	η = 0.5
Collection Optic Area (A)	A = 20 cm^2
Range to Target (R)	R = 100m
Overlap Factor (O)	O = 0.8
Backscatter Efficiency (β)	β = 0.15
Atmospheric Trans. (T)	T = 0.93

For a 2-inch-diameter collection optic (20 cm^2 area), an overlap factor of 0.8, and a spectral transmission of 0.5, from Eqn. (2.1), the expected return will be reduced from the transmit power by a factor of ~2.7×10^8. Assuming the noise for this measurement is dominated by the detector NEP rather than signal shot noise or amplifier noise, the achievable SNR with this set of specifications is determined by,

$$SNR = \frac{P_{detected}}{NEP_{Det}}. \tag{2.3}$$

For a typical mid-IR detector with a room-temperature NEP = 1.7×10^{-11} W/Hz^{½} and 100 MHz of bandwidth [18], 1 mJ of transmit energy (143-kW peak power) will result in an SNR of approximately 1600 (32 dB). This is sufficient to detect small (~0.1%) pulse differences due to meth effluent absorptions. Therefore the mid-IR laser source under development must achieve narrowband output energies exceeding 1 mJ.

CO_2 Monitoring Specifications

In contrast, the CO_2 application is a spatial mapping and monitoring scenario, where the goal is to remotely obtain information regarding the extent and concentration of typically high-concentration CO_2 pollution plumes. Therefore, in this application range-resolved measurements are required, which prohibits the use of a topographical scatterer. As a result, for this application the lidar system must rely on significantly weaker particle backscattering. An estimated backscatter coefficient of β = 1e-6 was used in the calculations [2]. Because a maximum range was not specified for this application, the design will be based on achieving unity SNR at 100 meters. Based upon these parameters, a set of system specifications for the CO_2 lidar system can be generated that allows for an estimation of the necessary transmit power. The list of system specifications can be seen in Table 2.

Table 2. Table of system specifications for the CO_2 lidar system.

Parameter	**Value**
Transmit Energy (E_L)	E_L = 1.5 mJ
Pulse Duration (τ)	τ = 7 ns
Spectral Transmission (η)	η = 0.5
Collection Optic Area (A)	A = 20 cm^2
Range to Target (R)	R = 100 m
Overlap Factor (O)	O = 0.8
Backscatter Efficiency (β)	β = 1e-6
Atmospheric Trans. (T)	T = 0.90

For this design we assumed a 2-inch-diameter collection optic (20 cm^2 area), an overlap factor of 0.8, a spectral transmission of 0.5, a detector NEP of 7e-13 W/Hz^{½} [19], and a 100 MHz detector bandwidth. Because this is a range-resolved system that relies on

particle scattering, the fractional amount of return light is range dependent, which means that the SNR is also range dependent. Based upon the detector specifications presented here and the detected lidar signal at each range determined by Eqn. (2.1), the SNR can be calculated for all ranges out to 100 meters using Eqn. (2.3). A plot of the calculated SNR vs. range based upon the system specifications in Table 2 can be seen in Figure 9, where the *y* axis is plotted on a log scale for visual purposes. Therefore, with1.5 mJ of transmit energy (205 kW), the system will be able to achieve range-resolved mappings of high concentration CO_2 pollution plumes out to 100 meters.

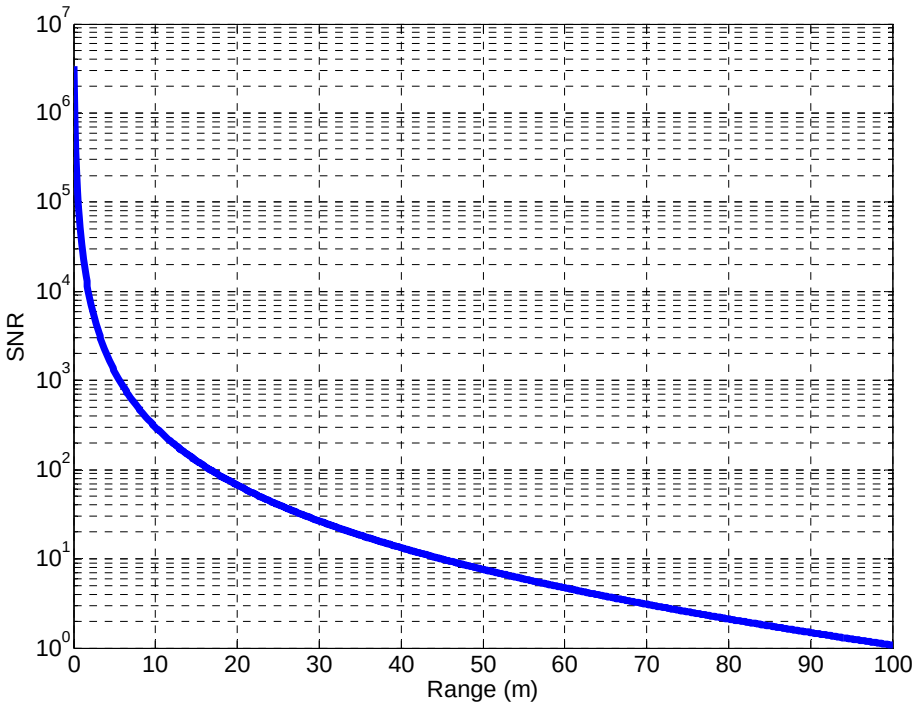

Figure 9. Plot showing the SNR vs. Range, which shows that the SNR goes to unity at 100 meters. The y axis is plotted on a log scale for visualization purposes.

The calculated SNR's allows for an estimation of the expected performance of the mid-IR lidar system for each application; however, due to the widely variant nature of the

atmosphere, DIAL techniques must be used to perform the required high-resolution measurements. Therefore, further analytical analysis must be carried out to determine the estimated system performance when performing DIAL measurements.

Differential Absorption Lidar (DIAL)

When operating in a DIAL configuration, the detected lidar signals are evaluated through analysis of the lidar equation at the "on" and "off" wavelengths at a range (R), and after a range bin (ΔR) to determine the presence and/or concentration of the gas effluent of interest. As was stated previously, the information regarding the concentration of the gas effluent of interest is contained in the total extinction coefficient α from Eqn. (2.2), which can be expanded to the form

$$\alpha = \kappa(R, \lambda) + N(R)\sigma(R, \lambda), \tag{2.4}$$

where κ contains all losses due to atmospheric scattering, and N is the concentration of the gas effluent of interest with a known molecular absorption cross section σ. The molecular absorption cross section (σ) can be accurately determined from the HITRAN radiative transfer database [3]. To determine the measured concentration $N(R)$ of the gas effluent of interest from the detected lidar signals, a series of derivations must be performed, which followed the work of Obland et al [20]. The derivation begins by determining the incremental change in detected energy for the "on" pulse at ranges R and $R+\Delta R$. To extract the desired end quantity $N(R)$ from the exponential, the natural log is taken for each term.

$$ln\big(E_{on}(R)\big) - ln\big(E_{on}(R+\Delta R)\big) =$$

$$ln\left[E_L \frac{c\tau}{2}\eta(\lambda_{on})\frac{A}{R^2}O(R)\beta(R,\lambda_{on})\, exp\left[-2\int_0^R \kappa(R,\lambda_{on}) + N(R)\sigma(\lambda_{on})dR\right]\right] \qquad (2.5)$$

$$-ln\left[E_L \frac{c\tau}{2}\eta(\lambda_{on})\frac{A}{(R+\Delta R)^2}O(R+\Delta R)\beta(R+\Delta R,\lambda_{on})\left[-2\int_0^{R+\Delta R} \kappa(R+\Delta R,\lambda_{on}) + N(R+\Delta R)\sigma(\lambda_{on})d(R+\Delta R)\right]\right]$$

Upon performing the subtraction of the natural logs, the non-range-dependent parameters E_L, $c\tau/2$, η, and A will immediately cancel from the equation. We can also make the assumption that the overlap factor O, backscatter coefficient β, and scattering coefficient κ will change negligibly over a range bin and will also cancel out, reducing the equation to the form,

$$ln\big(E_{on}(R)\big) - ln\big(E_{on}(R+\Delta R)\big) =$$

$$ln\left(\frac{1}{R^2}\right) - 2\sigma(\lambda_{on})\int_0^R N(R)dR -$$

$$ln\left(\frac{1}{(R+\Delta R)^2}\right) + 2\sigma(\lambda_{on})\int_0^{R+\Delta R} N(R+\Delta R)d(R+\Delta R). \qquad (2.6)$$

Next we will group the natural log terms appropriately to achieve the following equation,

$$\ln\left(\frac{E_{on}(R)}{E_{on}(R+\Delta R)}\right) = \ln\left(\frac{(R+\Delta R)^2}{R^2}\right) - 2\sigma(\lambda)\left[\int_0^R N(R)dR - \int_0^{R+\Delta R} N(R+\Delta R)d(R+\Delta R)\right]. \qquad (2.7)$$

Further reduction can be accomplished by the following assumption,

$$-\int_0^R N(R)dR + \int_0^{R+\Delta R} N(R+\Delta R)d(R+\Delta R) =$$

$$-\int_0^R N(R)dR + \int_0^R N(R)dR + \int_R^{R+\Delta R} N(R+\Delta R)d(R+\Delta R) = N(R)\Delta R, \qquad (2.8)$$

which assumes that the gas effluent concentration changes very little over a range bin, which can also be thought of as calculating the average concentration over a range bin. Upon substituting the result from Eqn. (2.8) into Eqn. (2.7),

$$\ln\left(\frac{E_{on}(R)}{E_{on}(R+\Delta R)}\right) = \ln\left(\frac{(R+\Delta R)^2}{R^2}\right) + [2\sigma(\lambda_{on})N(R)\Delta R]. \qquad (2.9)$$

The derivation made for the “on” wavelength can be similarly made for the “off” wavelength, and the same approximations remain accurate as well. The “off” wavelength can therefore be represented as

$$\ln\left(\frac{E_{off}(R)}{E_{off}(R+\Delta R)}\right) = \ln\left(\frac{(R+\Delta R)^2}{R^2}\right) + \left[2\sigma\left(\lambda_{off}\right)N(R)\Delta R\right]. \quad (2.10)$$

To determine the measured concentration of the gas effluent, the detected lidar signal for the “off” wavelength (Eqn. (2.10)) must be subtracted from the “on” wavelength (Eqn. (2.9)) to determine the incremental change between the two pulses.

$$\ln\left(\frac{E_{on}(R)}{E_{on}(R+\Delta R)}\right) - \ln\left(\frac{E_{off}(R)}{E_{off}(R+\Delta R)}\right) =$$

$$\ln\left(\frac{(R+\Delta R)^2}{R^2}\right) + [2\sigma(\lambda_{on})N(R)\Delta R] - \ln\left(\frac{(R+\Delta R)^2}{R^2}\right) - \left[2\sigma\left(\lambda_{off}\right)N(R)\Delta R\right], \quad (2.11)$$

which results in the simplified equation that represents the measured concentration from the detected lidar signals for the “on” and “off” wavelengths [2 pg.189],

$$N(R) = \frac{1}{2(\sigma_{on}-\sigma_{off})\Delta R}\ln\left[\left(\frac{E_{on}(R)}{E_{on}(R+\Delta R)}\right)\left(\frac{E_{off}(R+\Delta R)}{E_{off}(R)}\right)\right]. \quad (2.12)$$

This is the most commonly used form of the equation when analyzing DIAL measurements, and agrees with reference 2 (page 189). However, further approximations can be made for our system to simplify the analysis. For the two proposed applications the “off” wavelengths will be very far detuned from any absorption features. Therefore the approximation can be made that the change in the “off” wavelength over a range bin ΔR is small compared to the change in the “on” wavelength over a range bin. Therefore the measured energy for the “off” wavelength before and after a range bin will essentially be the same. Also, because the “off” wavelength is very far detuned from any absorption

feature, the molecular absorption cross section for that wavelength is essentially zero, resulting in

$$N(R) = \frac{1}{2(\sigma_{on})\Delta R} \ln\left[\left(\frac{E_{on}(R)}{E_{on}(R+\Delta R)}\right)\right]. \quad (2.13)$$

Finally, another derivation can be performed that allows for a relation between the minimum measurable molecular density of the lidar system and the calculated SNR for the system. This derivation begins by defining the following inequality, [21 pg. 291],

$$E_{on}(R) - E_{on}(R + \Delta R) \geq \frac{E_{on}(R+\Delta R)}{SNR}. \quad (2.14)$$

This effectively states that the fractional optical pulse energy reduction due to the gas effluent over a range bin must be greater than the inverse of the SNR. This equality can be manipulated into the following form,

$$\left(\frac{E_{on}(R)}{E_{on}(R+\Delta R)}\right) = 1 + \frac{1}{SNR}, \quad (2.15)$$

which can be substituted into Eqn. (2.13) to obtain the following equation that can be used to estimate the minimum measurable molecular density of a lidar system based on a calculated SNR,

$$N(R)_{min} = \frac{1}{2\sigma_{on}\Delta R} \ln\left[\left(1 + \frac{1}{SNR}\right)\right]. \quad (2.16)$$

This equation can now be used to determine the minimum measurable molecular density for the meth and CO_2 applications. For the meth application, using the SNR value of 1600, a typical molecular absorption cross section of 1e-18 cm^2 [3], and a ΔR of 300 cm, the minimum detectable molecular density $N(R)_{min}$ = 1e12 cm^{-3}. The minimum measurable concentration in parts, can be found by dividing the minimum detectable molecular density by the molecular density of a cubic centimeter for atmospheric

pressures of 2.479e19 cm^{-3}. Based upon this calculation, the theoretical minimum measurable concentration for the meth lidar system is ~0.1 ppm. Based on experimental data from Martyny et al [17], meth effluent concentrations up to 250 ppm level can be expected in meth labs, depending on the effluent. If necessary, it is possible to reduce the detectable concentration significantly by increasing the collection area, decreasing the range, using a more efficient topographical scatterer, or averaging over multiple pulses. Also, if the plume is larger than a range bin, than the minimum measurable concentration will improve.

Similar calculations can be performed for the CO_2 system. Using the SNR vs. range data calculated previously in this chapter, the CO_2 molecular absorption cross section at 2.0 μm of 5e-21 cm^2 [3], a ΔR of 300 cm, and the molecular density of a cubic centimeter for atmospheric pressures of 2.479e19 cm^{-3}, the minimum measurable concentration in ppm as a function of range can be seen in Figure 10. This plot shows that the CO_2 lidar system theoretically will be able to measure < 10,000 ppm concentration plumes at 100 meters, which is well below the estimated concentration of the target pollution sources based on discussions with the EPA.

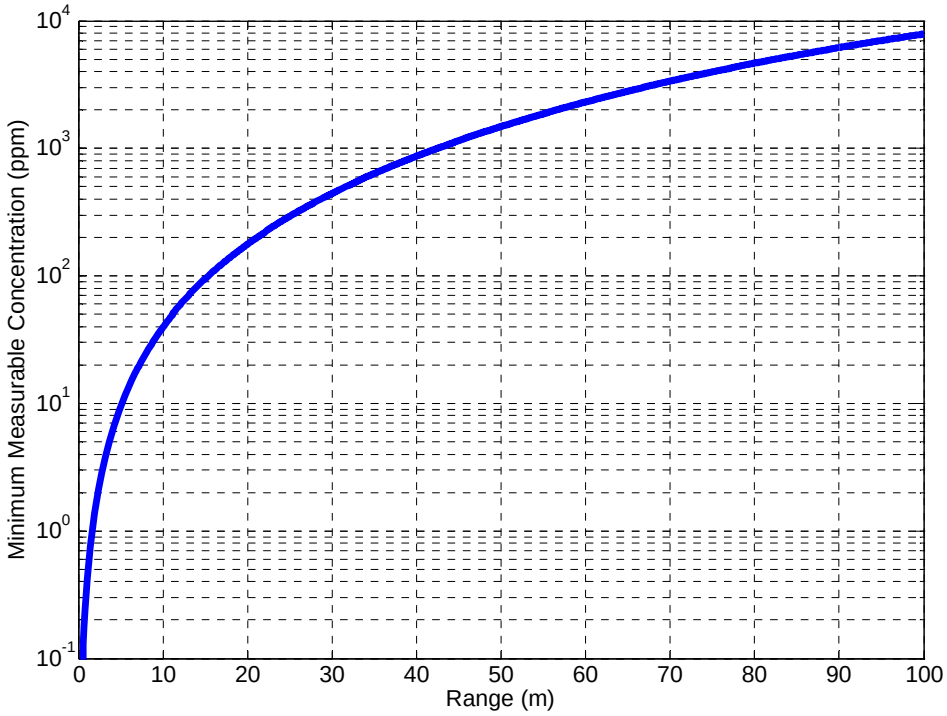

Figure 10. Plot showing the minimum measurable concentration in parts per million above ambient atmospheric concentrations of CO_2 as a function of range.

In summary, the goal of calculating the system specifications in this chapter was to guide the design of the appropriate laser source to excel in the remote gas sensing applications. The goal of Chapter 3 is to use the performance specifications calculated in Chapter 2 to develop the appropriate mid-IR laser system to achieve the performance requirements necessary to meet the goals of the desired application spaces.

CHAPTER 3

NONLINEAR CRYSTAL SELECTION

This chapter describes the selection process of the appropriate nonlinear crystal to achieve the maximum conversion efficiency into the mid-IR to meet the mid-IR energy requirements for high-resolution remote sensing determined in Chapter 2. This chapter will address some of the critical properties of the nonlinear materials, including a discussion pertaining to phase matching, along with the development of models to assist in the selection process. Finally, experimental results will be presented that demonstrate sufficient frequency conversion into the mid-IR in several nonlinear materials.

Overview of Nonlinear Materials

OPG is a second-order, $\chi^{(2)}$, nonlinear optical interaction, which only occurs in noncentrosymmetric materials. This is a result of the inversion symmetry property of centrosymmetric materials which cancels out any second-order nonlinear processes. Liquids, gases, amorphous solids (glasses), and many crystals cannot be used to produce second-order interactions due to this inversion symmetry [22]. This limits the available materials to nonlinear crystals, and the choice of crystal depends on several factors including the effective nonlinear coefficient, wavelength transparency range, and damage threshold. The wavelength transparency range describes the wavelength range where the crystal does not absorb a significant portion of incident light, and the optical damage

threshold defines the intensity of light the crystal can sustain without damage, which is discussed in more detail later in this chapter.

The nonlinear coefficient, which is sometimes referred to the effective nonlinear coefficient, or d_{eff}, is a coefficient that defines the susceptibility of the nonlinear crystal to produce a second-order response. This coefficient is widely dependent on the type of nonlinear crystal, and can also vary within a crystal depending on what axis of the crystal light propagates down [1 pg. 106]. As a result, the nonlinear coefficient is typically written in tensor notation such as, d_{33} or d_{13}, where the indices relate the nonlinear susceptibility to the polarization of the incident and generated light with respect to a crystal axis. For example, the coefficient d_{33} means that the pump, signal, and idler are required to have the same polarization with respect to a crystal axis to access that nonlinear coefficient, and the coefficient d_{13} means that the incident and generated beams must have perpendicular polarizations with respect to a crystal axis to access that nonlinear coefficient. This idea is important when selecting the appropriate nonlinear crystal, and will also be important when discussing the concept of phase matching.

Phase Matching

Efficient conversion from the pump to the signal and idler requires that the three beams stay phase matched as they propagate through the nonlinear crystal, so that the amplitude contributions from different locations in the crystal to the product wave are all in phase. This phase matching can be described by conservation of momentum and the wave vectors (k) of each beam [22],

$$k_{pump} - k_{signal} - k_{idler} = \Delta k \tag{3.1}$$

For,

$$k_i = \frac{n_i(T)\omega_i}{c} \tag{3.2}$$

Where *n* is the temperature-dependent index of refraction of the nonlinear material, ω is the angular frequency of the beam, and *c* is the speed of light. For perfect phase matching, $\Delta k = 0$, which results in maximal conversion efficiency. However as Δk becomes non-zero, the energy conversion decreases substantially. Subsequently, the chromatic dispersion relationships of the nonlinear crystals make it nearly impossible to fulfill both phase matching and conservation of energy if all the beams have the same polarization [1]. These dispersion relations can be alleviated through the use of the birefringence displayed by many crystals, which is the dependence of the refractive index of the crystal on the direction of the polarization of the light [22]. For instance, propagating the three beams through the crystal with different polarizations can result in birefringent phase matching (BPM). Different successful variations of BPM include Type I, Type II, critical (angle-tuning), and non-critical (temperature) phase matching. Unfortunately, birefringent phase matching (BPM) can limit the choice of nonlinear crystals, limit the choice of the signal and idler wavelengths, limit the desired tuning range due to insufficient birefringence, and can suffer from spatial walk off of the beams. Also, it is often the case in nonlinear crystals that the d_{33} nonlinear coefficient tends to be much larger than the off-diagonal coefficients [22], which requires that all three beams be polarized in the same direction. This is not compatible with any of the BPM techniques.

This problem can be alleviated through use of periodically poled materials, which utilizes a phase matching technique known as quasi-phase matching (QPM). Periodic poling relies on the coherence length, $l_c = \pi/\Delta k$, which is the maximum distance the three beams with the same polarization can propagate in the nonlinear crystal before they destructively interfere. By periodically inverting the ferroelectric domain of the crystal by 180 degrees every coherence length one can achieve constructive interference with the light from the previous coherence length, resulting in QPM or constructive interference through the length of the crystal, which is illustrated in Figure 11 [1]. This figure shows that BPM still achieves better conversion efficiency than QPM when the nonlinear coefficients are kept constant. However, due to the much larger nonlinear coefficients that can be accessed by periodically poled materials, QPM will result in better conversion efficiency in the end, while allowing for wavelength flexibility, ease of use, ease of phase matching, no spatial walk off, and wide tuning ranges. The phase matching condition for QPM now takes the form [22],

$$k_{pump} - k_{signal} - k_{idler} - \frac{2\pi}{\Lambda} = \Delta k, \tag{3.3}$$

where Λ is the poling period of the periodically poled material. For ideal QPM,

$$\Lambda = 2l_c = {2\pi}\Big/{\left(k_{pump} - k_{signal} - k_{idler}\right)}, \tag{3.4}$$

The powerful feature of periodically poled materials is that from Eqns. (3.2, 3.3, and 3.4) and a specified pump wavelength, the poling period (Λ) can be determined to produce the exact desired wavelengths at the signal and idler. Materials with the desired poling period can then be ordered from a vendor to allow for positioning of either the signal or idler

directly on a molecular absorption feature of interest. It is important to note that from Eqn. (3.2) the *k* vector of each mode has a temperature-dependent index of refraction term which can be used to temperature tune the output wavelengths of the signal and idler pair to accurately locate an absorption resonance or to reach multiple absorption resonances. Also, vendors have recently begun to implement several (2 to 15) different poling period channels on a single nonlinear crystal, which combined with the ability to temperature tune the signal and idler wavelengths, allows for extremely wide tuning ranges (2 μm to 4.5 μm) with a single pump laser and nonlinear crystal.

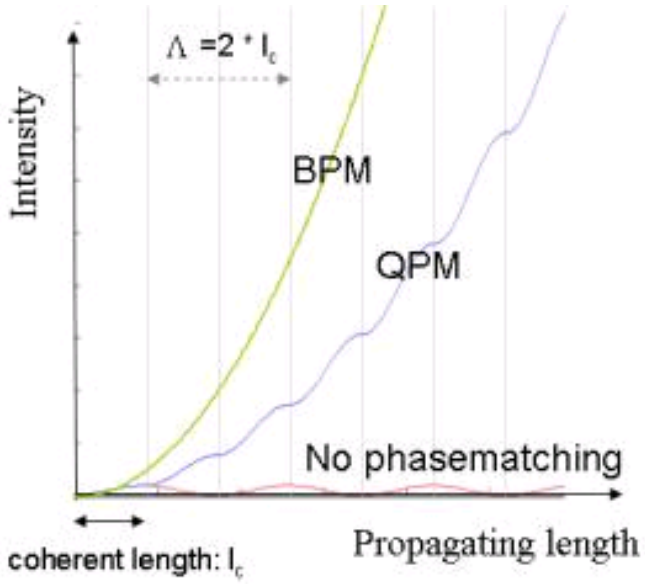

Figure 11. A graph of intensity vs. propagation length in a nonlinear crystal. BPM represents birefringent phase matching, and QPM represent quasi-phase matching. Picture courtesy of HC Photonics.

Optical Parametric Generation Theory

Optical parametric generation (OPG) is defined by a set of three coupled differential equations that explain the growth and depletion of the pump, signal, and idler in a nonlinear optical material. These equations are [22]

$$\frac{\partial A_s}{\partial z} = -\frac{1}{2}\alpha_s A_s + i\kappa_s A_i{}^* A_p e^{-i\Delta kz} \tag{3.5}$$

$$\frac{\partial A_i}{\partial z} = -\frac{1}{2}\alpha_i A_i + i\kappa_i A_s{}^* A_p e^{-i\Delta kz} \tag{3.6}$$

$$\frac{\partial A_p}{\partial z} = -\frac{1}{2}\alpha_p A_p + i\kappa_p A_s A_i e^{i\Delta kz} \tag{3.7}$$

where A_s, A_i, and A_p are the field amplitudes, α_s, α_i, and α_p are the absorption coefficients of the signal, idler, and pump beams, respectively, z is the propagation distance through the nonlinear crystal, and Δk is the phase mismatch of the beams. Also, κ_x is the coupling constant,

$$\kappa_x = \frac{8\pi\omega_x d_{eff}}{n_x c}, \tag{3.8}$$

where x represents the pump, signal, or idler, ω is the frequency, and n is the index of refraction of the nonlinear crystal for the pump, signal, and idler respectively. The initial amplitudes of the field amplitudes are given by,

$$A_s(0) = \sqrt{2\pi I_s(0)/n_s c} \tag{3.9}$$

$$A_i(0) = 0 \tag{3.10}$$

$$A_p(0) = \sqrt{2\pi I_p(0)/n_p c} \tag{3.11}$$

where $I_s(0)$ and $I_p(0)$ are the incident intensities (in ergs/(cm^2 sec)) of the signal and pump, n_s and n_p are the indices of refraction at the signal and pump wavelength, and c is

the speed of light. From these equations it is clear that the amount of frequency converted light directly depends on the intensity of the pump beam, which will be important when selecting nonlinear crystals. For the OPG process, where no signal or idler is input into the crystal, the initial intensity $A_s(0)$ is the effective intensity of a single photon produced through parametric fluorescence. Based on these base equations, there are different complexities of modeling that can be used to explain different aspects of the parametric process. The three models that will be discussed are the Non-Depleted Pump, Depleted Pump, and Multi-Mode models. All three have characteristics that are desirable when attempting to model the OPG process.

Non-Depleted Pump Model

The non-depleted pump model follows the work of Boyd [22] which assumes that the pump is not depleted and can therefore be treated as a constant to simplify the coupled differential equations. This assumption is only valid when a small fraction of the energy has been converted from the pump into the signal and idler beams, as will be shown. The simplified differential equations representing the non-depleted pump model are [22],

$$\frac{\partial A_s}{\partial z} = -\frac{1}{2}\alpha_s A_s + igA_i{}^* e^{i\Delta kz}, \tag{3.12}$$

$$\frac{\partial A_i}{\partial z} = -\frac{1}{2}\alpha_i A_i + igA_s{}^* e^{i\Delta kz}, \tag{3.13}$$

$$g = \kappa A_3(0). \tag{3.14}$$

Where the coupling constant κ now equals [22],

$$\kappa = \frac{8\pi\omega_s\omega_i d_{eff}}{n_s n_i c^2}, \tag{3.15}$$

If we assume a case where we have a single input at the signal wavelength (therefore $A_i(0) = 0$) due to parametric fluorescence, with perfect phase matching, the differential equations can be solved and reduced to [22],

$$A_s(z) = A_s(0)\cosh(gz), \tag{3.16}$$

$$A_i^*(z) = i\sqrt{\frac{n_s\omega_i}{n_i\omega_s}}\frac{A_3}{|A_3|}A_s^*(0)\sinh(gz), \tag{3.17}$$

Later in this chapter it is shown that the non-depleted pump model is reasonably accurate in determining the threshold energy required for frequency conversion for a crystal length *z*, and constant *g* from Eqns. (3.16 and 3.17). A typical plot obtained from this model can be seen in Figure 12; however, because the pump is assumed to be constant, this model is only accurate when the converted energy is a small fraction of the input pump energy. For conversion of a higher fraction of pump light, conservation of energy breaks down. In reality this growth will roll off due to pump depletion, phase mismatch, or other unanticipated effects. Therefore, if one wants to determine the actual conversion efficiency past threshold of the OPG process, more advanced models must be developed.

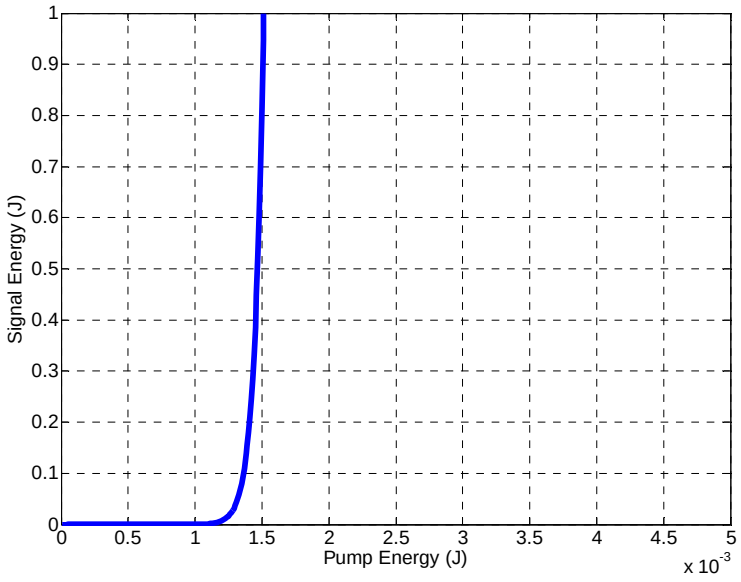

Figure 12. Plot showing the results from the non-depleted pump model. This model is useful in determining the threshold levels of the frequency conversion, but is only accurate when the converted energy is a small fraction of the input pump energy.

Depleted Pump Model

To accurately describe the behavior of the OPG process above threshold, a depleted pump model was developed that considers pump depletion as the pump photons get converted into the signal and idler beams upon propagating through the nonlinear crystal. The three coupled differential equations cannot be solved analytically. Therefore, this model numerically integrates the three coupled differential equations, Eqns. (3.5, 3.6, and 3.7). Upon numerically integrating, the depleted pump model with perfect phase matching shows that after the pump has been depleted, back conversion occurs, resulting in energy going from the signal and idler beams back into the pump beam, and vice versa, as the pump energy is increased. This behavior can be seen in the depleted pump model results presented in Figure 13, which shows the signal (green) and idler (purple)

oscillating with the pump (dotted blue) as a function of input energy. Experimentally, based upon our research as well as research in the literature, results show that upon meeting threshold, the output energy generally follows a linear growth with no back conversion observed. Subsequently, there is disagreement between the depleted pump model and experimental results. Therefore, more advanced models must be developed to accurately model conversion efficiencies.

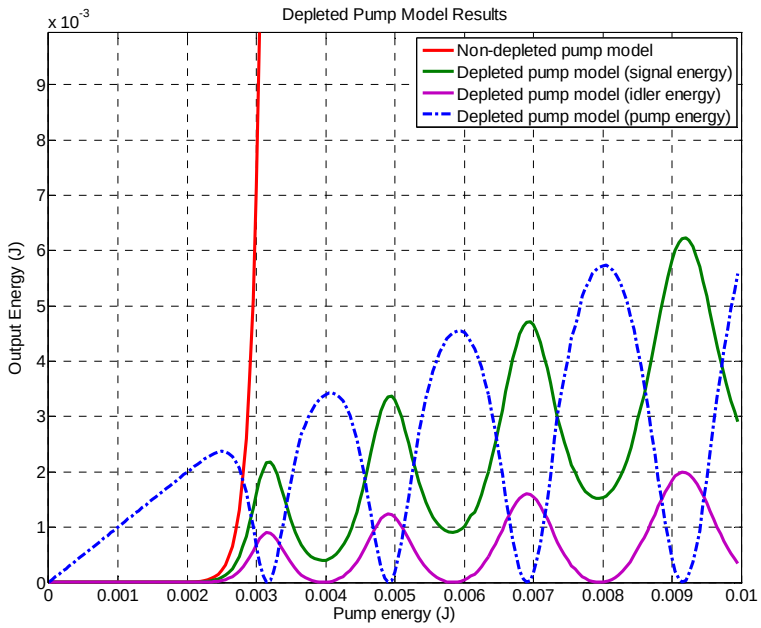

Figure 13. Results from the depleted pump model showing an unpredicted oscillatory conversion / back conversion process.

Multi-Mode Model

To explain the linear growth performance seen in experimental results, a model was developed by Dr. Wm. Randall Babbitt of Montana State University that follows the approach of Guan et al. [23] in considering the effects of multiple spatial modes that can exist in a bulk periodically poled crystal. In the simplest OPG process model, the signal and idler beams are constrained to co-propagate with the pump beam, and therefore these

models assume growth of only a single spatial photon mode. However, in a bulk crystal, the photons can seed multiple on and off-axis modes. Guan et al. [23] showed that by including multiple photon modes (in their case 10 on-axis and 10 off-axis), the model generates an output that grows somewhat more linearly, depending on the parameters used. Therefore, we incorporated multiple photon modes into our model to determine the effects on OPG and OPA performance. The number of modes is adaptable for optimization and the phase mismatch and coupling of the different modes can be varied independently to allow study of a variety of cases, including the effects of a multi-spatial-mode pump. Results from this advanced model begin to show signs of linear growth, similar to that seen in the experiments, when a multitude (~40) of output spatial modes with random phase mismatch were pumped by a multi-spatial-mode pump beam. This large number of spatial modes for the output and pump modes is not consistent with the current experimental conditions. However, due to larger number of modes (~40) and random spread of the input parameters used in the model to achieve these results, little quantitative comparison could be made between the modeling and experimental results. The one quantitative result is that the introduction of multiple pump and output modes into the model did not substantially change the pump threshold for achieving frequency conversion.

Nonlinear Crystal Properties

The modeling efforts were developed to assist in determining the necessary crystal parameters for efficient conversion of the pump laser at 1064 nm to the mid-IR

using the OPG / OPA process. Although the depleted pump and multi-mode models were not as useful as hoped, they both predicted roughly the same pump threshold as the non-depleted pump model. Therefore, the non-depleted pump model was used in determining the necessary crystal parameters to achieve frequency conversion. The parameters of most interest are the crystal length, nonlinear coefficient, and pump intensities that are required to reach frequency conversion threshold. The crystal length is critical due to the theoretical exponential dependence of frequency converted energy on propagation (crystal) length. Also, the amount of converted light depends proportionally on the pump intensity and nonlinear coefficient. However, due to the limited lengths (<50 mm) and nonlinear coefficients (< 16 pm/V) of commercially available periodically poled nonlinear crystals, the non-depleted pump model estimates that pump intensities approaching 1 GW/cm^2 are required to achieve efficient OPG conversion in a single pass configuration.

Such high pump intensities are troublesome for several reasons. First, high intensities can exceed the surface damage threshold of the crystal, which can result in a permanent surface damage of either the input or output facet [25]. Second, high intensities can induce photochromic damage, which is an optically-induced absorption (heating) that can lead to thermal dephasing (preventing efficient frequency conversion), and eventually permanent damage [25]. Examples include gray tracking, photo-darkening, and green-induced infrared absorption (GRIIRA) [24]. The final negative effect is photorefractive damage, or “laser damage,” which is an optically-induced refractive index change. These localized index changes can either distort the

wavefront of the laser beam or scatter optical radiation into various directions, which prevents efficient frequency conversion if not appropriately mitigated [25]. Photochromic and photorefractive damage can be attributed to impurities or intrinsic defects in the nonlinear crystals that occur during the growth process [29]. These troublesome effects must be minimized by proper selection of a nonlinear crystal.

Periodically poled lithium niobate (PPLN) represents the present state of the art for nonlinear frequency conversion of solid-state lasers due to its high nonlinear coefficient, wide wavelength transparency (350 nm – 5500 nm) [26], and relative maturity. However, OPG in PPLN at high intensities has been limited by material issues primarily due to photorefractive damage and GRIIRA. Although GRIIRA effects are most commonly seen in frequency doubling crystals, the effects can also occur in pulsed mid-IR OPA's due to blue or green light generation by parasitic higher-order QPM processes [27]. Fortunately, it has been demonstrated that the photorefractive effects in PPLN can be reduced substantially by operating the crystals well above room temperature (> 120 degrees Celsius), unfortunately this same technique has not been shown to reduce GRIIRA [28]. Recent studies have shown that doping the $LiNbO_3$ (lithium niobate) crystals with small amounts of Magnesium Oxide (MgO) can nearly eliminate the photorefractive and GRIIRA effects through elimination of intrinsic defects by the substitution of Mg on Li sites [27]. As a result of these recent advancements, PPLN and MgO:PPLN have become more viable options for high-power OPG processes. However, due to the impracticality of heating the PPLN crystals well above room temperature in a hand held device to further reduce photorefractive effects, as well as the

low surface damage threshold (~500 MW/cm^2), these crystals are not ideal for long-term, high-power OPG processes.

Alternatively, studies have shown that growing crystals in a nearly stoichiometric composition can reduce the density of defects that are responsible for the damaging photochromic and photorefractive effects seen in congruently grown crystals [29]. As a result, materials grown with nearly stoichiometric composition, and in particular periodically poled nearly stoichiometric lithium tantalate (PPSLT), have been the subject of recent research for high power nonlinear conversion processes. Advantages of nearly stoichiometric lithium tantalate (SLT) over congruent lithium niobate (CLN) include much lower levels of photorefraction and GRIIRA [30,31], a higher surface damage threshold, as well as a comparable nonlinear coefficient. Advantages of SLT over potassium titanyl phosphate (KTP) include a wider wavelength transparency (400 nm - 5500 nm for SLT [32], versus 350 nm – 3000 nm for KTP, see Figure 14) and less susceptibility to gray tracking that is common in pulsed operation in KTP [29].

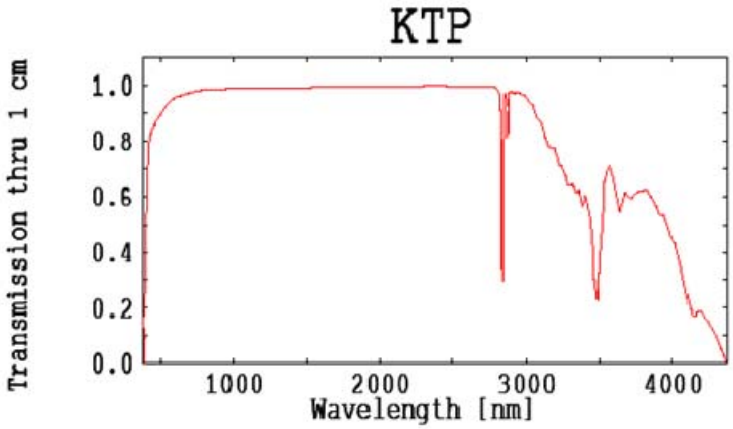

Figure 14. Transmission spectrum of KTP crystals.

Based upon a thorough examination of these nonlinear materials, three different materials were considered according to their ability to operate in a high-power configuration and the current commercial availability: periodically poled congruent lithium niobate (PPCLN and MgO:PPCLN), periodically poled potassium titanyl phosphate (PPKTP), and periodically poled stoichiometric lithium tantalate (PPSLT). Due to the limited mid-IR wavelength transparency of KTP (see Figure 14), the modeling work and experimental validation was limited to PPCLN (and MgO:PPCLN) and PPSLT.

Due to the insufficiencies of the depleted pump model to guide the crystal selection process, sample crystals were obtained from several vendors to provide empirical guidance for crystal selection. The appropriate sample crystals were chosen through use of the non-depleted pump model to determine the necessary length and nonlinear coefficient to achieve threshold with the available pump intensities. Sample crystals were obtained with similar poling periods from a variety of different major crystal vendors, which are summarized in Table 3.

Table 3. A listing of the sample crystals obtained for experimental testing.

Vendor	Crystal Type	Length	Deff
Spectralus	PPCLN	35 mm	16 pm/V
Crystal Technology Inc.	PPCLN	50 mm	16 pm/V
Deltronic Crystal Ind.	PPSLT	55 mm	12 pm/V
HC Photonics	MgO:PPCLN	50 mm	16 pm/V
AdvR	PPKTP	25 mm	7 pm/V

Experimental Setup

To test the performance of the obtained nonlinear crystals, an appropriate experimental setup was constructed. However, to allow for a thorough understanding of the setup, a brief discussion about the Monoblock laser is required.

Monoblock Laser Spatial Mode

The Monoblock laser cavity is constructed in a flat-flat coupler configuration, which allows for ease of manufacturing and compact laser size; unfortunately, this configuration also leads to a higher order spatial mode output beam. Also, due to the properties of the passive Q-switch, the output beam has several localized hot spots rather than a smooth intensity distribution. The spatial mode and intensity distribution of the Monoblock output beam is shown in Figure 15. This image was captured on a CCD camera located ~250 mm from the end of the Monoblock output coupler. This poor spatial mode and intensity distribution of the Monoblock leads to many difficulties in the OPG/OPA process, especially when attempting to seed the OPG process. Therefore, in the initial studies, the Monoblock was spatially filtered with a pinhole to achieve a cleaner (lower-order) spatial mode with a smoother intensity distribution. However, achieving a lower-order spatial mode led to a substantial reduction in the usable pump power. As a result, spatially filtering is undesirable for the final product. However, it is a useful tool when assessing and validating the performance of the OPG/OPA process in the nonlinear crystals.

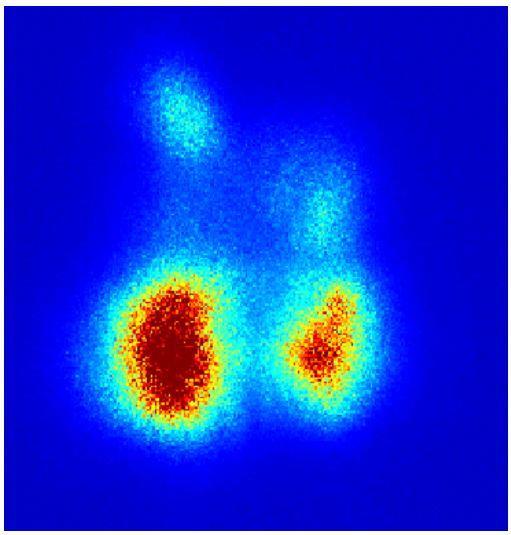

Figure 15. Image from a CCD camera of the poor spatial mode of the Monoblock laser (250 mm after the output coupler).

Experimental Setup

An experimental setup was constructed to allow for spatial filtering of the pump beam if desired, and to test the frequency conversion performance and susceptibility to optical damage of each sample crystal. The constructed experimental setup can be seen in Figure 16. After the Monoblock pump laser, we use a λ/2 waveplate and a polarizing beam splitter (PBS) in combination as a variable pulse energy attenuator for the pump. We use a second λ/2 waveplate to control the polarization of the pump light to align with the correct axis of the nonlinear crystal. The light is then focused using an f = 300-mm bi-convex lens, to allow for spatial filtering of the pump if desired. A “flipper” mirror (dashed line) is used to measure the pump energy prior to conversion to determine the achieved conversion efficiency. The light is then re-collimated using an f = 150-mm plano-convex lens, and immediately focused through the nonlinear crystal using an f = 125-mm plano-convex lens. The appropriate focal length was determined to

approximately match the confocal parameter of the focused beam to the crystal length, and to generate the necessary pump intensity (spot size) to achieve frequency conversion. Alternative lenses to the 125-mm lens could be used to alter the focused spot size, and therefore the pump beam energy density, inside the crystal. A 1.4-μm high pass filter is used after the crystal to filter out the residual pump and parasitic second harmonic generated light, leaving just the signal and idler which are directed onto a broadband pyroelectric energy meter. From this setup, the conversion efficiency of each nonlinear crystal can be determined.

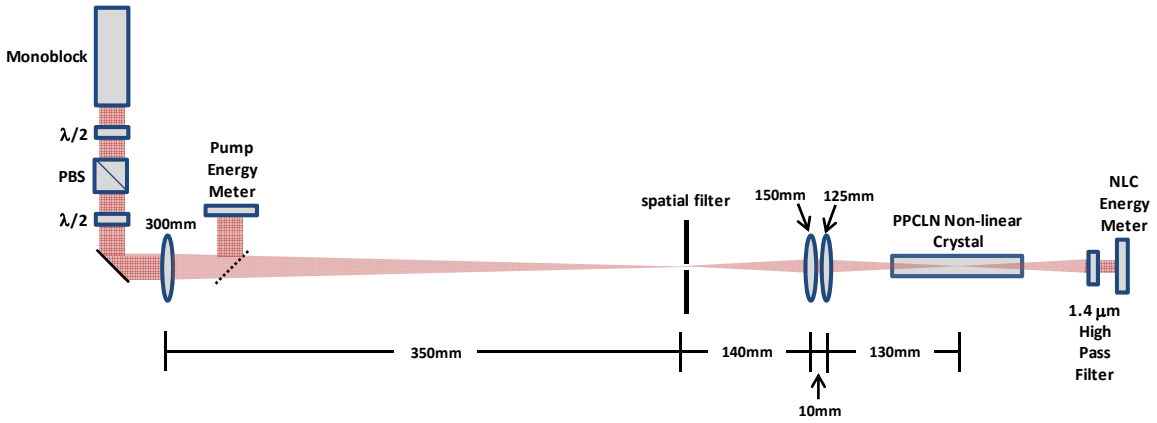

Figure 16. Experimental setup to test the performance of the sample nonlinear crystals.

Experimental Results

The first goal of these experiments was to validate the non-depleted pump model's OPG threshold predictions. To do this, we used the CTI PPCLN sample and measured the output energy from the crystal as the input pump pulse energy was increased. A spatial filter for the pump light was used to improve the spatial quality of the input pump beam, to allow for a better measurement of the pump spot size. As shown

in Figure 17 (red), the OPG threshold occurs at a pump pulse energy of approximately 1.5 mJ. Above threshold, the output energy grows linearly in contrast to the depleted pump predictions presented in Figure 13. Figure 17 includes predictions from the non-depleted pump model for different beam sizes for validation purposes. From the manufacturer we obtained the effective nonlinear coefficient and crystal length of 16 pm/V and 50 mm, respectively. The only other free parameter in our model was the spot size in the crystal. Despite the spatial filtering of the pump beam, precise determination of the beam waist was difficult because higher order components were still present. We used an InGaAs camera to estimate the beam waist ($1/e^2$ radius) at the center of the crystal to be ~160 microns. In Figure 17, we show the model results from three different spot sizes (140, 150, 160 microns). The experimental threshold best matches the model's predictions for the 150-micron spot size. The discrepancy with the model is easily attributed to the uncertainty in the spot size. We performed similar model validations for the PPSLT crystal and obtained similar reasonable agreement.

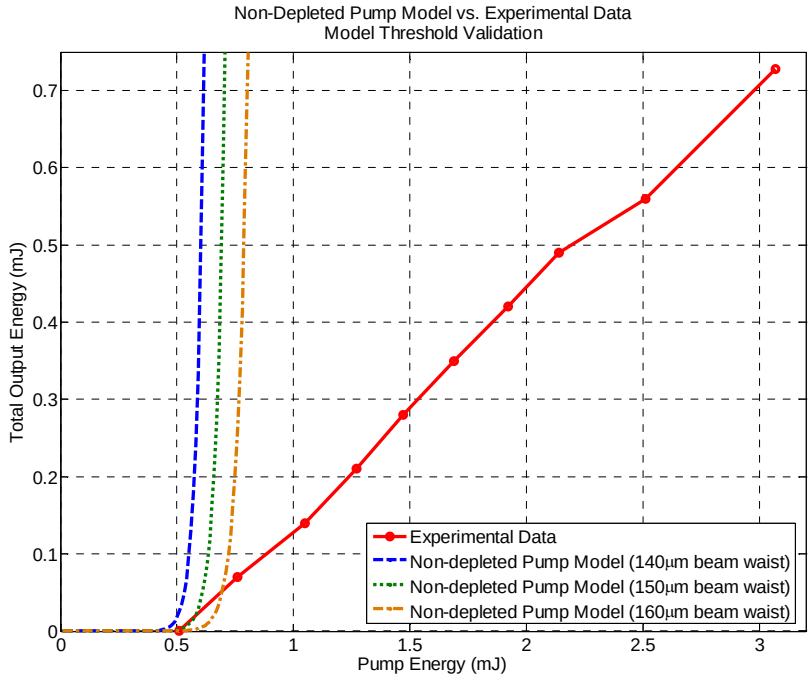

Figure 17. Comparison between experimental data taken with a spatially filtered pump beam, and theoretical data obtained from the non-depleted pump model for three different beam waists.

Next, we tested each of the crystals to determine the achievable output energies and conversion efficiencies. In these experiments, only the conversion efficiency into the signal wavelength was monitored, and the pump was not spatially filtered to allow for maximum pump energies. The first crystal that was tested was the HC Photonics MgO:PPCLN crystal. The results from this experiment can be seen in Figure 18, which had a slope efficiency of 23% before a roll off at ~2.5 mJ of pump energy. To determine if this effect was related to photorefractive damage, the same experiment was performed holding the crystal at room temperature (blue), and at an elevated temperature (green). This experiment concluded that the roll off is not strongly related to temperature. It is therefore likely that the roll off is not due to photorefractive effects. Also, due to the MgO doping, photochromic effects should also not cause this limiting effect.

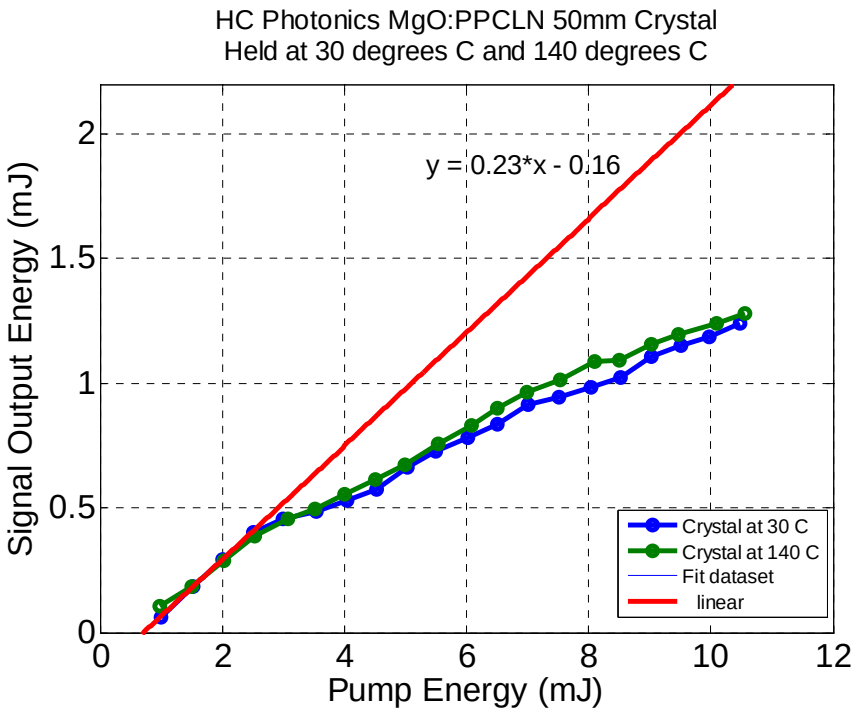

Figure 18. Experimental conversion results from the HC Photonics 50-mm MgO:PPCLN crystal.

To attempt to determine the cause of the roll off, the second 50-mm PPCLN crystal provided by Crystal Technology Inc. was tested, and the results are presented in Figure 19. The crystal was held at an elevated temperature (~160 degrees Celsius). This crystal had a higher initial slope efficiency (32%), but then showed a similar roll off of the conversion efficiency near ~3 mJ, which is consistent with the results obtained from the similar HC Photonics crystal. This result showed that the roll off effect was consistent for similar crystals (d_{eff} and crystal lengths) produced by different manufacturers.

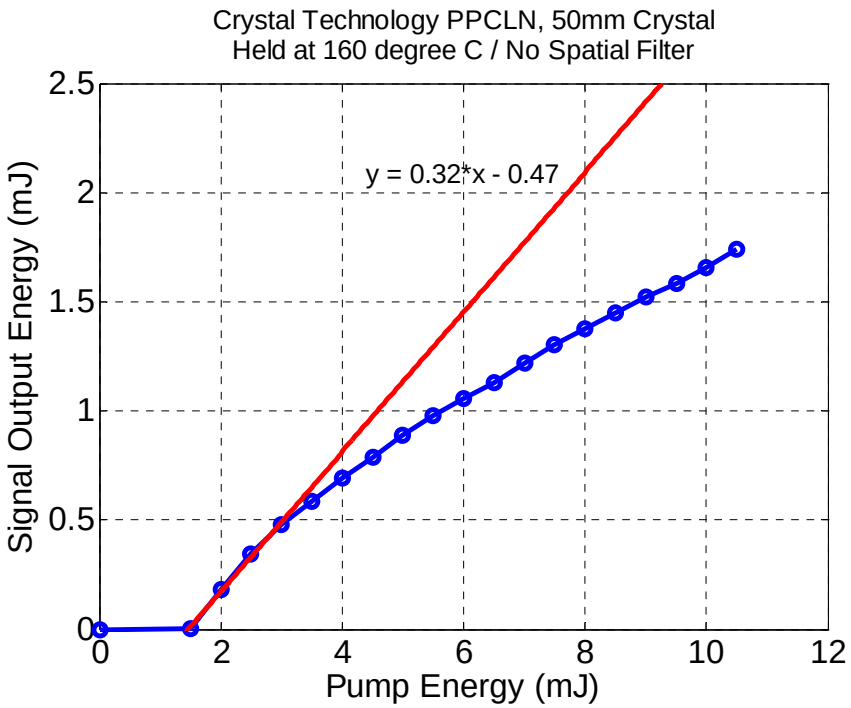

Figure 19. Experimental conversion results from the Crystal Technology Inc. 50-mm PPCLN crystal.

As a comparison to the results from the two 50-mm PPCLN crystals, a 35-mm PPCLN crystal was tested, and the results are presented in Figure 20. This PPCLN crystal was operated at ~150 degrees Celsius. With the 35-mm PPCLN crystal, the roll off in the conversion efficiency was not observed, and linear growth in output energy was observed out to the maximum pump energy with a conversion slope efficiency of ~28%, and a peak conversion of ~26%. Assuming that the growth process, and the density of intrinsic defects are similar between all of the PPCLN crystals, this result leads us to believe that the longer crystal length (propagation distance) is the primary cause of the roll off in the PPCLN crystals. However, we wanted to determine if there was any correlation with the effective nonlinear coefficient.

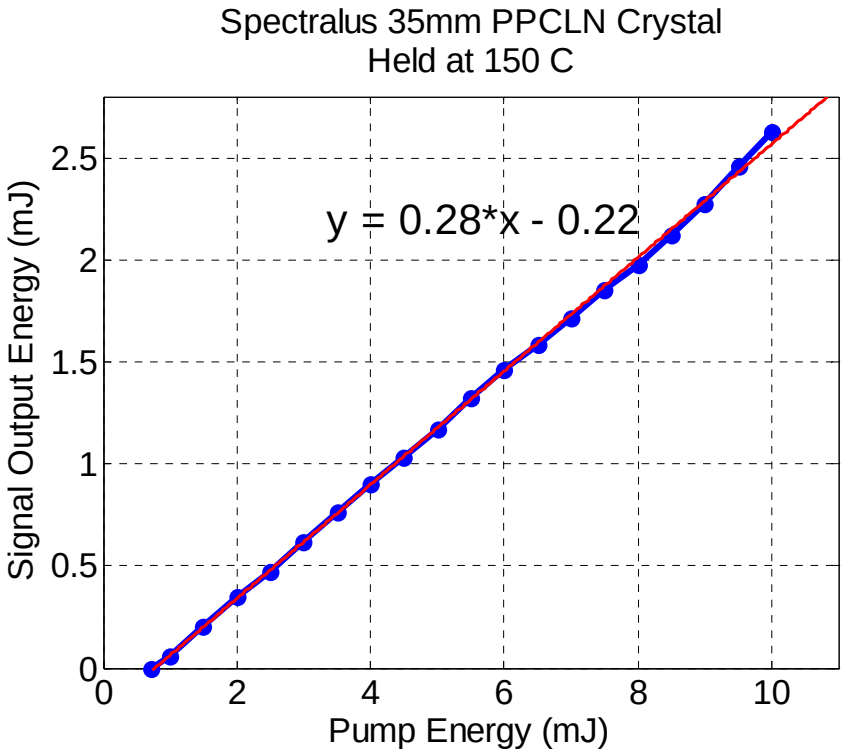

Figure 20. Experimental conversion results from the Spectralus 35-mm PPCLN crystal.

Finally, the PPSLT crystal was tested to determine the performance of this material, as well as test the performance of a material with a lower nonlinear coefficient. The results from these experiments can be seen in Figure 21. Due to the properties of the SLT material, this crystal is not required to be held at an elevated temperature to reduce photorefractive effects; however, the crystal was held at 60 degrees Celsius to match the output wavelengths of the other crystals (~1.5 μm). These results show that in the 55-mm PPSLT crystal we see no roll off in the conversion efficiency and a linear energy growth out to the maximum pump energy with a conversion slope efficiency of ~25%, and a peak conversion of ~23%. This result indicates that the roll off may be limited to crystals with long lengths and large nonlinear coefficients.

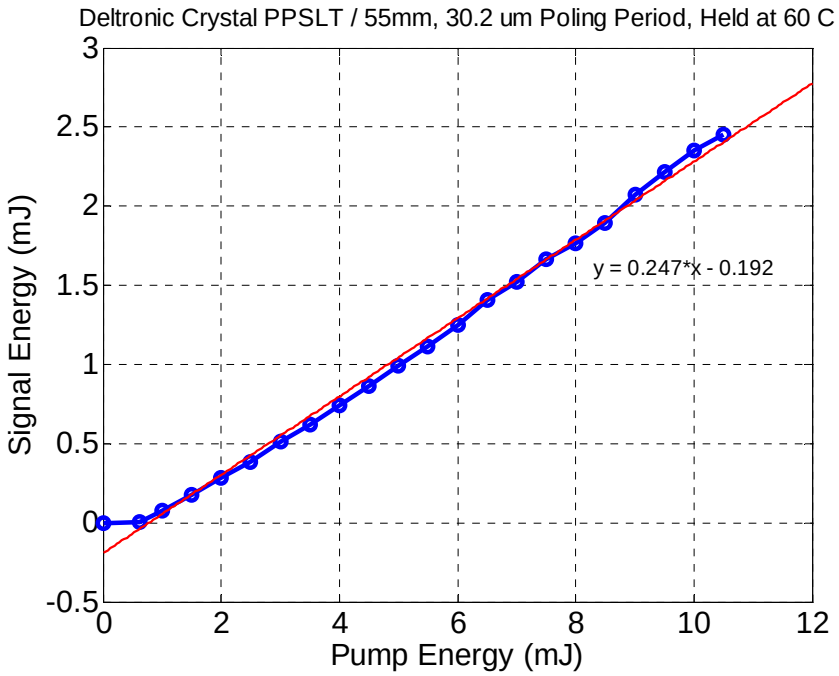

Figure 21. Experimental conversion results from the 55-mm PPSLT crystal.

Due to the lack of data on PPSLT in literature, we also wanted to measure the amount of energy in the idler beam to verify that the SLT material does not absorb light at longer wavelengths. The idler energy was measured by implementing a 3-μm high pass filter before the energy meter to block the pump, parasitic second harmonic generation, and signal wavelengths. The idler energy was found to be ~1mJ or ~40% of the signal energy, which is consistent because the percentage of the idler energy relative to the signal energy should be the ratio of the two wavelengths (1.55-μm signal, 3.39-μm idler) which is ~46%. The slight drop in the percentage from the theoretical value could be due to slight errors in the measurement or a small fraction of absorption occurring.

The results from the four samples show that the crystals with a long length and large nonlinear coefficient exhibit a roll off in the conversion efficiency, while the short crystal with a large nonlinear coefficient and the long crystal with a small nonlinear

coefficient do not. Although the number of crystals we were able to test was small, the data indicates that longer crystals with higher nonlinear coefficients are more likely to exhibit the conversion efficiency roll off. Powers et al [33] present findings in their work concluding that nonlinear crystals with long lengths and large nonlinear coefficients are more susceptible to the growth of noncollinear processes due to the high conversion susceptibility (high gain) and long interaction lengths. They conclude that the noncollinear processes could potentially steal gain from the collinear processes, which may explain our roll off effect. They also conclude that the noncollinear effects can be reduced by using crystals with long lengths and low nonlinear coefficients. Although the correlation is inconclusive, their work tends to agree qualitatively with our experimental data obtained with the PPLN and PPSLT crystals. Regardless, our experimental data, combined with the work of Powers et al [33], led us to prefer PPSLT for our nonlinear conversion requirements due to PPSLT's high surface damage threshold, lower susceptibility to photorefractive and photochromic effects, lower nonlinear coefficient (potentially less susceptibility to noncollinear effects), and the potential for room temperature operation with efficient conversion and high energy output.

CHAPTER 4

OPTICAL PARAMETRIC AMPLIFICATION

This chapter describes the processes involved with narrowing the broadband OPG emission by means of a seeding, which is often referred to as optical parametric amplification. This portion of the work performed in this thesis is critical because narrowband emission is essential for high-resolution mid-IR spectroscopy. A majority of the discussion and results presented in the chapter are devoted to experimental results. While an advanced theoretical model would help to fully understand the performance of an OPA configuration, it was not a primary focus of this thesis work. Results presented in this chapter show the ability to produce narrowband emission from our developed mid-IR laser source, with the proper linewidths to perform high-resolution mid-IR spectroscopy. Finally, advanced seeding techniques are demonstrated that could allow for simultaneous DIAL measurements with a single laser source.

Motivation / Laser Requirements

Although the OPG configuration allows for sufficient energy conversion into the mid-IR, its frequency bandwidth is too broad (>150 GHz) for high-resolution mid-IR spectroscopy applications. As shown in Figure 22, which was obtained from the HITRAN database [3], typical atmospherically broadened molecular absorption features in the mid-IR are < 3.5 GHz (~0.14 nm at 3.4 μm) FWHM. The OPG output bandwidth is dictated by the phase matching bandwidth of the material which says that the phase

matching condition presented in Chapter 2 allows for growth of a broad bandwidth of signal and idler wavelength pairs rather than just a single pair. The major difficulties with this broadband output can be seen visually in Figure 23, which shows the measured output of the OPG process on an OSA (blue), compared to (red) a trace that simulates the approximate width of a typical molecular absorption feature. Clearly only a very small portion of the total energy will get absorbed by the narrowband molecular absorption feature, thus the sensitivity of the lidar system is severely degraded for discriminating the "on" and "off" wavelengths in a DIAL configuration. The broadband emission could also be absorbed by closely spaced neighboring species, which could corrupt the measurement and result in false positive detections of gas effluents. Therefore, to maximize the sensitivity of the lidar system, as well as eliminate the possibilities of false positive measurements, the output bandwidth of the mid-IR laser must be less than ~3.5 GHz.

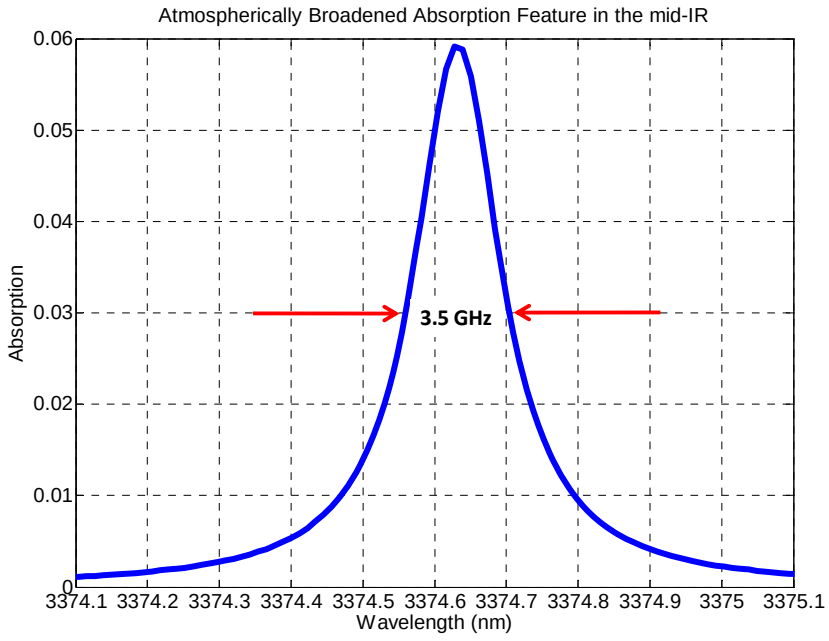

Figure 22. Plot showing a typical absorption bandwidth of 3.5 GHz (0.14nm) of a molecular absorption feature in the mid-IR, obtained from HITRAN database.

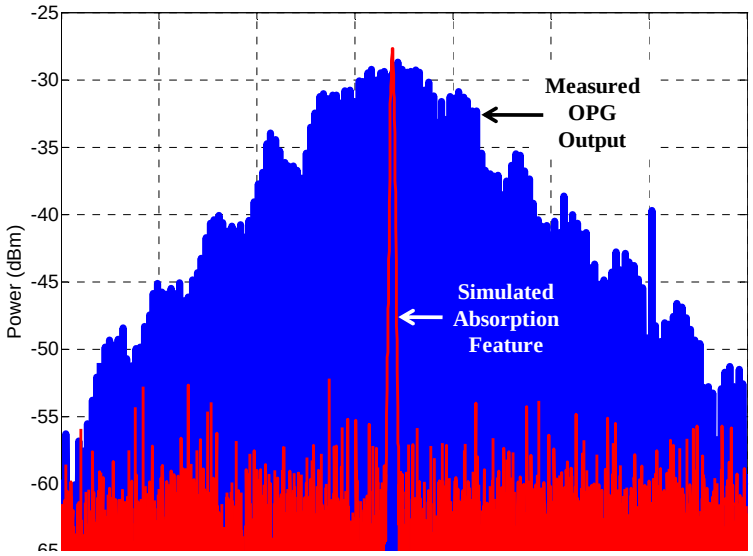

Figure 23. Plot of the measured broadband output of the OPG process (blue), compared to simulated absorption feature (red).

Optical Parametric Amplification Theory

Due to the limitations of the broadband output from the OPG process alone, some means of bandwidth reduction is necessary. One approach to narrowing the OPG output has been realized through seeding of the OPG process, often referred to as optical parametric amplification (OPA). In this process a seed laser, either pulsed [34] or CW [35], with a wavelength that falls within the phase matching bandwidth of either the signal or idler, is spatially overlapped or “mode matched” with the pump beam at the input of the nonlinear crystal. Theoretically, when the pump and the seed are properly mode matched, and there is enough energy in the seed to overcome the energy of a spontaneously emitted photon generated through parametric fluorescence, the output bandwidth and divergence of the OPG (signal and idler) are controlled by the bandwidth and divergence of the seed laser [33].

Theoretically, OPA can be modeled through use of Eqns. (3.12 – 3.17), as was done for the non-depleted pump. However, rather than assuming the initial seed energy $A_s(0)$ is the energy of a single spontaneous fluorescence photon, in an OPA configuration $A_s(0)$ represents the amount of energy in the CW seed beam during the duration of the pump pulse. Non-depleted pump theory for OPA predicts that we should see the threshold level of the OPG process drop substantially when seeding, however experimentally we have not seen this effect. Also, advanced modeling is necessary to predict the performance of the features of interest of OPA which are the bandwidth and beam divergence reduction. As a result, we relied heavily on experimental results to determine the performance of the OPA seeding process.

Experimental Setup

The experimental setup that was used to "mode match" the seed and pump lasers, and test the seeding performance can be seen in Figure 24. This setup is nearly identical to the setup described in Chapter 3 (see Figure 16, and corresponding write up) for the nonlinear crystal testing experiments, with the addition of the necessary optics to achieve seeding. It can be seen from this setup that by use of a dichroic mirror we can combine the pump and seed beams with very little loss in optical power of each source. The mirrors prior to the dichroic mirror are used to maximize the spatial overlap between the pump and seed beams. Once again, this setup allows for spatial filtering of the pump beam if desired. Depending on the polarization of the seed laser, a $\lambda/2$ waveplate can be

used to ensure alignment of the seed and pump polarizations, which is critical to achieve seeding.

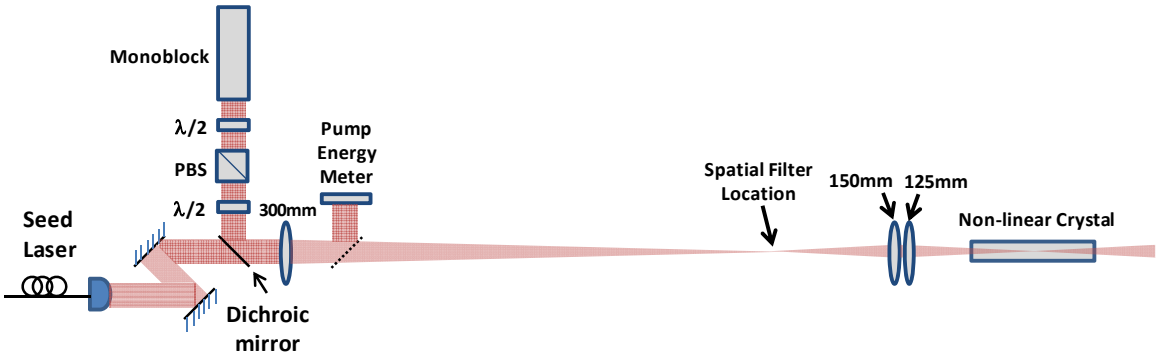

Figure 24. Experimental setup to achieve narrowband emission via seeding (OPA).

After the nonlinear crystal, the light is collected into a fiber and two different methods can be utilized to analyze the seeding performance. The first method involves monitoring the emission spectra on an optical spectrum analyzer (OSA) operating in pulsed mode. In pulsed mode the OSA conducts a wavelength scan over the anticipated phase matching bandwidth and dwells for 100 ms every 0.01 nm increment, resulting in a resolution of ~0.1nm. This is a relatively simple technique to verify if the OPG process is seeded. Unfortunately, this technique has an update rate on the order of minutes per scan which does not allow for real time monitoring or optimization of the seeding. Also, this approach does not allow for a quantitative analysis of the seeding efficiency. As a result, a second method was developed to allow for real-time optimization, and analysis of the seeding performance. This method uses a high-resolution monochromator to perform the analysis; however, this method required additional development.

Monochromator Technique

The monochromator device uses a high-resolution diffraction grating to achieve spectral resolutions of ~0.12 nm out to ~2.0 μm. This grating, along with complementary optics allows for real time optimization and analysis of the seeding efficiency of the OPG/OPA process. The layout of the monochromator can be seen in Figure 25. To simplify the light input mechanism into the monochromator we used a fiber at the input, which also serves to diffract the light to increase the device resolution (larger spot on grating results in better resolution). The diffracted light is directed onto a mirror (collimating mirror) to collimate the light, which is then reflected onto the diffraction grating where the light is spectrally separated by the grating. The spectrally separated light is then directed onto another mirror (focusing mirror) which focuses the spectrally resolved light onto the exit slit. The diffraction grating angle can then be tuned to select which wavelength, within ~0.12 nm, is output from the device.

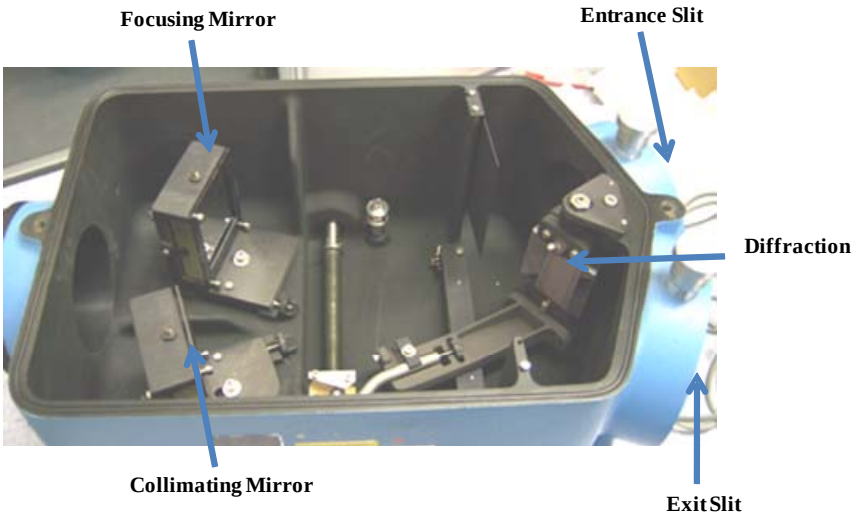

Figure 25. Picture showing the layout of the monochromator device.

Prior to use, the monochromator had to be fully calibrated to allow for accurate determination of the wavelength of the output light. To accomplish this, three DFB lasers at different wavelengths (1064nm, 1508nm, and 1550nm) were passed through the device and the monochromator's counter value was recorded for each laser. The wavelength of each DFB laser was measured using an optical spectrum analyzer (OSA). Based upon these values a calibration curve was constructed, which can be seen in Figure 26.

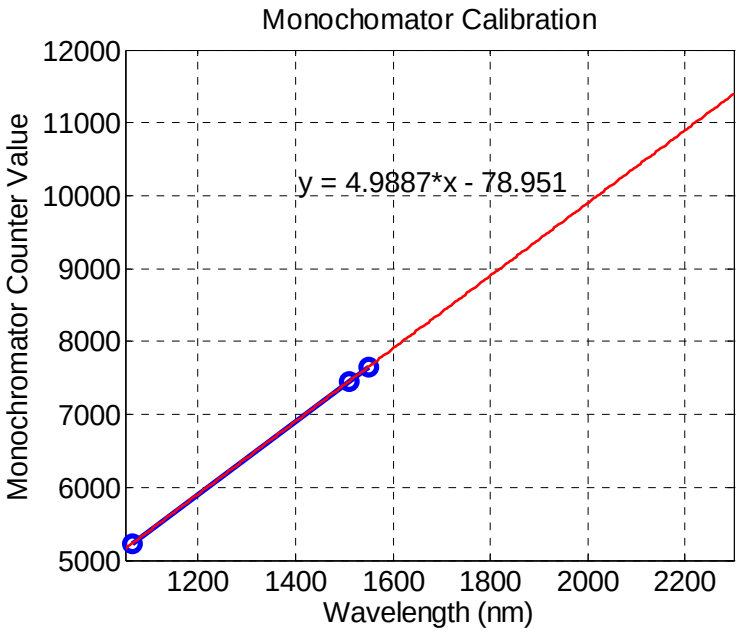

Figure 26. Curve representing the monochromator calibration.

To verify seeding and to quantify the seeding efficiency, the setup shown in Figure 27 was constructed around the monochromator. This setup has two paths, one which directs the light out of the monochromator onto a photodetector (red path), and the other which directs light out of a fiber coupler onto the same photodetector (yellow path). A "flipper" mirror is used in the "red path" to allow us to choose which path is directed onto the photodetector. Seeding verification is performed using the "red path." When the

OPG process is not seeded, only a very small fraction of the broadband energy in the monochromator will exit the device, resulting in low powers observed on the photodetector. When the OPG process is seeded with perfect efficiency, theoretically all of the energy should exit the monochromator, resulting in a significant power increase observed on the photodetector. With this setup the seeding efficiency can be optimized by monitoring and optimizing the power on the photodetector.

Quantifying the seeding efficiency utilizes the "calibration path", shown in Figure 27 (yellow path). The "calibration path" allows for a comparison between the total energy (yellow path) and the percentage of light that gets through the narrowband exit slit on the monochromator (red path). The ratio signifies the percentage of the total energy that is efficiently seeded.

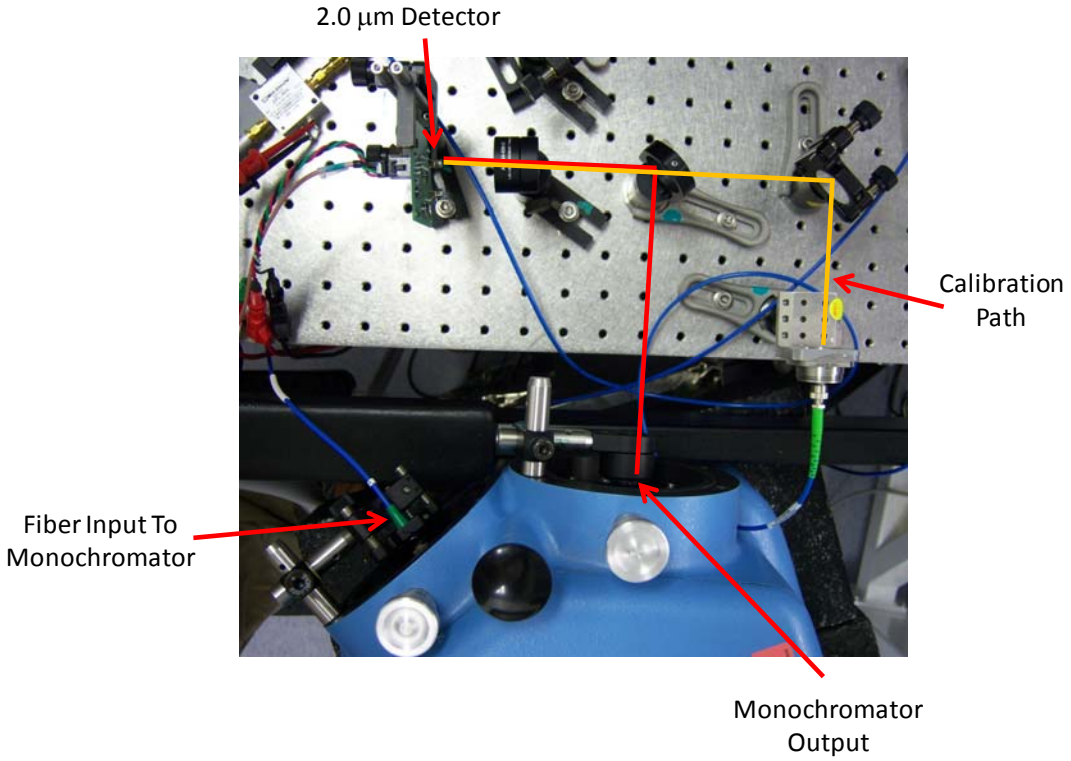

Figure 27. Seeding validation and measurement setup.

The following procedure was created to quantify the percentage of the total energy that is efficiently seeded using the setup shown in Figure 27.

1. Pass the seed light through the calibration path (yellow path) to determine the total amount of narrowband CW power.
2. Pass the seed light through the monochromator (red path), via the fiber input to determine the transmission loss from the mirrors and diffraction grating inside the device. Because the seed laser is narrowband it will pass directly through the exit slit without any additional loss. This transmission loss determines the maximum percentage of light we would expect to see when measuring the pulses.
3. Pass the OPG/OPA pulsed light from the non linear crystal through the calibration path (yellow path) to determine the total amount of pulsed light.
4. Pass the OPG/OPA pulsed light through the monochromator (red path) and measure the total amount of pulsed light at the output.
5. Multiply the total signal pulse energy, found in step 3, by the transmission loss, found from steps 1 and 2. This determines the theoretical maximum output signal energy which would occur if we had 100% seeding efficiency.
6. Divide the pulse energy measured in step 4 by the theoretical maximum found in step 5. This determines the percentage of light that has been converted to narrowband through the OPA process (seeding efficiency).

Experimental Results

A series of experiments were conducted to verify seeding and quantify the seeding efficiency. We initially conducted experiments to simply verify the ability to achieve narrowband emission, and then progressed to experiments to quantify the amount of narrowband emission that could be achieved (seeding efficiency). We then performed heterodyne experiments to determine the linewidth of the narrowband emission. Finally, we conducted proof of concept experiments on a "dual-wavelength" seeding technique that could potentially allow for simultaneous DIAL measurements.

Single-Wavelength Seeding

Initially, the goal was to prove the ability to achieve narrowband emission from the mid-IR laser source through seeding (OPA). These experiments utilized the OSA approach to seeding verification. The results from this approach can be seen in Figure 28. In this plot the blue trace represents the signal without seeding, and the red trace represents the signal with seeding. The results show "narrowing" of the output emission when seeded, which verified that we were actually achieving narrowband emission at the signal wavelength. However, with the OSA we were unable to optimize the seeding or quantify the seeding efficiency.

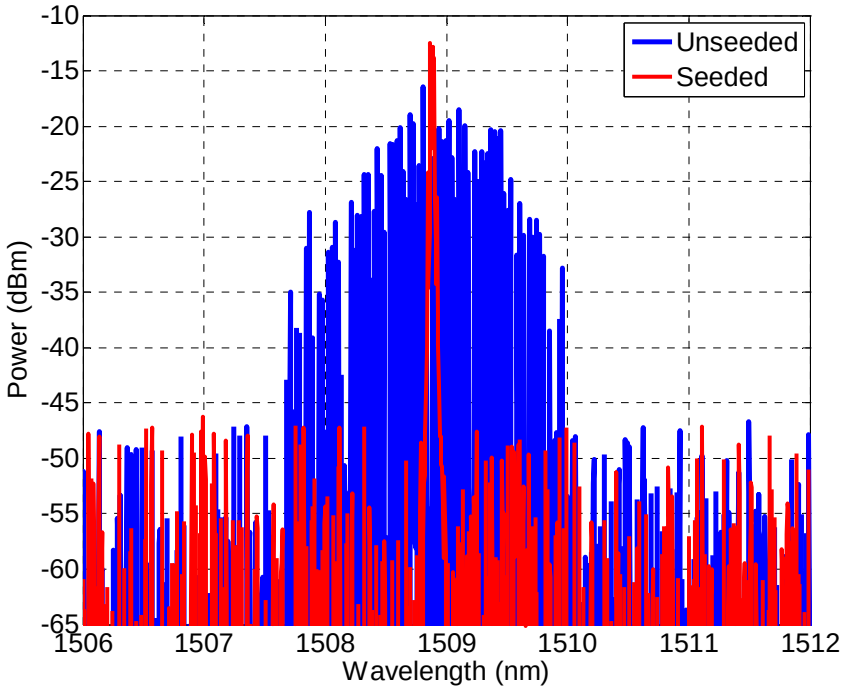

Figure 28. Plot showing data obtained using an OSA in pulsed mode that verifies the ability to seed the OPG process and achieve narrowband emission.

Due to the weaknesses of the OSA approach, the monochromator technique was developed. The results from seeding verification experiments with the approach can be seen in Figure 29. To obtain these results we simply passed the signal light through the monochromator, and measured the output light on a photodetector with (blue) and without (red) seeding. These results show that when the seed laser is blocked, very little signal light is measured at the output of the monochromator (red) due to the broad spectrum of the light, and when seeding a large spike in power is seen (blue) due to the large amount of energy located in a narrowband spectrum. This approach verified the results seen with the OSA. The benefit of this approach is that the verification was performed real time, and allowed us to optimize the seeding.

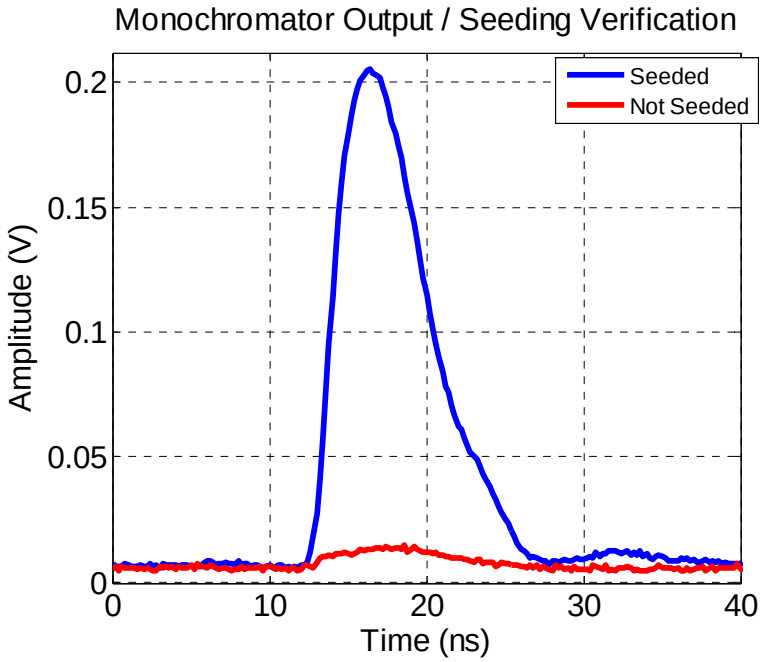

Figure 29. Plot showing seeding verification through use of a monochromator.

Upon verification and optimization of seeding, the seeding efficiency was measured using the 6 step procedure outlined earlier in this chapter. Based upon the discussions in Chapter 3 regarding the spatial mode of the Monoblock laser, we were especially interested in the achievable seeding efficiency when the Monoblock was not spatially filtered. The seeding efficiency relies directly on how well we can mode match the pump and the seed, which is difficult due to the complex spatial pattern of the pump beam when not filtered (see Figure 15). For comparison, data was acquired with and without spatial filtering of the Monoblock utilizing the experimental setup shown in Figure 24 and the monochromator. The results from these experiments can be seen in Figure 30. The red trace represents the seeding efficiency as a function of seed power without spatial filtering, and the blue trace represents the seeding efficiency as a function of seed power with spatial filtering. These results show a significant increase in the

achievable seeding efficiency when spatial filtering the pump beam, which resulted in a maximum seeding efficiency of ~63% for the spatially filtered case, and a maximum seeding efficiency of ~35% without spatial filtering. In these experiments, we measured ~200 μJ of signal energy for the spatially filtered data with ~3 mJ of pump energy, and we measured ~1 mJ of signal energy for the non-spatially filtered data with ~3 mJ of pump energy. The output signal energy discrepancy is due to the increase in pump energy before the crystal when the spatial filter is removed. As anticipated, we observed degradation in the seeding efficiency because of the difficulties associated with mode matching the seed laser to all of the higher orders in the pump beam. However, we do see a relatively linear increase in the seeding efficiency with seed optical power (log scale), which indicates that in the future we can seed with more optical power to increase the seeding efficiency. Extensive research will be devoted to this issue in future work to improve the seeding efficiency without spatial filtering.

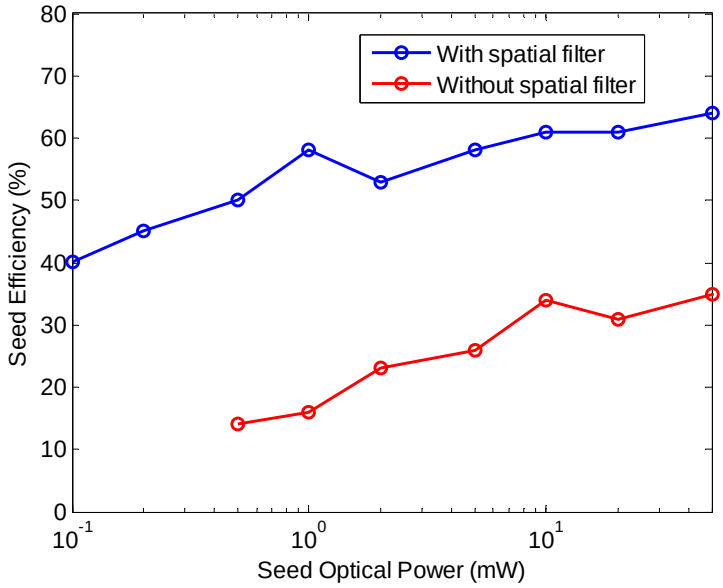

Figure 30. Plot showing the achievable seeding efficiency with and without spatial filtering of the pump beam.

Linewidth Measurements

Measurements were performed to determine the linewidth of the generated OPG/OPA light. To accomplish this measurement, we conducted a heterodyne experiment where we optically mixed the narrowband signal output, which was seeded with a CW 1508 nm DFB laser, with a separate CW 1508 nm stable DFB laser (< 10 MHz linewidth). The subsequent heterodyne signal was detected with a 26-GHz New Focus Detector, and the pulses were digitized and captured using a Tektronix 3-GHz fast digitizer operating at the maximum sample rate. The linewidth of the idler was not measured directly due to the lack of a suitable laser source to perform the heterodyne experiment. The results of these experiments can be seen in Figure 31. The subset of this figure represents the captured time domain heterodyne signal (blue), and a representative trace of the signal pulse (red). The main figure shows the Fourier Transform of the heterodyne signal, which shows a measured linewidth of < 200 MHz FWHM. This emission characteristic is critical in enabling this lidar system to perform high-resolution spectroscopy of gas effluents in the mid-IR.

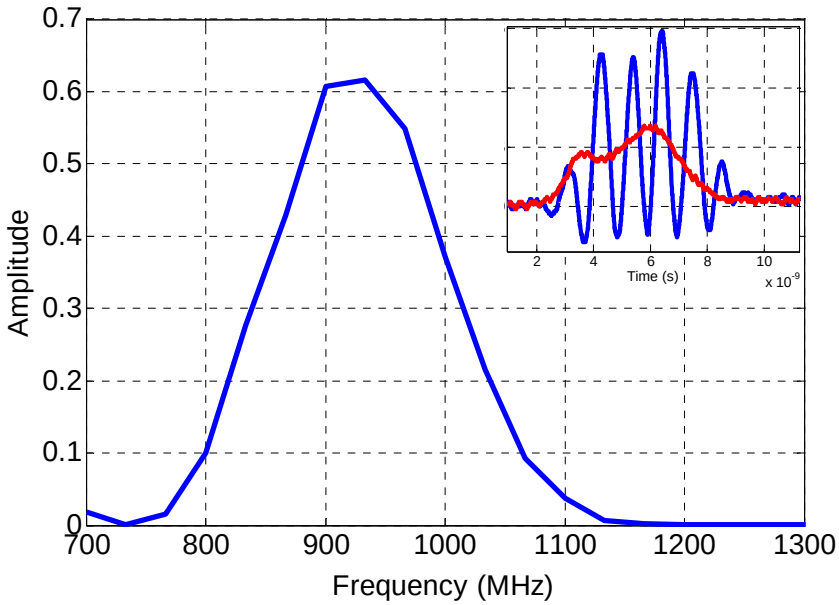

Figure 31. The results of a heterodyne experiment that was conducted to measure the linewidth of the seeded narrowband OPG signal emission. The inset shows the time domain capture of the heterodyne signal (blue), as well as a sample trace of the signal pulse (red). The main figure shows the Fourier Transform of the time domain heterodyne signal, which shows a measured signal linewidth of ~200 MHz (FWHM).

The Monoblock linewidth was also measured via a delayed self heterodyne experiment. The Fourier Transforms of several time domain captures of the heterodyne signal from this experiment can be seen in Figure 32. These results show an upper limit linewidth of the Monoblock of ~250 MHz. From the measured pump and signal linewidths, the linewidth of the idler can be estimated by the equation,

$$\sigma_i^2 = \sigma_p^2 + \sigma_s^2, \tag{4.1}$$

where σ is the linewidth of the pump, signal, and idler respectively. Based upon Eqn. (4.1) the idler is estimated to be ~ 320 MHz. Therefore both the signal and idler can achieve the linewidth requirements necessary to perform high-resolution mid-IR spectroscopy.

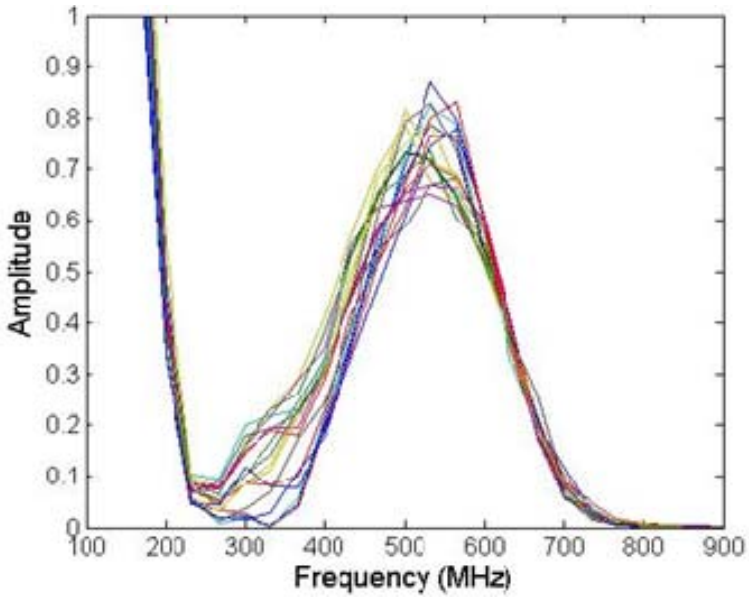

Figure 32. Result showing the measured linewidth of the Monoblock laser. These results were obtained by performing a delayed-self-heterodyne experiment.

Dual-Wavelength Seeding

Experiments were conducted to determine the feasibility of a dual-wavelength seeding technique. Theoretically, by placing two spectrally separated seed lasers within the phase matching bandwidth, two signal (and idler) wavelengths will be created, separated by the seed laser separation. This would allow for simultaneous DIAL measurements with a single laser source. To conduct the proof of concept experiments, two CW DFB diode lasers located at 1508 nm with ~8 mW of optical power each were summed using a 50/50 PM fiber splitter, and the output of the splitter was spatially overlapped or “mode matched” with the pump beam to allow for seeding. The two wavelengths were separated by about 1 nm, which is enough to enable spectral separation upon return from the target, but is not so large that the wavelengths will experience different scattering coefficients from topographical scatterers. To verify dual-wavelength

seeding, the output of the nonlinear crystal was fiber coupled and directed onto an OSA. The results from this can be seen in Figure 33. The blue trace represents the OPG output without seeding, and the red trace represents the seeded OPG/OPA output with dual-wavelength seeding. This result shows that both seed wavelengths receive gain, and narrowing is seen at two distinct signal wavelengths. Mixing terms can also be observed in the spectrum, but will not play a role since they are small in magnitude and spectrally selective detection will be used in the back-end receiver. This result demonstrated the feasibility of operating in a dual-wavelength seed configuration, and could potentially allow for simultaneous DIAL measurements with a single laser source.

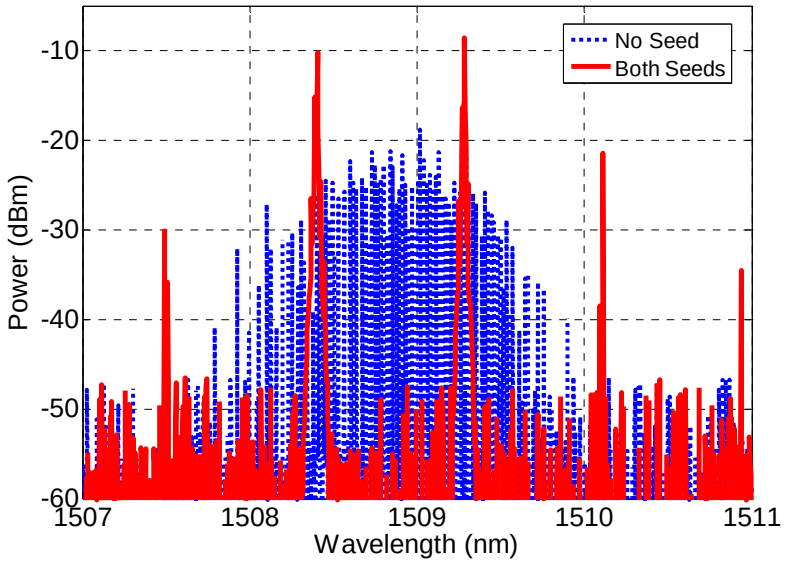

Figure 33. Results of a dual-wavelength seeding proof-of-concept experiment using a PPLN crystal with two DFB diode lasers separated by ~1nm.

We hoped that strong correlations would exist between the two wavelengths so that the pulses could simply be subtracted on return to provide sensitive differential measurements. However, upon further investigation the gain seemed to fluctuate between

the two signal wavelengths. It became apparent that the two wavelengths compete for the gain, and strong correlation between the two wavelengths was not observed. To compensate for the lack of correlation, we showed that by sampling the energy in each wavelength prior to transmission to the target we could reliably calibrate out the energy difference on the return pulses. This calibration was shown to produce a maximum standard deviation of the calibrated pulse peak height of 0.33% (1 part in 330). This error was shown to be dominated by noise in the back-end digitizer. Unfortunately, this error will degrade the SNR that can be achieved by the lidar system. Therefore, extensive research will be devoted to this research area to optimize the correlation between the two wavelengths, and/or improve the back-end processing to allow for high-resolution measurements.

CHAPTER 5

SYSTEM COMPONENTS

This chapter describes the system level component design and construction required to achieve optimal performance of the mid-IR laser source. At the core of this discussion is the development of components to achieve the absolute wavelength stability necessary to perform high-resolution atmospheric detection of gas effluents. Also described is the development of diode pumping to increase measurement times and the backend detection and processing components to achieve high-resolution results.

Component Requirements

To achieve the required performance for each application, many critical system-level components were designed and constructed. Although the meth and CO_2 applications are similar, several of the components on the system level are different for the two systems due to dissimilarities in the applications. A summary of the required system components for each application is shown in Table 4. This table shows that both applications will likely utilize diode pumping of the Monoblock, Monoblock temperature control, and crystal temperature control, which are discussed in detail in this chapter. However, the backend of the two systems will require different means to detect and process the return lidar signals. These differences and the approaches taken for each application are discussed in detail in this chapter.

Table 4. This table lists the required system level components for the meth and CO_2 applications.

System Component	Meth Detection	CO_2 Monitoring
Diode Pumping of Monoblock	x	x
Monoblock Temp. Mitigation and Mounting	x	x
Crystal Temp. Control	x	x
Range Resolved Diff. Detection		x
Single Point Diff. Detection	x	
High Speed ADC / FPGA		x
Gated Integrator	x	

Diode Pumping

Diode pumping of the Monoblock laser is used rather than flashlamp pumping to achieve increased repetition rates upwards of 20 Hz. The increased repetition rates will allow for more rapid measurements, as well as the possibility of averaging many shots to increase the SNR of the measurements. Experimentally, flashlamp pumping was limited to repetition rates of ~0.07 Hz due to the flashlamp circuitry, which made system development very difficult. This led to the implementation of diode pumping for system development and the prototype devices. However, for the proposed applications, flashlamp pumping can be an adequate solution if improvements are made to the circuitry to allow for ~1 Hz repetition rates. Flashlamp pumping significantly reduces system cost and complexity at the expense of higher repetition rates. Regardless, for the current systems diode pumping will be utilized due to the existing issues with the flashlamp circuitry. The power requirement for the diode pumping is ~1000 Watts at 808 nm for pulse durations of 250 μs (upper-state lifetime of the Monoblock gain medium). This is the amount of energy required to achieve the proper population inversion in the Monoblock gain medium. This is achieved through use of a 5-bar, 1000 W Quasi-CW

(QCW) diode array. The combination of the diode array and Monoblock requires a current driver capable of driving 140 amps to the diode array for pulse durations of 250 μs at 20Hz repetition rates, while maintaining a small form factor. Fortunately, OptiSwitch Technology's has recently released a compact, light-weight pulsed current source, which can be seen in Figure 34. Their PLD-200-ULW unit can achieve 200 amps of peak current for pulse durations of 300 μs. The pulse repetition frequency can be varied from single shot to 20 pulses per second (PPS), which is well suited to the power-handling capacity of the Monoblock. The driver's pulse width is controlled by a digital input. The driver can be battery operated with 6 DL123 batteries for 38 minutes continuously at 20 Hz, 200 A, and 300 μs. Or, if operating at a repetition rates of 1 Hz, the unit can achieve over 12 hours of continuous operation on one charge, which should easily suffice for times when the unit is away from its charging station. It is not anticipated that the system will be operated continuously, but rather we assume it will be operated in short bursts. Therefore, we anticipate that this unit will achieve >12 hours of limited operation on a single charge, even at 10 Hz repetition rates.

Figure 34. Picture of the PLD-200-ULW current driver used to drive the diode stack necessary for diode pumping the Monoblock pump laser.

Monoblock Temperature Mitigation and Mounting

Temperature Mitigation

Temperature mitigation must be applied for both temperature control and heat removal. Temperature control is required to stabilize the operating temperature of the Monoblock, which is critical in the meth detection application. Heat removal is required to remove excess heat from the laser on a shot-to-shot basis to maintain a constant operating temperature, which is critical for both applications if higher repetition rates are desired.

Temperature control is required for the meth detection application, but is not critical for the CO_2 monitoring application for the following reason. The difference lies in the fact that meth detection uses the idler wavelength for gas detection, due to the location of the absorption lines of interest being further into the mid-IR (3 μm to 5 μm), and CO_2 monitoring will use signal because of its the 2.0-μm absorption line (which is near the end of the signals range with our pump wavelength). Due to the lack of suitable seed sources in the mid-IR from 3 μm to 5 μm, both applications will be seeded at the lower-wavelength signal. Therefore, for CO_2 monitoring the absolute wavelength stability of the signal is controlled by the spectrally stable seed laser, and has very little dependence on the Monoblock wavelength stability. In contrast, for meth detection the idler is dependent on both the seed laser and Monoblock wavelength stability. For example, Monoblock wavelength shifts > 6 pm (or 1.8 GHz, see Figure 22) could result in a detuning of the idler from a molecular absorption feature. As a result, active wavelength stabilization of the Monoblock is required for the meth application.

Wavelength or frequency changes in the Monoblock occur by three phenomenon, all of which are temperature induced. The first way is a temperature-induced shift in the gain profile of the Nd:YAG gain medium in the Monoblock. The tuning coefficient of Nd:YAG is 3.5 pm/K [36]. The second way is a temperature-induced change in the cavity length of the Monoblock based on the thermal expansion coefficient of YAG (8e-6/K) [37]. Based upon the Monoblock operating wavelength (1064 nm), this results in a tuning coefficient of 8.5pm/K. The third way is through a temperature-induced change in the index of refraction of the Nd:YAG gain medium, which has a thermal coefficient of 7.3e-6/K [37]. Based upon the Monoblock operating wavelength (1064 nm), this results in a tuning coefficient of 7.77 pm/K. This tuning coefficient assumes the worst case scenario that the gain medium fills the entire cavity. However, due to the coupled relationship between the cavity length changes and the index of refraction changes, the two phenomenon are added together resulting in a tuning coefficient of 16.27 pm/K. The temperature-induced effect that exhibits the largest tuning coefficient will be the dominating factor, which turns out to be the combination of the cavity length and index of refraction changes. As a result, to achieve wavelength drift less than 6 pm, we need a temperature stability of ± 0.4 Kelvin.

Because of these wavelength stability requirements, for the meth application the goal is to elevate the Monoblock operating temperature above ambient environment temperatures and stabilize the operating temperature within ± 0.4 Kelvin to eliminate wavelength drift caused by widely varying environmental conditions. In contrast, for the CO_2 system to be affected (which uses the signal wavelength), the phase matching

bandwidth of the signal would have to be spectrally detuned from the seed, which would take a shift of > ~1 nm (3 dB phase matching bandwidth at the signal is ~1.4 nm). This large of a shift can only occur if the gain profile of the Nd:YAG were to shift, because changes in the cavity length will only oscillate between cavity modes (~0.01nm shifts). Based upon the tuning coefficient of Nd:YAG it would take a temperature change of 285 Kelvin for a 1 nm shift, which is not practical. Therefore, the CO_2 application will not require active temperature control.

Heat removal is required at higher pulse repetition rates because additional heating can occur in the Monoblock due to the inability of the laser to passively remove heat quickly enough. Additional heating can cause misalignment of the laser if not properly mitigated. Therefore, for both applications, if operating at higher repetition rates, a form of heat removal between shots is required. For the CO_2 application we plan on implementing a form of passive heat removal through use of advanced heat sinks, to minimize complexity and cost. However, for the meth application, active temperature control is already required, so the heat removal will be performed with the same TEC that is used for temperature control.

Monoblock Mounting

To enable hand-held operation, we had to determine a way to mount the Monoblock in a secure package. This had proven to be difficult because of the cavity alignment sensitivity. A design was generated and constructed, with assistance from Mechanical Engineering Master's student Aaron Anderson that allows for secure, stable mounting, as well as temperature control if necessary, which can be seen in Figure 35. In

this design the Monoblock is mounted on a large copper base that acts as a heat sink for thermal stabilization, and eleven self-centering set screws are used to evenly apply pressure across the rail of the Monoblock. This design was constructed and integrated with the Monoblock laser for testing. Experimentally, the even distribution of pressure across the length of the YAG rail has proven to be critical in enabling sturdy mounting without laser misalignment. Temperature control has not yet been implemented, but the design allows for easy integration of temperature control for the meth application. Based on preliminary designs, thermal stabilization will be achieved by implementing two thermoelectric coolers (TEC) on the back side of the copper mount. One TEC will be located near the pumping region, and the other will be near the end of the Monoblock cavity to reduce any temperature gradients. Passive thermal isolation will be used to buffer the Monoblock from the ambient environmental conditions. Several thermocouples located along the rail of the Monoblock will sample and feedback the temperature to a temperature controller. The TEC will elevate the Monoblock to a stable temperature above ambient and will also remove excess heat generated during each pump pulse.

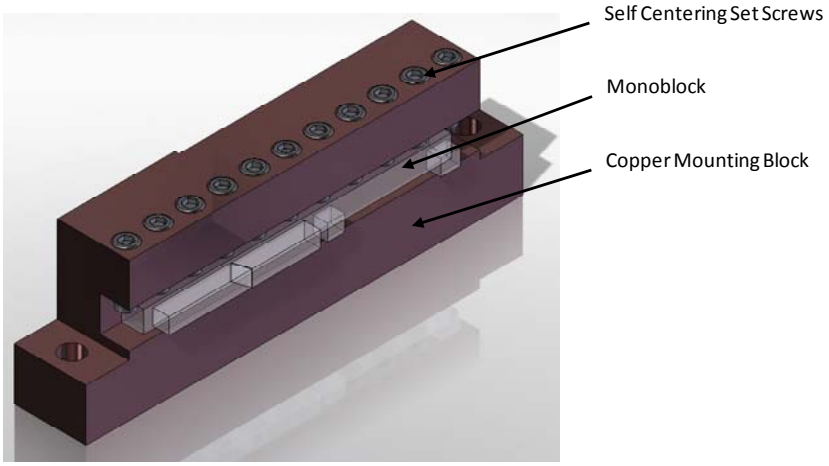

Figure 35. A SolidWorks drawing of the current Monoblock mounting scheme.

Frequency Stability Experiments

Stability experiments were performed to determine the short-term and long-term frequency drift of the Monoblock laser. Although we had calculated the temperature tuning coefficients of the Monoblock, the frequency stability experiments were critical because it was unknown how much the Monoblock temperature was changing shot to shot. Therefore, a heterodyne experiment was performed where an unstabilized Monoblock was optically mixed with a frequency-stable narrowband CW 1064nm DFB laser. The heterodyne signal was detected using a 26-GHz New Focus Detector, and digitized and captured using a 3-GHz Tektronix oscilloscope. The Monoblock temperature was also recorded at every data point via thermocouples mounted along the YAG rail. However, due to poor isolation of the thermocouples, convection dominated the thermocouple measurements and we were unable to correlate temperature drift to frequency drift. Regardless of the temperatures, the results showed that the Monoblock was able to stabilize to a fairly constant operating temperature without active stabilization. This can be seen in Figure 36, which is a plot of each center frequency of the Fourier Transform of the heterodyne signal captured every 10 minutes for ~ 1.5 hours. This result shows that the frequency range of the Fourier Transform of the time domain heterodyne signal was $< \pm 100$ MHz, signifying a temperature drift of < 0.5 Kelvin. This result tells us that the Monoblock laser can passively remove heat fast enough at 1 Hz repetition rates to maintain a stable operating temperature without misalignment. Unfortunately, similar experiments were not performed at increased

repetition rates. Therefore, further research will be devoted to determining the temperature stability at increased repetition rates.

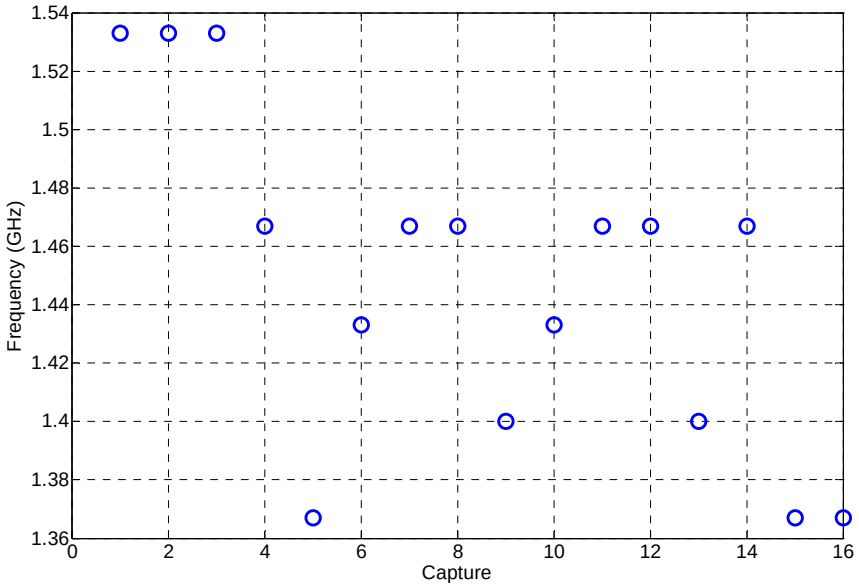

Figure 36. Results showing the long term and short term frequency drift of the Monoblock. The frequency axis is the heterodyne signal frequency measured by heterodyning the Monoblock with a stable DFB laser.

Crystal Temperature Control

Temperature control of the crystal is also critical in both applications for absolute wavelength stability of the nonlinearly converted signal and idler. Similar to the Monoblock laser, the output wavelengths of the OPG process at the signal and idler depend on the operating temperature of the nonlinear crystal. This dependence is due to the temperature-dependent index of refraction of the material which changes the phase matching condition through Eqns. (3.2 and 3.3). Experimentally, we calculated a tuning coefficient of ~0.27 nm/Kelvin by measuring the signal wavelength on an OSA at three different crystal temperatures. This tuning coefficient was verified analytically using the

Sellmeier equation for lithium niobate to determine the indices of refraction at the three different temperatures, and then using Eqns. (3.2 and 3.4) at the calculated indices of refraction to determine the total amount of wavelength change. In addition, we verified that the wavelength tuning was due to the index of refraction change with temperature, rather than the thermal expansion of the nonlinear crystal. The thermal expansion coefficient of lithium niobate is ~5e-6/Kelvin [26]. This results in the same fractional change for the poling period, so a 28-μm poling period would see a 28 pm change in the period for a 10 Kelvin temperature change. This amount of change in the poling period results in a negligible change in the output wavelength.

The ability to tune the output wavelength with temperature is valuable because it allows us to tune the crystal to accurately align the phase matching bandwidth of either the signal or idler with a molecular absorption feature. After alignment, the temperature is kept fixed to detect or monitor on a specific molecular absorption feature. Therefore the goal of crystal temperature control is to stabilize the crystal temperature above the ambient environment temperature to eliminate signal or idler wavelength drift due to environmental convection, as well as allow for tuning of the center of the signal or idler phase matching bandwidth to enable access to the gas effluent absorption wavelength. Further motivation for crystal temperature control includes the need to operate PPLN nonlinear crystals at elevated temperatures to reduce photorefractive effects and reduction of intensity fluctuations that have been observed in previous experiments due to shifts in the center wavelength of the signal with respect to the seed because of instabilities of the crystal temperature. Therefore we want to keep the signal wavelength as spectrally stable

as possible, while utilizing inexpensive components for temperature control. Based upon practical components, the goal was stabilities of better than ± 0.2 Kelvin.

Work was performed, with the assistance of Mechanical Engineering Master's student Aaron Anderson, to design and construct a highly stable, highly efficient, highly compact oven for the nonlinear crystal to achieve optimal center frequency stability that can still accommodate hand-held battery-operated use. The final design that was constructed for this project can be seen in Figure 37. In this design heat is generated via Ni-chrome heating wire by a mechanical relay, and an OMEGA CN4000 heater controller with PID algorithms is used to maintain a constant temperature to better than 0.1° Celsius stability. The Ni-chrome coils are cast in a highly thermally conductive ceramic (Cotronics Corp. Durapot 810). This casting is contained inside low heat transfer ceramic foam (Cotronics Corp. Rescor 310) to allow for increased thermal isolation. The nonlinear crystal is mounted in a copper heat sink with thermal grease and epoxy to provide uniform heat transfer from the Ni-chrome heating coils as well as secure mounting of the crystal in the oven. While heating up to operating temperatures, the Ni-chrome coils utilize ~20 Watts of power (~2 A at 10V), this consumption results in the system reaching 115° Celsius in ~3 minutes with ~1 minute stabilization time. Through various tests, stabilization on the order of ± 0.1° Celsius has been verified. Also, the oven maintains a very small form factor of only 2.5" x 2.5" x 2.5". Based upon a crystal operating temperature of ~60° Celsius (PPSLT), the unit would only be able to be away from the charging station for ~1 hour before a recharge is necessary (assuming a 6.6 Ah, 3.7 V, 6 A lithium ion battery). Improvements can be made to reduce the operating

temperature and increase the passive isolation to better retain the generated heat to allow for longer duration battery-operated operation.

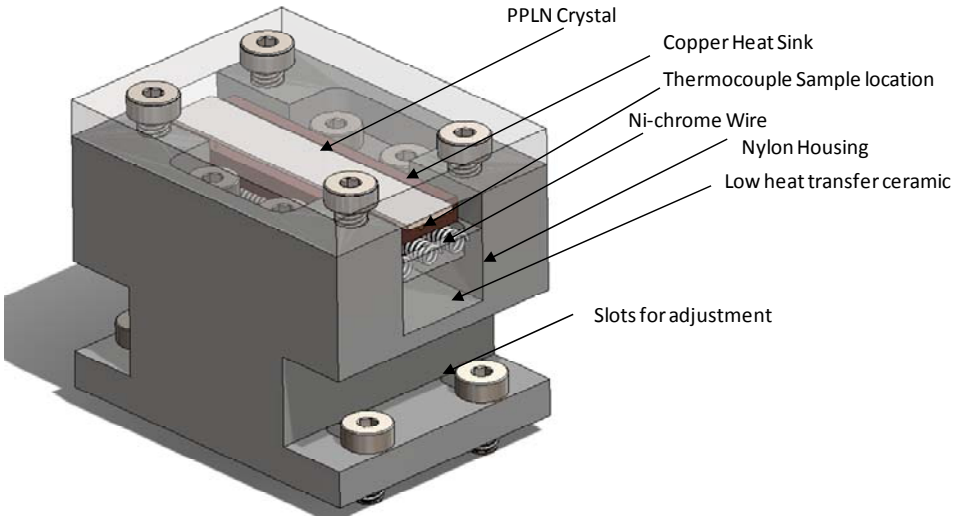

Figure 37. SolidWorks drawing of the current design for nonlinear crystal mounting and temperature stabilization.

Range-Resolved Differential Detector

The CO_2 monitoring application requires continuous measurements during the time of flight of the laser pulse to provide spatial mappings of the CO_2 pollution plumes. The desired meter-level spatial resolution requires a > 100 MHz detector, along with a > 100-MSPS Analog-to-Digital Converter (ADC). Also, to simplify the DIAL measurements, the developed differential detector will simultaneously capture both the "on" and "off" wavelengths and perform the subtraction electronically rather than in post processing. Therefore, due to the lack of commercially available, > 100-MHz differential detectors at 2.0 μm, this application required the development of such a detector. The

> 100-MSPS ADC is a fully developed commercial product, so no additional development was necessary and this will therefore not be discussed in further detail.

To create the differential detector, two Hamamatsu G8423-03 photodiodes were constructed in differential configuration, as shown in the circuit schematic in Figure 38. The photodiodes are connected in differential configuration so that the resulting photocurrents subtract. As a result, the output from the detector board will be the incremental difference between the two detected lidar signals. For the CO_2 application the desired characteristics of the detector were low noise and sufficient bandwidth to resolve 10-ns pulses, resulting in ~2-meter spatial resolution for plume mappings. For the meth detection application, range resolution is not necessary, so advanced detector development is not necessary. Therefore, the focus of this discussion is on the development of a differential detector capable of sufficient bandwidth to resolve 10-ns pulses at 2.0 μm.

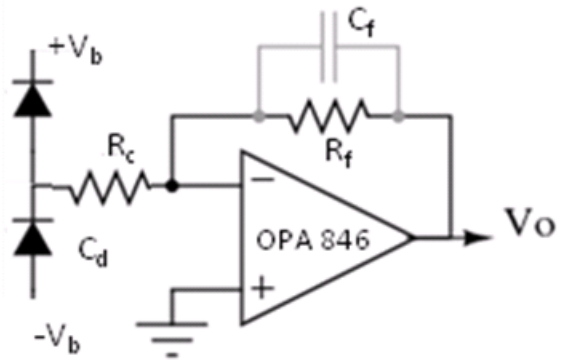

Figure 38. Circuit diagram for the differential detector.

With the help of Dr. Peter Roos, a compensation resistor (R_c) and a feedback capacitor (C_f) were used to suppress instabilities in the op-amp (see Figure 38). A conservative expectation for a transimpedance amplifier bandwidth is given as [38]

$$f_{-3dB} = \frac{\sqrt{f_{RC} f_T}}{2}, \tag{5.1}$$

where f_T is the op-amp unity gain bandwidth, and f_{RC} is the response corner of the feedback resistor R_f and diode capacitance C_d,

$$f_{RC} = \frac{1}{2\pi R_f C_d}. \tag{5.2}$$

We selected the OPA846 for its large gain-bandwidth product (f_T = 1750 MHz) and reasonable noise characteristics. To enable the desired spatial resolution, we chose f_{-3dB} = 100 MHz. Solving Eqn. (5.2) for R_f and inserting an expression for f_{RC} derived from Eqn. (5.1) yields

$$R_f = \frac{1}{2\pi f_{RC} C_d} \approx \frac{f_T}{8\pi f_{-3dB}^2 C_d}. \tag{5.3}$$

Inserting the values for f_{-3dB}, f_{RC}, and C_d yields $R_f = 160\,\Omega$. However, to optimize the performance, in the actual circuit we used $R_f = 340\,\Omega$. A picture of the complete circuit is shown in Figure 39.

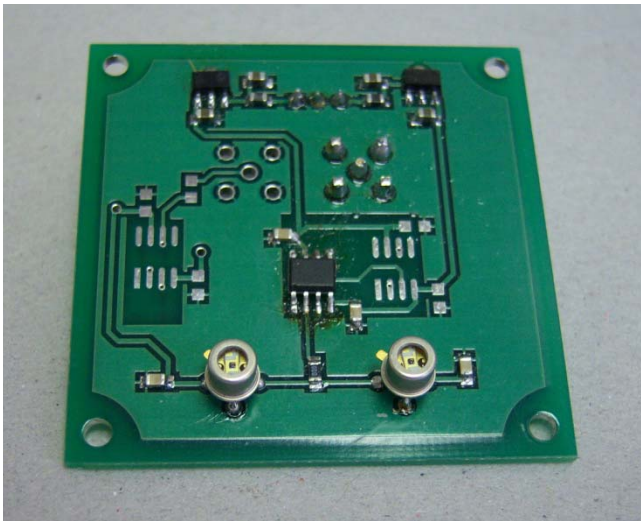

Figure 39. Differential detector circuit for sensitive detection of 2-μm light.

We empirically investigated the feedback capacitor (C_f) that would provide the lowest noise while retaining sufficient bandwidth. The results of this study are shown in Figure 40. The black trace shows the case where no feedback capacitor is present, the blue trace shows when a 1 pF capacitor is used, the green trace shows when a 10 pF capacitor is used, and the red trace shows the measurement background level. All traces were taken with a 50 kHz resolution bandwidth. When no feedback capacitor is used, we observed a broadband resonance near 70 MHz that is due to the instability of the op amp. By including just 1 pF of capacitance, we were able to suppress the resonance and flatten the noise response. Also evident on all traces are the strong narrowband resonances between 95 MHz and 100 MHz. These are not a product of the detector itself, but rather a RF pickup from local radio stations and we anticipate suppressing them substantially with proper shielding. We do not anticipate that this will negatively impact the device performance. In the final design, we used a feedback capacitor of 0.5 pF and a compensation resistor $R_c = 26\,\Omega$.

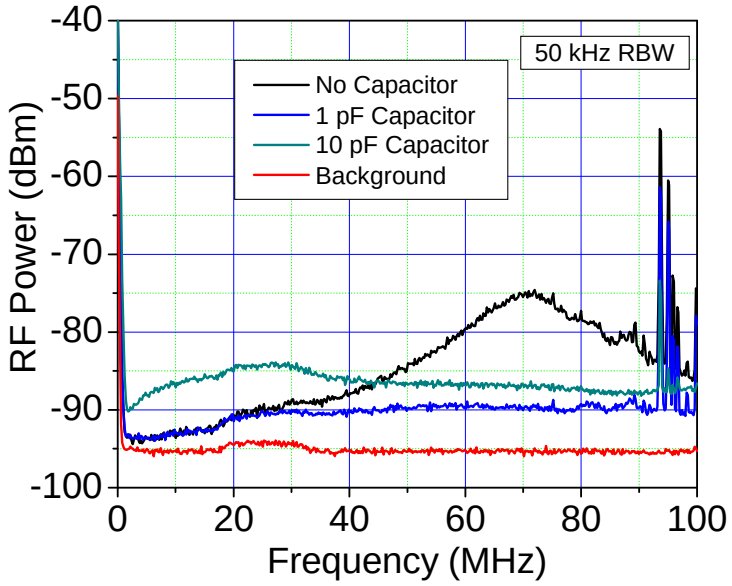

Figure 40. Plot showing the noise levels of different feedback capacitor values.

Upon completion of the detector, experiments were conducted to test the achievable performance. We first tested the extinction ratio, or the ability of the detector to subtract the two channels to eliminate common mode returns. This was done by illuminating both diodes equally to get the best possible extinction, which is represented in Figure 41 by the red trace, and then unblocking one of the diodes (blue). The first dip in the trace is a reference return which was aimed to illuminate just one of the diodes such that we always had a feature as a reference point to trigger the digitizer for the trace captures. The difference between the blue and red trace shows that we can achieve an extinction ratio exceeding 1 part per 100, which is sufficient to measure concentrations that are 1/3 of the ambient atmospheric levels of 380 ppm.

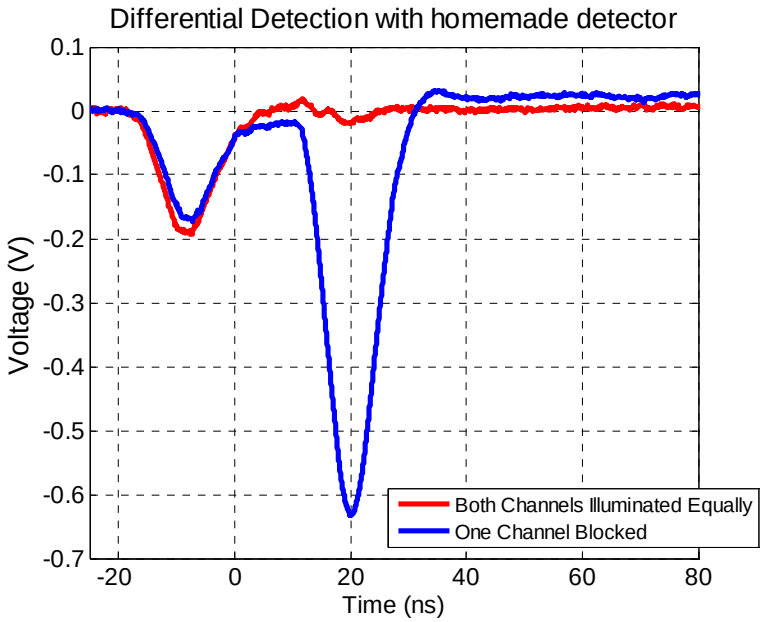

Figure 41. A plot showing the differential detection capabilities of the detector.

Finally, we performed experiments to validate the range resolution capabilities of our light pulse and the differential detector combination. To perform these experiments,

the 2.0-μm emission was directed out of the nonlinear crystal, collimated, and sent across the laboratory onto a white card placed ~5 m from the laser source. We then placed a glass slide 1.97 m in front of the white card in the path of the 2.0-μm emission. In these experiments, one of the diodes was blocked so that the range resolution could be measured without any common-mode subtraction. Due to the high pulse energies, both the glass slide and the white card provided more than sufficient back-scattered photons to generate strong return signals on the detector without any collection optics. These peaks are shown in blue in Figure 42. The blue trace represents the data that was captured when the glass slide and white card were in the path, and the red trace represents the data that was captured with only the white card. The initial small pulse at ~0.75 m was simply used as a trigger pulse. This data shows that the developed differential detector and mid-IR laser have the capability to measure range differences of < 2 meters.

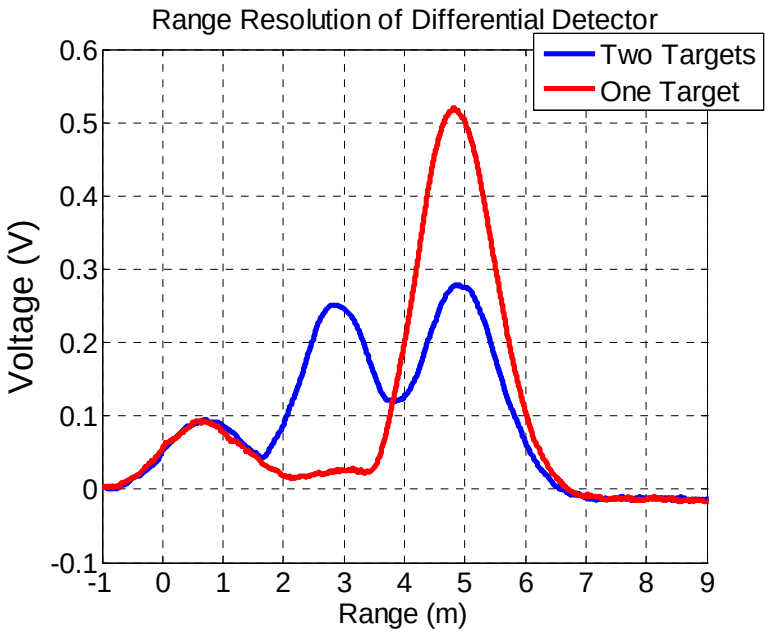

Figure 42. Plot showing the achievable range resolution of the differential detector.

Gated Integrator

The meth detection application only requires a single point measurement to provide a binary “yes” or “no” answer to the presence of a gas effluent. This requires a single-point differential detector, which allows for alternative approaches to processing the detected lidar signals. The alternative return processing approach that we will use is a gated integrator rather than an ADC. This decision is based primarily on cost and savings. The high-speed ADC that would be required to digitize the return pulses is too costly and greatly increases the overall complexity of the device without improved performance. The goal is to make a single-point measurement of the energy in the return optical pulse and this is most simply accomplished with a gated integrator. In contrast, because the CO_2 monitoring application requires range-resolved measurements, the detected lidar signals must be sampled with a fast ADC. Therefore, the focus of this discussion is the development of a gated integrator circuit to reduce the cost and complexity of the meth detection lidar system. Also, the required differential detection for the DIAL measurements can be performed on the gated integrator boards, so commercially available mid-IR detectors will be used. These detectors require very little additional development and therefore will not be discussed.

A gated integrator integrates the total current across a capacitor over the time duration that the gate is open. When connected to a photodiode as shown in Figure 43, the total current is integrated, which includes the photocurrent resulting from the return pulse, as well as dark current from the detector. Additional sources of noise will be current and voltage noise from the op amp, and leakage current from the FET switches

that are typically used as the gating mechanism. It is anticipated that these additional noise sources can be calibrated out of the system. The gate must open when the transmit pulse goes out and remain open for the maximum range window. For the meth lidar system, the maximum range is 100 m (200 m to object and back), so the maximum gate window will be ~600 ns.

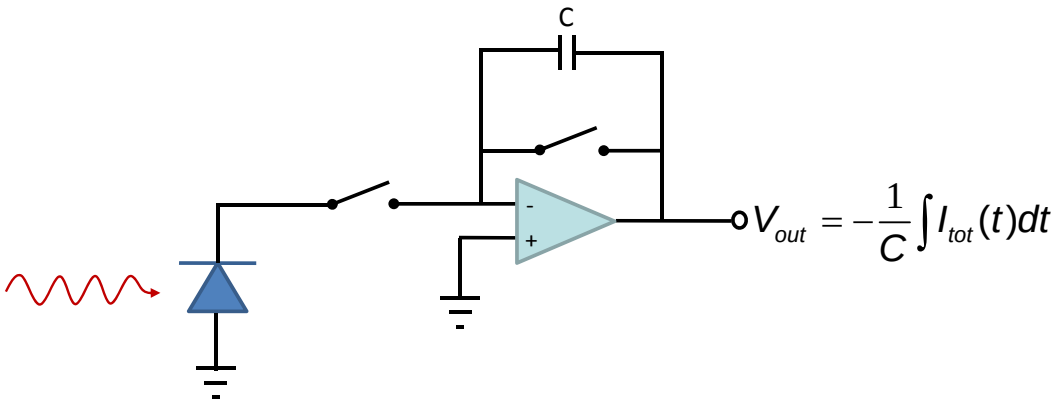

Figure 43. Block diagram of photodiode and gated integrator circuit. The output voltage (V_{out}) is the integrated current divided by the capacitance C.

To determine the achievable performance of the device, two identical prototype gated integrator circuits were constructed. The schematic for this circuit can be seen in Figure 44. The developed circuit is more complex than the basic integrator presented in Figure 43 to minimize leakage noise. A series of biasing resistors is used at the input of the op-amp to bias out the dark current of the detector as well as any other leakage current. We used a 220 pF charging capacitor to achieve the appropriate V_{out} voltage levels for the anticipated incoming photocurrents. The FET (N-channel, model B5583) for the gate switch was chosen to minimize the leakage current from the gate to the drain (reduce noise), and also to provide the highest “open” resistance to maximize the RC time constant to allow adequate sampling of the voltage charge. The op-amp (OPA 627)

was chosen to allow for the desired switching speeds without instability, minimal leakage current, and large slew rates. A CMOS chip (ADG442) was used to generate ± 15 V pulses for proper operation of the FET switch.

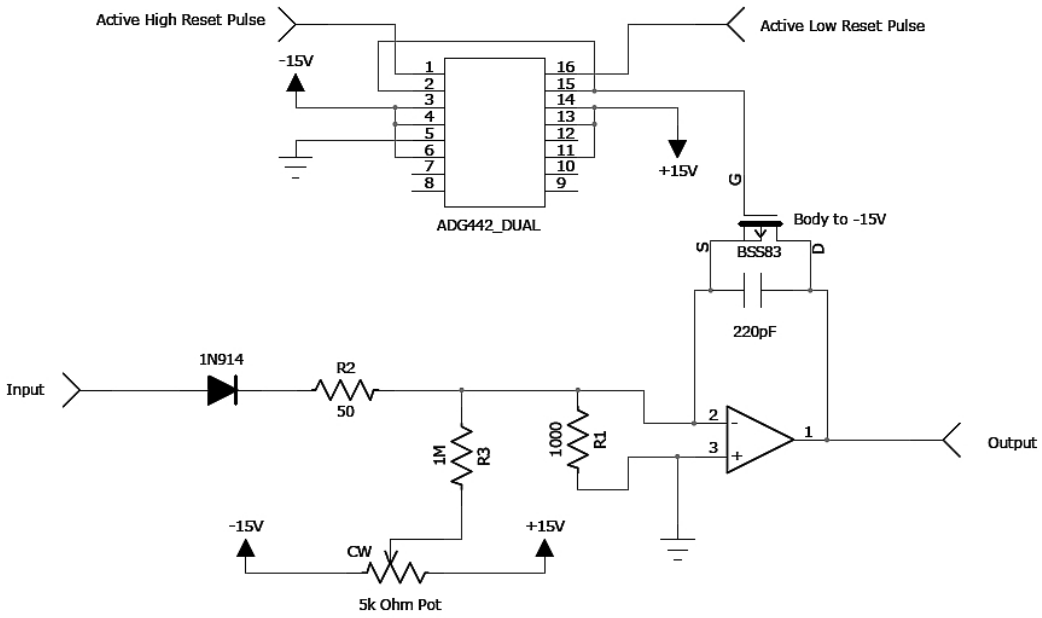

Figure 44. Schematic for the first revision of the gated integrator circuit for return processing.

The final result is a circuit that properly integrates an incoming 10-ns laser pulse and holds the voltage charge until the capacitor is reset, which is demonstrated in Figure 45.

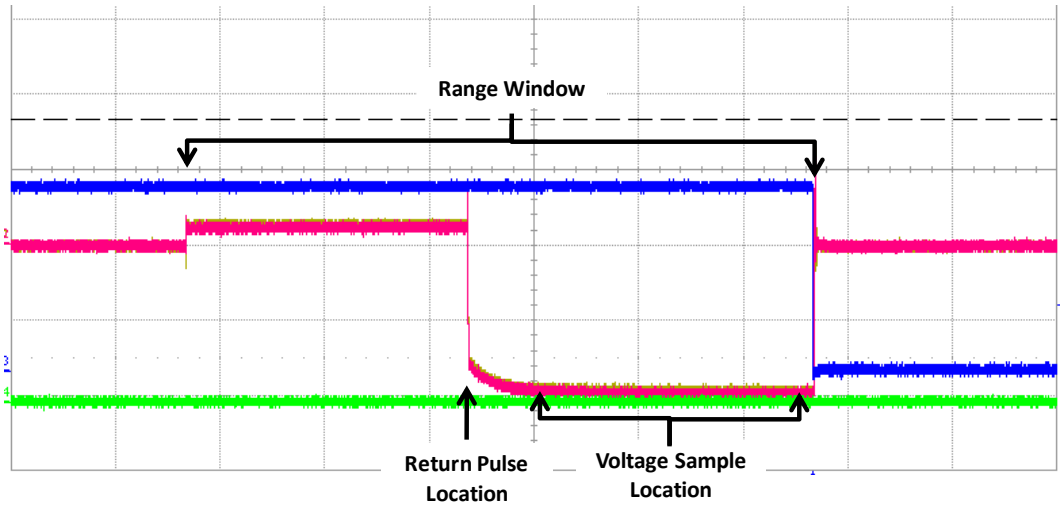

Figure 45. Trace capture of the output of the gated integrator, showing how the device works.

High-resolution DIAL measurements require that this alternative processing method have a SNR that is approximately equivalent to the SNR of the lidar system, which was determined to be ~1600 in Chapter 2 for the meth application. Therefore, experiments were performed to determine the achievable processing performance of the integrator circuits. To accomplish this, we simulated a return pulse by directing the Monoblock laser onto a diffuse scatterer to homogenize the beam. Two identical photodetectors (Thorlabs 210) collected the scattered light from the diffuse scatterer. Each detector was fed into a separate gated integrator circuit and the SNR of the integrator circuits was determined from a series of resultant charges, which is shown in Figure 46. To determine the SNR, we captured a trace as seen in averaged 100 points before and after the simulated pulse and subtracted the two mean values to determine the resultant signal for the integrator. The same analysis was performed for the second integrator. We then took the ratio of the signals from the two integrators. We then iterated this procedure 1000 times and found the mean and the standard deviation of the

1000 calculated ratios. The SNR was found by taking the mean divided by which can be seen in From this data we were able to calculate the mean of all of the traces and divide by the standard deviation to determine the SNR of the gated integrator circuits, which came out to be ~1300. This performance will only slightly limit the overall performance of the lidar system. However, this device will only see improvement with future low-noise revisions of the integrator circuit that can be achieved with advanced auto biasing noise subtraction techniques, and improved op amp and FET noise performance. The benefit to this gated integrator approach is that all of the processing requirements are now contained on a small (2" x 2"), inexpensive (< $100 in parts) circuit board, and no high speed ADC's are required.

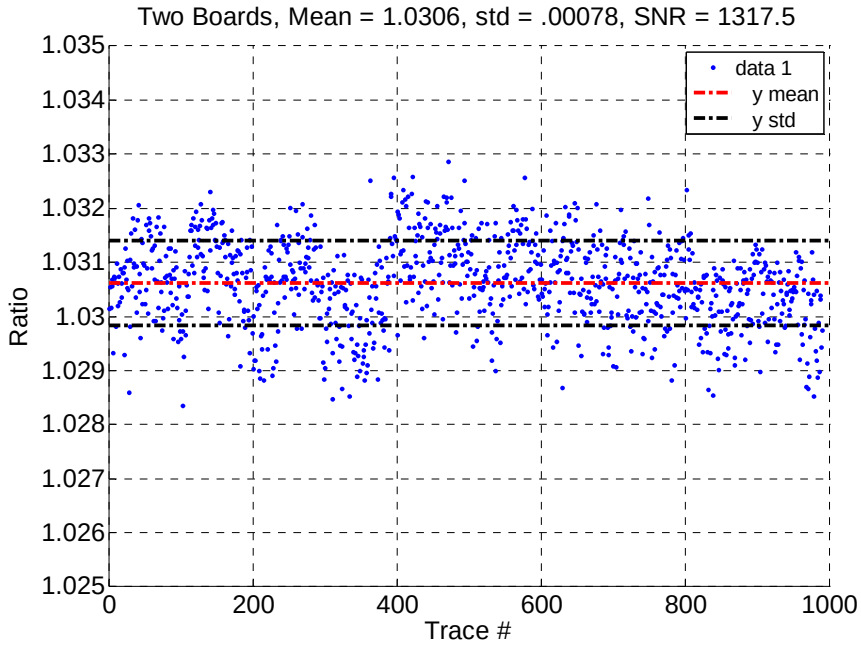

Figure 46. Plot showing the calculated SNR of ~1300 for the two integrator circuits.

Breadboard Prototype Development

All experimental results for this thesis were taken with a setup spread out on an optical table to demonstrate system components and feasibility. We have recently begun compressing the components into a small-form-factor, portable, breadboard prototype for future testing of gas effluents. This breadboard prototype can be seen in Figure 47. For this revision of the prototype, the goal was to make the device completely portable. This was achieved by integrating everything onto a 24” x 18” breadboard. Work was also devoted to down selecting or constructing the proper power supply, pulse generator, and temperature control to allow for a completely portable, standalone unit. To date, we have constructed a completely portable unit which we have used to demonstrate > 3 mJ of broadband OPG emission at the signal wavelength, and a peak conversion efficiency of 28%. Seeding (OPA) has been implemented but the performance has yet to be measured. The picture seen in Figure 47 illustrates the potential for this mid-IR laser to be very compact given the proper optical and mechanical design. We anticipate a final form factor of approximately 7” x 5” x 5”. Also, the total parts cost for this breadboard prototype is < $13,000.00. This can be substantially reduced with volume discounting, and component reduction (no waveplates or beam cubes). We have estimated the total parts cost for a diode pumped version of our narrowband mid-IR laser source to be ~$8,000.00 (approximate total cost per unit will be parts cost x4), and a flashlamp pumped version of our narrowband mid-IR laser source to be ~$5,300.00 (approximate total cost per unit will be parts cost x4). This results in a significant reduction in size and cost compared to current commercially available OPO/OPG based mid-IR laser sources

(see Chapter 1), with a substantial increase in performance for long-range atmospheric mid-IR spectroscopy applications.

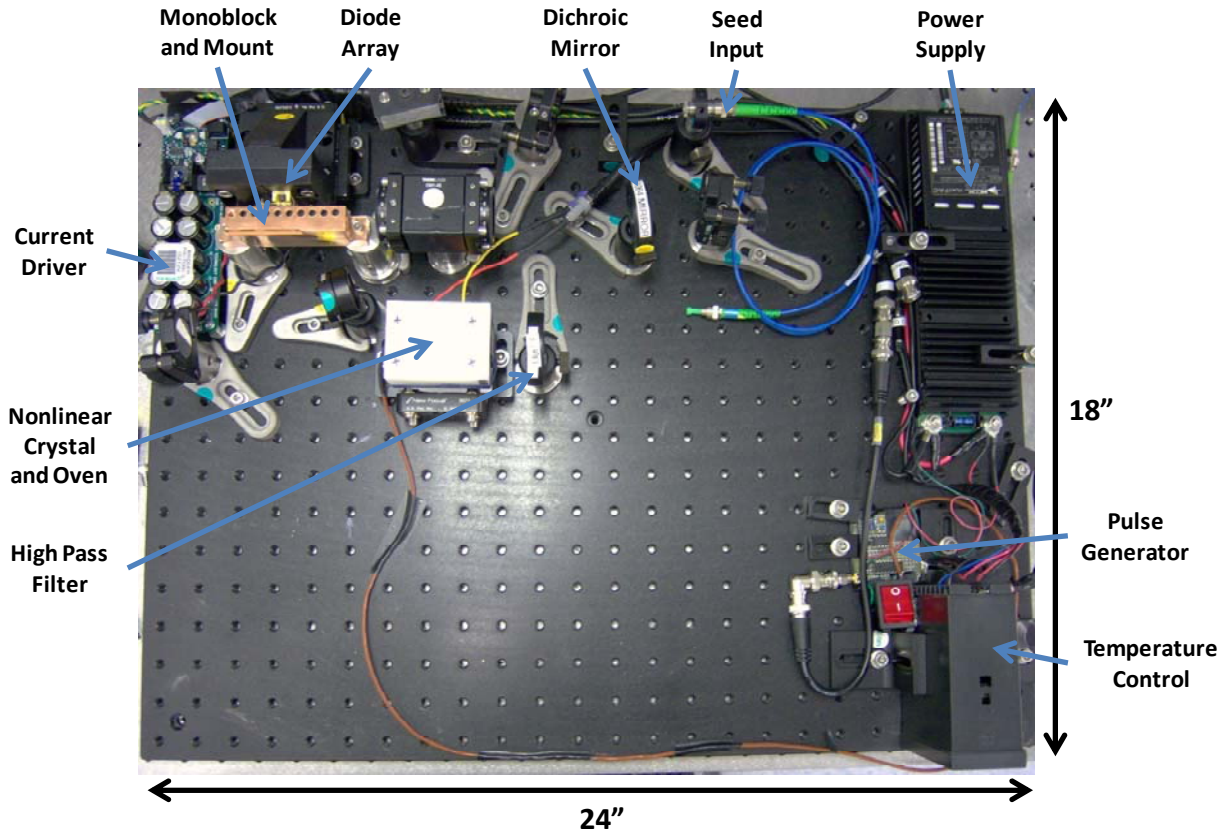

Figure 47. A picture of the portable breadboard prototype being constructed for future detection of meth and CO_2 effluents.

CHAPTER 6

GAS EFFLUENT MEASUREMENTS

This chapter is devoted to documenting the experimental data obtained from proof-of-concept gas effluent measurements performed with our developed narrowband mid-IR laser source. The goal of these experiments is to verify that the seeded output of our laser source is sufficiently narrowband to see absorption from a gas effluent. Due to the lack of suitable seed sources far into the mid-IR, our approach is to seed at the lower signal wavelength where suitable seed lasers exist. As a result, spectroscopy at the signal wavelength compared to the idler is simplified because the absolute wavelength stability of the pulsed signal output is dictated purely by the highly stable seed laser regardless of the stability of the Monoblock. Therefore, these proof-of-concept experiments were conducted using 2.0-μm generated light at the signal wavelength to detect CO_2. This chapter discusses the steps necessary to perform the proof of concept experiments, and the obtained results.

Gas Cell Construction

The first step towards gas effluent detection was to procure a gas cell filled with CO_2. We were able to borrow a 0.5-meter gas cell from the Physics department at Montana State University with windows positioned at the Brewster angle to avoid back reflections and etalon effects in the cell, making it unnecessary to AR coat the windows.

A picture of the gas cell is shown with the end caps removed in Figure 48 (left), as well as the end of the cell where the windows will be placed (right).

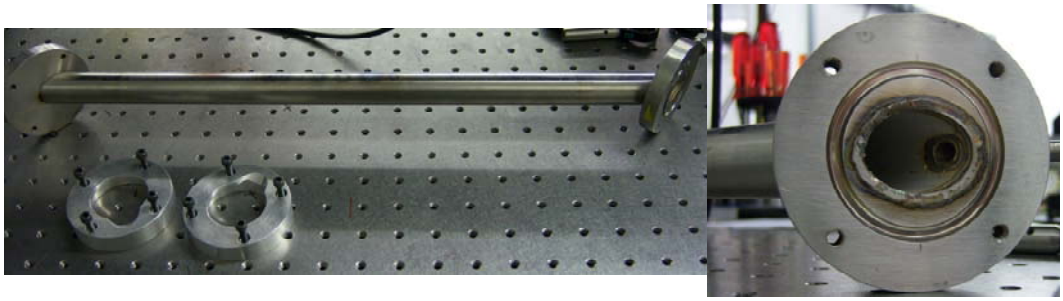

Figure 48. (Left) Picture taken of the 0.5m long gas cell that was used for gas effluent detection experiments. The ends of the cell are cut at a Brewster angle to eliminate etalon effects.

To complete the construction of the gas cell, we had to find the appropriate set of windows for the anticipated experiments. The windows are required to be highly transmissive in the mid-IR from 1.5 μm to 5 μm to allow for testing of different gas effluents throughout the mid-IR, and to have sufficient thickness to withstand pressures of up to 10 atmospheres to allow for high-pressure testing if necessary. Also, we wanted to choose a material that was non-crystalline to avoid birefringence effects. Based on these criteria, we chose Calcium Fluoride material, and ordered a pair of 10-mm thick, 50-mm diameter, Calcium Fluoride windows from Argus International and inserted them into the cell. The completed cell is shown in Figure 49. On the left side of the cell we added a valve to allow for simple filling of the cell without any leakage during or after the transfer. On the right side of the cell we added a pressure gauge and a pressure relief blow-off valve. These components allow for accurate monitoring of the pressure inside of the cell to ensure safe pressure levels. We initially filled the cell to a pressure of 10 atmospheres to check for leaks and then reduced the pressure to 1 atm for our studies.

The cell was evacuated prior to being filled, so effectively the concentration inside the cell was ~100% CO_2.

Figure 49. Constructed gas cell with additional components to fill the cell with CO_2 and safely monitor the pressure inside of the cell.

Theoretical Absorbance

Prior to detection with our mid-IR laser source, experiments were performed to validate the theoretical absorbance of CO_2, and to map the absorption feature locations to an operating temperature of the seed laser. These experiments were performed by passing the 2.0-μm seed laser through the procured gas cell onto a single photodiode of the differential detector. The seed laser was temperature tuned through a range of ~10 degrees C, and the corresponding power transmission was recorded. Nanoplus GmbH, the manufacturer of the seed laser, provides a single-point measurement that maps a temperature to a wavelength, as well as a tuning coefficient of 0.19 nm/° Celsius. These coefficients were used to determine the wavelength-dependent transmission of CO_2 within the gas cell. This experimental data was compared to the theoretical CO_2 transmission based on molecular absorbance information obtained from HITRAN [3],

beer's law for transmission, and the estimated concentration within the cell. Figure 50 shows good agreement between the experimental and theoretical datasets, which validates our theoretical CO_2 models. The apparent decrease in transmission as the wavelength is increased is actually due to a decrease in the seed laser output power at high operating temperatures, which could have been removed by doing differential detection.

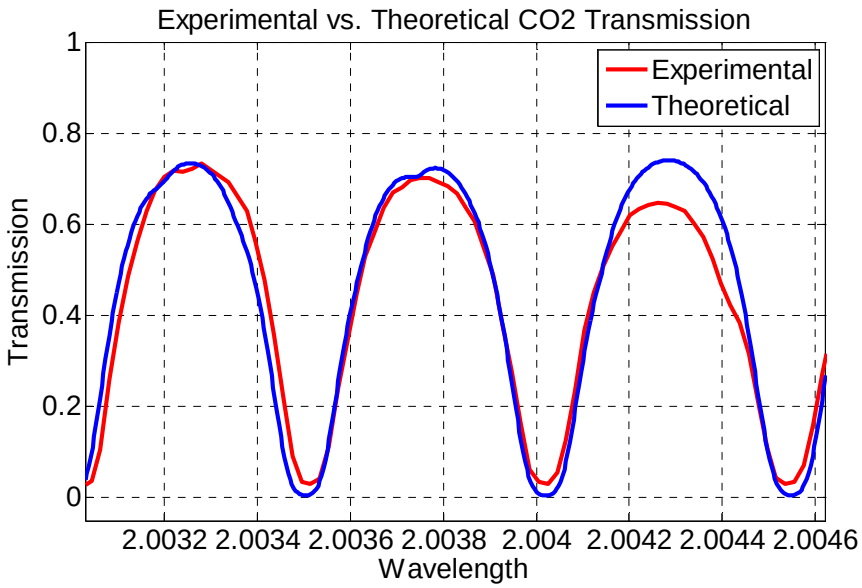

Figure 50. Plot showing spectroscopy results obtained by tuning the 2.0 μm DFB seed laser across several CO_2 transitions (red), compared to theoretical transmission data of CO_2 (blue) based on molecular absorbance information obtained from the HITRAN, beer's law for transmission, and the estimated concentration within the cell.

Experimental Setup

An experimental setup was constructed to perform differential detection of CO_2 with our pulsed mid-IR laser source, which is shown in Figure 51. Advanced techniques had to be implemented to accurately perform the measurements due to the lack of sufficient levels of seed power. To perform detection of CO_2 we must seed the OPG

process with a 2.0-μm DFB laser at the signal wavelength. Unfortunately, DFB lasers at this wavelength are relatively immature, and we were limited to ~3mW of free space output power. Upon fiber coupling the light, isolating the diode from back reflections from the Monoblock, and passing the light through the optical system, we were left with ~10 μW of seed power, resulting in a very poor seeding efficiency. The loss in power was due to losses in fiber coupling caused by poor beam quality of the seed laser as well as insufficient optics for fiber coupling 2.0-μm light, insertion loss in 1.5-μm fibers at our wavelength of 2.0 μm, ~10dB insertion loss in the fiber isolators as we were forced to use isolators designed for 1.5 μm, and optics not coated or designed for 2.0-μm operation. A fiber-coupled seed laser, as well as optics, fibers, and isolators designed for 2.0-μm operation will alleviate the low seed power issues. Even with this small amount of seed light, we were still able to produce narrowband emission with about 5% seeding efficiency. However, for improved performance, we effectively enhanced the seeding efficiency by passing the 2.0-μm pulses through a monochromator prior to detecting CO_2. As shown in Figure 51, the mid-IR output light was coupled into a fiber and passed through the monochromator to select out the “efficiently seeded” portion of the total signal energy. To differentially detect CO_2, the collected light from the monochromator was passed through a non polarizing beam splitter (NPBS) to perform a 50 / 50 split of the narrowband light. One portion of the split was passed around the gas cell and onto the negative channel of the differential detector. The other portion was passed through the gas cell and onto the positive channel of the differential detector. The two channels of the

differential detector were balanced with the seed laser (and therefore the emitted signal) tuned off of a CO_2 transition.

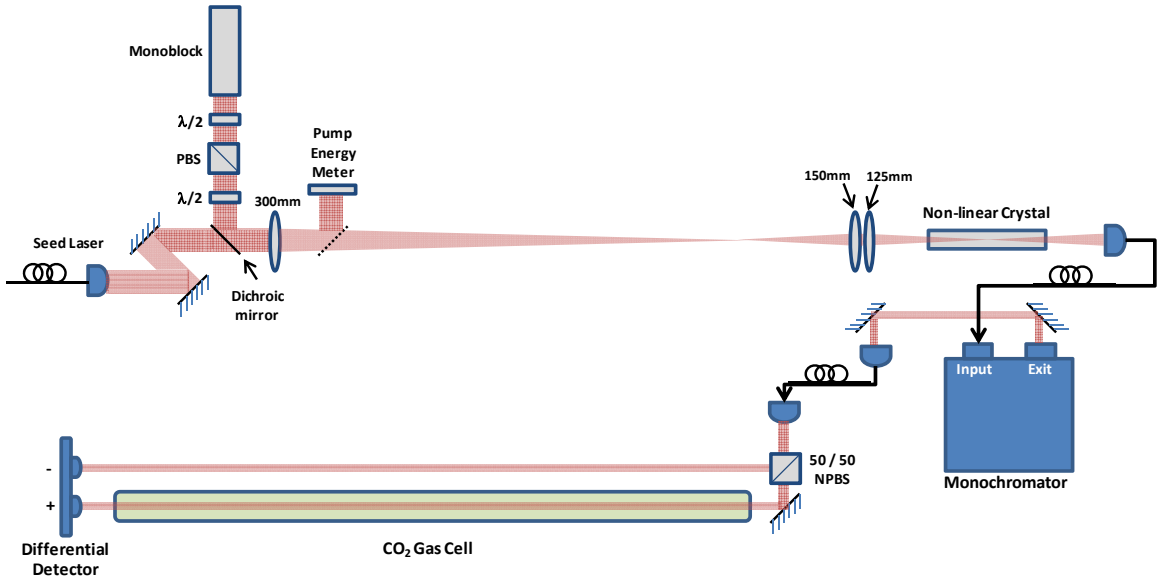

Figure 51. Experimental setup to perform differential detection of CO_2.

Differential Detection of CO_2

Using this experimental setup we performed differential detection of CO_2, which can be seen in Figure 52. To perform this measurement, the seed laser was tuned off of a CO_2 absorption feature (determined from Figure 50) and the detector was balanced as accurately as possibly to equally subtract the two channels. The balanced signal is represented by the red trace. The seed laser was then tuned on a CO_2 absorption feature, which is represented by the blue trace. This result shows that when we tune on the feature we get absorption of the pulsed narrowband emission that passes through the cell and an imbalance occurs between the two channels. Each trace represents 10 averages to allow for better resolution of the residual imbalance in the red trace. The pulse energy for

subsequent pulses was varying substantially due to the small amount of seed laser light (the pulse peak height standard deviation was 55% of the mean). For sequential differential detection, which is the process of taking the on- and off-transition measurements sequentially rather than at the same time, this pulse-to-pulse variation would seriously compromise the measurement. However, because only one pulse is used for this differential detection, we can easily see the difference between on- and off-transition. Moreover, our measurements with proper levels of seed power available at lower wavelengths and improved mode matching between the pump and seed, indicate that the differential detection measurements can be performed without the use of the monochromator. The present experiments prove the critical capability that our pulses are sufficiently spectrally narrow to detect CO_2.

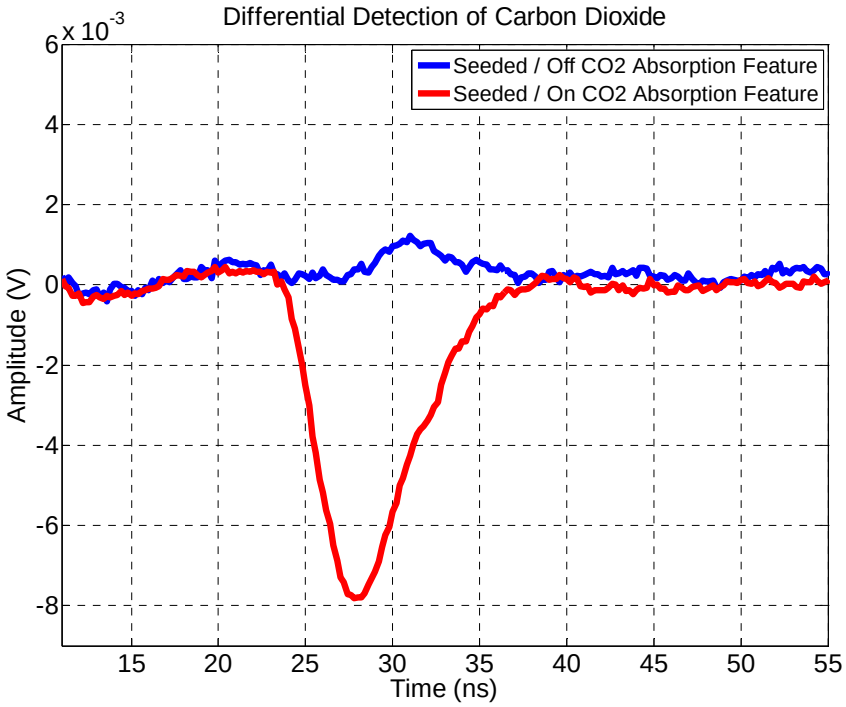

Figure 52. Plot showing differential detection of CO_2 using our developed laser system.

An estimation of the concentration of CO_2 inside of the gas cell can be calculated through use of Eqn. (2.12), the known molecular absorption cross section (σ_{on}) for CO_2, and the detected energy at the "on" and the "off" wavelengths. The detected energy for each wavelength after the gas cell (after a range bin $R+\Delta R$) is calculated using the voltage at the "on" and "off" wavelengths determined from Figure 52, the responsivity of the diodes of 1.3 A/W, and the transimpedance gain of the detector of 360 V/A. To accurately determine the energy ratio of the "on" and "off" wavelengths, the energy on each diode of the detector when balanced must be known. Simplifications can be made to Eqn. (2.12) because the energy in the "on" and "off" wavelengths at range R, prior to one path passing through the gas cell are the same (50/50 NPBS split) and will therefore cancel from the equation. Additionally, the variable σ_{off} can be assumed to be essentially zero because the "off" path does not interact with the CO_2 molecules in the gas cell.

CHAPTER 7

SUMMARY

Summary of Progress

We have demonstrated the ability to use the compact Monoblock laser in combination with OPG in nonlinear crystals to generate suitable levels of mid-IR light (> 1 mJ). This result (along with the lidar equation) proves the feasibility of our mid-IR laser source to perform atmospheric detection and monitoring of atmospheric gases at ranges of 100 m. We have also shown the ability to use OPA to generate narrowband mid-IR light, with linewidths < 350 MHz. These narrow linewidths in combination with the demonstrated pulse energies, make our laser source ideal for high-resolution, long-range, mid-IR spectroscopy of gas effluents. To prove the capabilities of our mid-IR laser source, we successfully performed differential detection of CO_2, which verified the feasibility of our proposed laser source for mid-IR spectroscopy. We have also shown the ability to temperature tune the nonlinear crystals to reach several different molecular absorption lines. In addition we have designed a mask for a five channel nonlinear crystal that will allow us to tune our laser source anywhere in the mid-IR from 2 μm to 4 μm We have also designed, constructed, and tested system level components to demonstrate advanced features of our mid-IR laser source such as < 1 GHz absolute wavelength stability, high repetition rates (10 Hz), and meter-level range resolutions for spatial mapping of gas effluents. Finally, we have shown the ability to build such a mid-IR laser source into a compact package (currently 24” x 18” x 7”, will achieve 7” x 5” x 5”) for

low cost (currently < $13,000 parts cost, will achieve < $8,000 parts cost), which will make our mid-IR laser source a legitimate option for hand-held, long-range, mid-IR spectroscopy applications.

Future Work

Although significant progress has been made to develop this mid-IR laser source, several critical areas need to be advanced in future research. The most critical improvement that must be made is with the seeding efficiency. Currently without spatial filtering we can only achieve 35% seeding efficiencies in the mid-IR. This efficiency must be improved for this device to perform with high resolution. It needs to be determined if we can achieve suitable seeding efficiencies with the current pump source, or if the spatial mode of the Monoblock laser has to be improved. Additionally, further research must be performed on the Monoblock at higher repetition rates to determine the achievable wavelength (temperature) stability. Also, we need to demonstrate the ability to use the idler wavelength to perform differential detection of a gas effluent. In addition to laser research, extensive research must be devoted to determining the achievable performance of dual-wavelength seeding for simultaneous DIAL measurements. If this approach will degrade the performance of the lidar system, other techniques to perform simultaneous DIAL must be researched to determine the most appropriate method. Finally, to develop a fully functional lidar system, extensive work needs to be devoted to the receiver portion of the system, more specifically model validation, integration of the

receiver optics and the back end processing, and integration of the full receiver subsystem with the mid-IR laser source.

REFERENCES

[1] I.T. Sorokina, and K.L. Vodopyanov, (Eds.), *Solid-State Mid-Infrared Laser Sources*, Springer Topics Appl. Phys. **89** (2003).

[2] C. Weitkamp, ed., *Lidar: Range-Resolved Optical Remote Sensing of the Atmosphere.* New York: Springer, 2005.

[3] HITRAN radiative transfer database (2008 Version) Obtained from http://www.cfa.Harvard.edu/HITRAN/HITRAN2008/.

[4] M Squared Lasers, "Firefly-IR," http://www.m2lasers.com/Products/LaserSystems/FireflyIR/tabid/93/Default.htm, Last Accessed 10/31/2009.

[5] Aculight Corporation,"Products," http://www.aculight.com/standardProducts.htm, Last Accessed 11/5/09.

[6] NovaWave Technologies, "IRIS 1000 DFG-based Mid-infrared Laser System," http://www.novawavetech.com/products/photonics/mid-infrared-lasers/iris-1000-dfg-based-mid-infrared-laser-system.html, Last Accessed 11/3/2009.

[7] Montana Meth Project, Montana Meth Use and Attitudes Survey, August 2005, from the web at www.montanameth.org, last accessed 7/10/2008.

[8] Office of National Drug Control Policy, Pushing Back Against Meth: A Progress Report on the Fight Against Methamphetamine in the United States. November 2006.

[9] Montana Attorney General, Mike McGrath. Methamphetamine in Montana: A Follow-up Report on Trends and Progress. April 2008.

[10] Drug Enforcement Agency, "Maps of Methamphetamine Lab Incidents," www.usdoj.gov/dea/concern/map_lab_seizures.html, last accessed 7/10/2008.

[11] Carbon Dioxide Information Analysis Center, http://cdiac.esd.ornl.gov/home.html, last accessed 05/13/07.

[12] Australian Gov., Bureau of Meteorology, www.bom.gov.au/info/climate/change/gallery/25.shtml, Last Accessed 05/13/09.

[13] Climate Change 2001. Synthesis Report. A Contribution of Working Groups I, II, and III to the Third Assessment Report of the Intergovernmental Panel on Climate Change, Edited by R.T. Watson, Cambridge University Press, Cambridge, U.K., 2001.

[14] Scientific Materials Corporation, www.scientificmaterials.com, Last Accessed 11/10/09.

[15] John E. Nettleton, Bradley W. Schilling, Dallas N. Barr, and Jonathan S. Lei, "Monoblock laser for a low-cost, eyesafe, microlaser range finder," Appl. Opt. **39**, 2428-2432 (2000).

[16] The Infrared Handbook, revised edition, William L. Wolfe and George J. Zissis, editors SPIE Press (Bellingham, WA), 1989.

[17] Martyny, J.W.,Arbuckle, S.L, McCammon. Jr., C.S. Esswein, E.J, Erb N, VanDyke, M, "Chemical concentrations and contamination associated with clandestine methamphetamine laboratories," J. Chem. Health Safety, doi:10.1016/j.jchas.2007.01.012 (2007).

[18] Boston Electronics, "Infrared Detectors," http://www.boselec.com/products/detir.html. Last Accessed 11/5/09.

[19] Hamamatsu Photonics, "G8423-03 Photodiodes," http://sales.hamamatsu.com/index.php?id=13183489&language=1&undefined, Last Accessed 10/30/2009.

[20] M.D. Obland, "Water vapor profiling using a widely tunable amplified diode laser differential absorption lidar (DIAL)," Ph.D. Dissertation, April 2007.

[21] R. M. Measures, *Laser Remote Sensing*, (New York: John Wiley & Sons, 1992).

[22] Boyd, Robert, *Nonlinear Optics*, *Second Edition*, (Orlando: Elsevier Science, 2003).

[23] Y. Guan, J.W. Haus, and P. Powers, "Broadband and off-axis optical parametric generation in periodically poled LiNbO3," J. Opt. Soc. Am. B, **21** (2004).

[24] R. Paschotta, "Photodarkening," http://www.rp-photonics.com/photodarkening.html, Last Accessed 10/10/09.

[25] D. Hum, "Frequency conversion in near-stoichiometric lithium tantalite fabricated by vapor transport equilibration," Ph.D. Thesis. March 2007.

[26] Almaz Optics, Inc. "Lithium Niobate, LiNbO3," http://www.almazoptics.com/LiNbO3.html, Last Accessed 10/10/09.

[27] J. Hirohashi, V. Pasiskevicius, S. Wang, and F. Laurell, "Picosecond blue-light-induced infrared absorption in single-domain and periodically poled ferroelectrics," J. Of App. Phys. **101**, d.o.i. 033105 2007.

[28] Y. Furukawa, K. Kitamura, A. Alexandrovski, R.K. Route, M.M. Fejer, G. Foulon, "Green-induced infrared absorption in MgO doped $LiNbO_3$," Applied Physics Letters, **78** (2001).

[29] A.J. Tracy, C. Lopez, A. Hankla, D.J. Bamford, D.J.Cook, S.J. Sharpe, "Generation of high-average-power visible light in periodically poled nearly stoichiometric lithium tantalate,"Appl. Optics **48** (2009).

[30] A.L. Alexandrovski, G. Foulon, L.E. Myers, R.K. Route, and M.M. Fejer, "UV and visible absorption in LiTaO3", SPIE **3610**, 44-51, 1999.

[31] K. Kitamura, Y. Furukawa, S. Takekawa, T. Hatanaka, H. Ito, and V. Gopalan, "Non-stoichiometric control of LiNbO3 and LiTaO3 in ferroelectric domain engineering for optical devices", Ferroelectrics **257**, 235-243, 2001.

[32] Almaz Optics, Inc."Lithium Tantalate," http://www.almazoptics.com/LiTaO3.html. Last Accessed 10/10/09.

[33] P.E. Powers, P.K. Bojja, R. Alkuwari, and E. Vershure, "High-energy seeded optical parametric generation with elliptical beams in quasi-phase-matched crystals," J. Opt. Soc. Am. B **22** (2005).

[34] P. E. Powers, K. W. Aniolek, T. J. Kulp, B. A. Richman, and S. E. Bisson, "Periodically poled lithium niobate optical parametric amplifier seeded with the narrow-band filtered output of an optical parametric generator," Opt. Lett. **23**,1886–1888 (1998).

[35] M. Rahm, U. Bäder, G. Anstett, J.-P. Meyn, R. Wallenstein, and A. Borsutzky, "Pulse-to-pulse wavelength tuning of an injection seeded nanosecond optical parametric generator with 10 kHz repetition rate," Appl. Phys. B 75, 47–51 (2002).

[36] M. Frede, R. Wilhelm, M. Brendel, C. Fallnich, "High power fundamental mode Nd:YAG laser with efficient birefringence compensation," Optics Express 12 (2004).

[37] Impex HighTech GmbH, "Nd:YAG Laser Crystals," http://www.impex-hightech.de/Lmat-nd-yag.html, Last Accessed 10/31/2009.

[38] P. C. D. Hobbs, *Building Electro-Optical Systems*, Ch 18, (John Wiley and Sons, New York, 2000).